NORTHWESTERN UNIVERSITY

# Inverse-Design and Fabrication of Electromagnetic Devices

A DISSERTATION

SUBMITTED TO THE GRADUATE SCHOOL
IN PARTIAL FULFILLMENT OF THE REQUIREMENTS

for the degree

DOCTOR OF PHILOSOPHY

Field of Electrical Engineering

By

Francois Callewaert

EVANSTON, ILLINOIS

September 2018

# Abstract

Maxwell equations are behind an incredible number of physical phenomena, explaining the behavior of light, electricity and magnetism, from Gamma rays to ultra-low frequency radio-waves. Since their inception in 1861, many approximations have been derived, many devices have been modelled and fabricated to manipulate the electromagnetic fields, and more recently many computational techniques have been developed to model the behavior of light-matter interactions numerically. However, until recently only forward techniques have been developed, to simulate the behavior of the electromagnetic field inside devices and materials coming from the imagination of a human being.

In this 21$^{st}$ century, artificial intelligence replaces the human for more and more complex tasks. Electromagnetics will not miss this opportunity to bring tremendous computing power and powerful algorithms to automate the device design task, called inverse-design. In this work, we develop an algorithm to do inverse-design of dielectric devices with sizes in the order of magnitude of the wavelength. The algorithm is used to design and fabricate multiple types of electromagnetic devices for the manipulation of light on-chip or in free-space, with low index or high-index dielectrics, from the microwaves to the near-infrared and maybe the visible in the future.

This dissertation is organized as follows. Chapter 1 presents the wave equations, various approximations, various computational techniques to simulate electromagnetic fields and various types of electromagnetic devices based on the inputs, outputs and types of materials inside. Chapter 2 explains the theory behind inverse-design, the comparison between the algorithm in this work and some other algorithms in the literature, regularization methods and a few insights for the

implementation. Chapter 3 demonstrates our first inverse-designed device: a two-dimensional optical diode made of Silicon and air. This chapter explores some details of the optimization process as a function of the number of iterations, and the tuning to select the best hyperparameters of the algorithm to optimize the performance of the final optical diode. Chapter 4 explores the design and fabrication of polymer meta-devices to transform free-space incoming electromagnetic radiation. Meta-gratings including polarization splitters and bends are demonstrated, as well as meta-lenses, one with short focal distance, one with long focal distance and one with tunable focal distance. The algorithm is adapted to new types of inputs and outputs such as plane-waves and cylindrical waves. The physical behavior of polymer-based devices, which have a low index, does not rely on strong resonances such as those observed in Silicon-based devices. This allows to design devices with a very large bandwidth. Furthermore, polymers can be 3D-printed, which allows to create devices with much more complex geometries and much larger aspect ratio than devices made with traditional lithography methods. In this chapter, we explore millimeter-scale 3D-printing to make microwave and millimeter-wave meta-devices, as well as nanometer-scale 2-photon lithography 3D-printing for the fabrication of a Near InfraRed polarization splitter. Finally, chapter 5 concludes this dissertation and provides some perspectives on the future opportunities for the improvement of the inverse-design computational method, its extension to more types of electromagnetic devices and its combination with advanced fabrication methods.

# Acknowledgements

This PhD work and dissertation would have been impossible without the help and support from many people and organizations. First, I would like to thank my PhD advisor, Prof. Koray Aydin, for giving me this amazing opportunity, for trusting me to start a new project, for offering his continuous guidance and support throughout the project. I also would like to thank Prof. Hooman Mohseni and the other members of my committee for their advice after the prospectus and their time reviewing this work. I would like to especially than Profs. Alan V. Sahakian, Prem Kumar and Sridhar Krishnaswamy, as well as Dr. Vesselin Velev and Dr. Heming Wei for the joyful and fruitful collaborations we had over the past two years. There would be no experimental section of this work without their support, their technical help and their sharing and trusting me with very expensive equipment. I would like to thank my teammates Serkan Butun, Zizhuo Liu and Edgar Palacios for their help in experimental projects, and Zhongyang Li, Wisnu Hadibrata, Sina Abedini and Xianglian Song for creating a joyful work environment and for fruitful discussions. I would like to particularly encourage Wisnu Hadibrata to pursue this project and explore new horizons in the inverse-design. I would like to thank all my friends, colleagues and staff at Northwestern for making such a nice and friendly environment to feel part of a big family and to grow as a person. I would like to thank the professors for their teachings, staff members and the EECS department staff in particular for their availability. I would also like to thank my advisor for supporting, university staff for funding, and friends Lin Sun, Jingshan Du, Mohsen Rezaei, Simone Bianconi, Travis Hamilton and Skyler Wheaton for helping organize multiple academic and professional talks with the SPIE organization.

Finally, I would like to thank my parents and siblings for all their support and encouragement. Most importantly, I deeply thank my wife Chang for always standing by me with endless love, and my two sons Lucas and Ted for bringing spice in my life and pushing me to be a better person every day.

# Table of contents

# List of Figures and Tables

# I) Introduction

## a) Maxwell's wave equations

In 1861, James Clerk Maxwell published the equations that would bear his name:

$$\nabla.\mathbf{D}=\rho \quad (1)$$

$$\nabla.\mathbf{B}=0 \quad (2)$$

$$\nabla\times\mathbf{E}=-\frac{\partial\mathbf{B}}{\partial t} \quad (3)$$

$$\nabla\times\mathbf{H}=\mathbf{J}-\frac{\partial\mathbf{D}}{\partial t} \quad (4)$$

These equations unified the fields of electronics, magnetism and optics by establishing a relation between the electric and magnetic fields **E** and **B**, the displacement and magnetizing fields **D** and **H**, the electric charges and currents ρ and **J** and the polarization and magnetization fields **P** and **M** that follow the constitutive equations:

$$\mathbf{D} = \varepsilon_0 \mathbf{E} + \mathbf{P} \approx \varepsilon \mathbf{E} \quad (5)$$

$$\mathbf{H} = 1/\mu_0 \mathbf{B} - \mathbf{M} \approx 1/\mu \mathbf{B} \quad (6)$$

where $\varepsilon_0$ and $\mu_0$ are respectively the permittivity and permeability of free space, and the right terms in both equations represent the approximation that describes the electromagnetic behavior of linear materials, where ε and μ are the permittivity and permeability, which are individual characteristics of the material.

In this case, the four equations can be replaced by a single wave equation, written as a function of either **E** or **H**:

$$\nabla\times\mu^{-1}\nabla\times\mathbf{E}=-\varepsilon\frac{\partial^2\mathbf{E}}{\partial t^2}-\frac{\partial\mathbf{J}}{\partial t} \quad (7)$$

$$\nabla \times \varepsilon^{-1} \nabla \times \boldsymbol{H} = -\mu \frac{\partial^2 \boldsymbol{H}}{\partial t^2} + \nabla \times \varepsilon^{-1} \boldsymbol{J} \quad (8)$$

These equations link the spatial variations of the fields to their time evolution, and they are the only equations needed to simulate the evolution of the electromagnetic fields in time if the initial conditions verify the two divergence equations. More on this can be found in any electromagnetics textbook[1].

## b) The many facets of the wave equation

Although quite simple in appearance, the wave equation leads to a wide variety of complex electromagnetic phenomena. Only very specific cases can be solved analytically, and full-field numerical simulations can be extremely computationally intensive for simulations larger than a few tens of wavelengths. Depending on the application, the wave equation can either be studied in the time domain or the frequency domain. While the first is appropriate for the simulation of light pulses or for FDTD, the wave equation in the **frequency domain** can accurately describe most phenomena that don't vary significantly at the time scale of a few optical cycles, of which are all phenomena studied in this work. Various approximations of the wave equation have been developed to understand light propagation in specific cases. Below are a few examples:

1) **Classical (ray) optics[2]**: when light propagates in the air or in objects with dimensions much larger than the wavelength or with very slow refractive index variations, the light path can be approximated as a ray following the **Snell-Descartes laws**.
2) **Fourier optics[3]** relies on the decomposition of the electromagnetic field into an infinite number of plane-waves, whose propagation in vacuum can be described analytically. Fourier

optics is typically used to compute the far-field from a source under the paraxial approximation (see below).

3) **Helmholtz optics** is based on the **paraxial** (or slowly varying envelope) **approximation[4]**, valid when electromagnetic radiation behaves approximately like a plane-wave. Under this condition the vector field **E** can be decomposed into a product of a plane wave and a slowly varying envelope function u:

$$\mathbf{E(r)}=\mathbf{u(r)}\exp(ikz) \tag{9}$$

Where k is the magnitude of the wave vector, for a wave propagating mainly in z-direction. k is such that $k^2 = w^2 \varepsilon_0 \mu_0$, with w the frequency of the wave, $\varepsilon_0$ and $\mu_0$ the permittivity and permeability of the main propagation medium. In this situation, electromagnetic radiation can be described the **paraxial wave equation**:

$$\nabla_\perp^2 \mathbf{u} + 2ik\frac{\partial \mathbf{u}}{\partial z} + w^2(\varepsilon-\varepsilon_0)(\mu-\mu_0)\mathbf{u}=0 \tag{10}$$

Where $\nabla_\perp = \frac{\partial^2}{\partial x^2} + \frac{\partial^2}{\partial y^2}$ is the transverse Laplacian, and the last term can be omitted when the wave propagates in a uniform medium. Using **the paraxial approximation allows to reduce drastically computational costs** when doing numerical analysis as the envelope needs much sparser spatial sampling than the amplitude. This approximation is widely used to model beams, diffraction patterns from apertures, propagation into waveguides or fiber optics with small perturbations…

4) **Periodic diffractive optics[5]**: when light goes through a grating, which is a periodic structure with a period larger and the same order of magnitude as the wavelength, light is diffracted into multiple diffraction orders following the **grating equation**:

$$d(\sin\theta_i + \sin\theta_d) = n\lambda \tag{11}$$

Where d is the grating period, $\theta_i$ and $\theta_d$ are the incident and diffracted angles, n is the grating order and $\lambda$ is the wavelength. The power diffracted in each order can be found by solving the wave equation in the grating unit cell with **periodic boundary conditions**, and then information about the whole grating and far-field propagation is trivially deducted. Gratings are used to design polarizers, wavelength separation…

5) **Photonic crystals (PCs)[6]**: are also periodic structures (with period larger than the wavelength), but unlike gratings light propagates (or not) through PCs, interacting and being diffracted by each lattice block. Propagation in the whole PC can be inferred from the solution of the wave equation in a unit cell using **Bloch boundary conditions** on the field, ie:

$$\mathbf{E}(\mathbf{r}+\mathbf{R}) = \exp(i\mathbf{k}\mathbf{R})\,\mathbf{E}(\mathbf{r}) \tag{12}$$

Where **k** is the wavevector and **R** is any lattice vector. Like in semiconductors, this equation leads to a **band-structure behavior**. PCs are typically used for on-chip photonics.

6) **Metamaterials[7]** are basically photonic crystals with **lattice constant much smaller than the wavelength**, such that electromagnetic radiation does not undergo diffraction (only $0^{th}$ order). Each lattice block of a metamaterial can then be described as its own artificial material with **electromagnetic properties $\varepsilon$ and $\mu$ depending on the structure rather than the materials involved**.

7) **Metasurfaces[8, 9]** are subwavelength-thick devices that modulate the phase of an incoming electromagnetic radiation going through or being reflected by it. Metasurfaces are typically made of a semi-periodic arrangement of building blocks with various sizes and shapes, so that each block can induce a discrete phase change between 0 and $2\pi$ (modulo $2\pi$) to electromagnetic radiation that goes through (or reflected by) it. Any optical functionality that can be described by a **phase transfer function** $\Delta\phi(x,y)$ can then be achieved by a metasurface once the **building block dictionary** has been established (typically with full field simulations). Metasurfaces have been used to replicate classical optics devices such as lenses, axicons, holograms, polarizers…

8) **Transformation optics[10]** is a technique that allows to transform a known propagation mode of electromagnetic radiation into another one if the phase of the field in the latter can be expressed as a coordinate transformation of the phase in the first. Coordinate transformations for the phase can be achieved with permittivity and permeability transformations and lead to a change in field amplitude following **transformation optics equations[11, 12]**. This technique has been used for the design of optical cloaks, in combination with the use of metamaterials to emulate the wide range of permittivities and permeabilities needed.

9) **Nonlinear optics[13]** describes the behavior of light in nonlinear materials, where the polarization is not linearly proportional to the field, and where new processes that cannot be described by the linear wave equation (7 and 8) happen, such as frequency mixing, Kerr effect or Raman amplification. The nonlinear wave equation for the electric field with an isotropic space, no free charges and non-magnetic materials writes:

$$\nabla\times\nabla\times\mathbf{E}+\frac{n^2}{c^2}\frac{\partial^2}{\partial t^2}\mathbf{E}=-\frac{1}{\varepsilon_0 c^2}\frac{\partial^2}{\partial t^2}\mathbf{P^{NL}} \quad (13)$$

Where n is the index of refraction, c is the speed of light and $P^{NL}$ is the non-linear polarization, which is typically a polynomial function of the field. Due to the coupling between several wavelengths, the nonlinear wave equation is better studied in the time-domain.

10) **2D wave equation** can describe accurately the behavior of planar devices where the structure varies in the x-y plane and stays uniform in the z-direction, apart from boundary conditions, such as most etched on-chip photonic devices, or polarization-sensitive gratings that vary in a single direction. In many cases, the 2D equation can accurately describe the device with much lower computational complexity. In particular, any field propagating in-plane can be described by its transverse field components, $H_z$ for TE polarization and $E_z$ for TM polarization, which are scalars. **The 2D problem can then be decomposed into two scalar wave equations**, one for each polarization, shown here in the frequency domain:

$$(\nabla\times\mu^{-1}\nabla\times - \varepsilon w^2)E_z=-iwJ \quad (TM) \tag{14}$$

$$(\nabla\times\varepsilon^{-1}\nabla\times - \mu w^2)H_z=-iw\,\nabla\times\varepsilon^{-1}\,J \quad (TE) \tag{15}$$

11) **Transverse modes** of a structure uniform along the z-direction ($\varepsilon,\mu(x,y,z) := \varepsilon,\mu(x,y)$) describe the ways that electromagnetic radiation can propagate in this direction without changing its amplitude, such that the field follows:

$$\mathbf{E}(x,y,z)=\mathbf{E}(x,y)\exp i\beta z \tag{16}$$

where $\beta$ is the propagation constant. The shape of the modes can then be found by solving the eigenequation (with $\beta$ the eigenvalue) derived from the wave equation in the transverse plane by replacing the z-derivatives by $i\beta$.

## c) Electromagnetic solvers

Based on those approximations, multiple computational techniques have been designed to model electromagnetic radiation, from full-field simulations to ray optics.

1) **Finite-differences in the Time-Domain[14]** (FDTD): is a full-field simulation that studies the propagation in time of an electromagnetic pulse in the structure. From that the propagation in the frequency domain can be retrieved with a Fourier transform. This technique has been leading for the modelling of devices where rectangular grids can be used accurately.
2) **Finite element method[15]** (FEM): uses unstructured grids (for example with triangles and tetrahedron) that allows to model more complex structures than FDTD, especially when mesh accuracy can vary a lot. This technique has a higher computational cost due to the more complex relationships between adjacent cells.
3) **Method of moments[16]** (MOM): uses Green functions to compute the field produced by a source or scattered by an object (typically a conductor). This method works only when the field propagates in open space, so the field in any point can be expressed as the convolution of the Green function and the sources. This method is then much faster than the other methods and does not need the implementation of boundary conditions.
4) **Finite-Difference in the Frequency Domain[17-19]** (FDFD): solves the monochromatic wave equation by converting it to a **linear system with matrix form Ax = b**, where A represents the wave equation, x is the field and b is the source term. The method can also be used to find the normal modes of a structure in the absence of sources, by solving the (N-1)-dimensional eigenproblem $Ax = w^2x$ where w is the propagation constant and N is the

dimension of the space. **This technique is behind both inverse and forward simulations in this work.**

5) **Rigorous Coupled-Wave Analysis[20, 21]** (RCWA): is a semi-analytical Fourier-space method that describes the field as a combination of plane-waves (or more generally spatial harmonics) with different wave-vectors, which can be very efficient for simulations of gratings and photonic crystals with periodic/Bloch boundary conditions.
6) **Beam Propagation Method[22-24]** (BPM): relies on the solution of the paraxial wave equation. Both spatial domain and frequency domain methods have been implemented. The method is mainly used to simulate shaped (bent, tapered) waveguide structures with slow variations and small propagation angles. Numerical sampling of the slowly varying envelope can be more efficient than sampling the field by many orders of magnitude, depending on the variations of the envelope function.
7) **Transfer Matrix Method** (TMM): is used to analyze the propagation of electromagnetic radiation through a stratified medium (1D photonic crystal) by considering boundary conditions at each interface.
8) **Ray tracing**: is the most widely used method to simulate and design optical elements based on classical optics, such as lenses, mirrors and even more complex devices that can be reduced to a black box behavior such as polarizers or scattering media. The method relies on sending multiple rays of various wavelengths and directions from the source and simulate their propagation into the optical media.

Although they use very different approximations, all the numerical methods above are **forward simulations:** they study the **propagation of the field from a given source into a given**

**structure or device**. Many simulation methods have been first developed to understand the interaction of electromagnetic waves with objects, such as prisms, gratings, planes… Then, with more experience and advanced fabrication techniques, these methods have allowed to design and make various types of electromagnetic devices.

## d) Electromagnetic devices

Any electromagnetic device can be defined by the **transformation of an input signal into an output signal** in specific parts of the space. The device behavior is described by the propagation of this signal and its interaction with the device's material (ε and μ for a linear material), following the wave equation. **Figure 1.1** shows a schematic representation of an electromagnetic device.

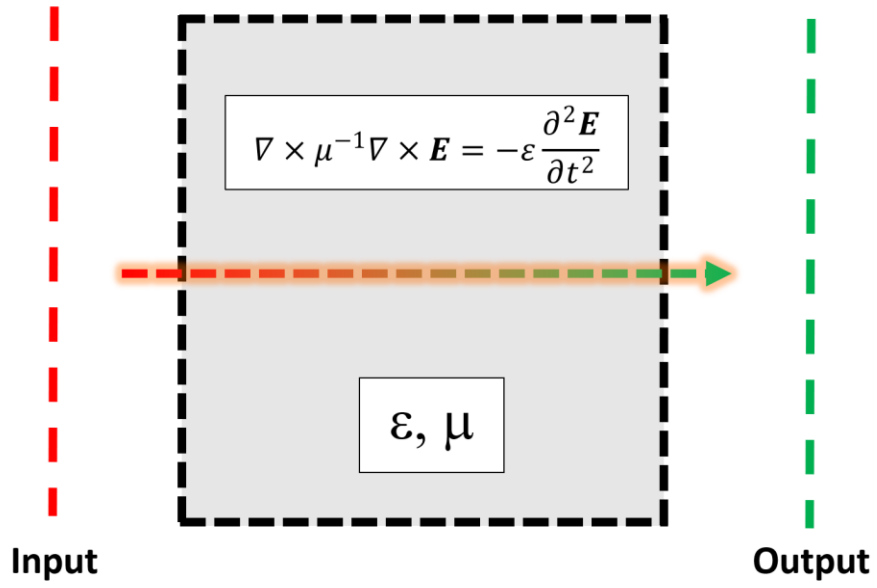


***Figure 1.1.*** *Schematic representation of an electromagnetic device, which is a "black-box" filled with material with varying optical properties (ε, μ), which transforms a given optical input into an optical output following the wave equation.*

It is important to note that there can be many ways to transform a given input into a desired output. Therefore, each class of device can be achieved in multiple ways. Next, we describe a few types of electromagnetic devices:

1) **Nonlinear devices** are described by a nonlinear wave equation (such as eq. 13), where the physics of the device depends on the non-linear polarization term. Typically, nonlinear devices are based on resonators with high Q-factors to generate very intense electric fields in the nonlinear materials. Those intense fields induce effects such as frequency conversion, or index change (Kerr effect). For example, an input with two high power waves (plane waves, Gaussian beams, waveguide modes…) with different wavelengths $\lambda_1$ and $\lambda_2$, can output a combination of waves with wavelengths $\lambda_1$, $\lambda_2$, $\lambda_1+\lambda_2$, $|\lambda_1-\lambda_2|$.
2) **Magnetic devices** are devices where the permeability $\mu$ is not equal to the vacuum permeability $\mu_0$. Magnetic materials typically operate at low frequency (a few Hz to microwaves), but recently metamaterials have allowed to create artificial magnetic materials in the THz or infrared. In this work will only consider non-magnetic materials.
3) **Lasers** are devices where the optical input comes from within the material and boundaries have only outputs. They rely on optical gain from stimulated emission to amplify light intensity in the gain material, such as a semiconductor with population inversion. The optical gain can be easily modelled with a complex permittivity where the imaginary part is negative. However, modelling a laser is a multiphysics problem, where one must also consider the semiconductor physics of electron recombination.

4) **Absorbers** such as solar cells, photodetectors or metals are devices with input electromagnetic radiation and no or a smaller output power. They follow similar physics as lasers, but the imaginary part of the permittivity is positive.
5) **Metallic devices at low frequencies[25, 26]** (compared to the plasmonic devices) are devices with mostly imaginary permittivity, such that electromagnetic radiation cannot penetrate in it. They behave like perfect electric conductors, where **E** field can only be perpendicular and **H** field can only be parallel to the surface. Mirrors are based on metals. Antennas can have multiple functions, such as producing spherical waves (dipole antenna) generating and directing electromagnetic beams or collecting it (Horn antennas), or just scattering incoming radiation. Metals are typically close to perfect electric conductors at THz or lower frequencies and depending on the length of propagation in terms of number of wavelengths (the longer the more absorption).
6) **Plasmonic devices[27, 28]** are devices based on metals (often metal/dielectric assemblies) where light penetrates significantly inside the metal, which means the permittivity is not too large and can even be positive at very short wavelengths. Plasmonic devices can be very good absorbers due to their complex permittivity. They also make good sensors and can enhance nonlinear processes, as they can focus light far below the diffraction limit, which generates a strong field enhancement.
7) **Metamaterials** are artificial materials made of a periodic arrangement of "cells" of structured materials, usually combining metals and dielectrics. If the wavelength of the radiation is much larger than the unit cell, light will interact with it like with any bulk material, but with a permeability and a permittivity defined by the structure of the unit cell rather than the materials.

For example, a metamaterial can be made magnetic without using any magnetic material. A famous use of metamaterials is the practical realization of an electromagnetic cloak in the microwaves[29, 30]. Full-field simulations of a metamaterial unit cell with periodic boundary conditions and under incoming plane-wave excitation allow to retrieve the scattering parameters (absorption, reflection, transmission), which in turns gives access to the effective $\varepsilon$ and $\mu$[31].

In this work, we will consider **much simpler devices based on linear isotropic non-magnetic dielectric materials that guide or scatter light without any absorption, i.e. real $\varepsilon > 0$ and $\mu=\mu_0:=1$**, such as the devices described below:

8) **Waveguides[32] and optical fibers[33]** are devices that can guide light along a high-index "core" surrounded by a low index material (air, SiO2…) or a photonic crystal. Typically, those devices are uniform along the propagation direction, and light propagation can be described by the "modes" of the structure along a transverse plane. Waveguides and optical fibers are ubiquitous for telecommunications and transport of information in general.
9) **On-chip photonic devices[34, 35]** are devices that couple or manipulate light on-chip. Light can be coupled on-chip directly from free-space to waveguide (often using a taper), where the input is a focused beam (typically Gaussian) and the output is a waveguide mode, both propagating in the same direction. Light can also be coupled from the top using a grating, which can be designed for any angle of incidence. Once light is coupled to the waveguide, it can be manipulated in multiple ways by various devices. A y-junction can split the power from one to two waveguides identically. A (de)multiplexer can combine (separate) the signals from multiple (one) input waveguides into one (multiple) other waveguide(s) depending on the

wavelength, polarization or mode. A ring resonator can select a very specific wavelength and amplify the optical power at resonance… All these devices connect input waveguides to output waveguides, by splitting, routing or modifying the modes.

10) **Gratings** are periodic devices that can add transverse momentum to plane-waves, deflecting it into various diffraction orders following the grating equation (Equation 11). Input and output plane-wave angles are the only information needed to describe the behavior of a grating. Gratings are often used to separate wavelengths in white light. Gratings that are periodic in one direction and uniform in the other often have a very strong polarization-sensitive behavior, making good polarizers…
11) **Lenses** are devices that can transform a plane-wave electromagnetic radiation into a cylindrical (2D) or spherical (3D) wave which is focused at a specific focal spot.

In the last few decades, a lot of powerful photonic and electromagnetic devices have been designed thanks to the improved understanding of the wave equation, and the growing numerical simulations capabilities. However, most of those devices are still designed by **forward methods**, where a device geometry is first proposed, then simulated, then modified in order to optimize the performance, in a lengthy trial-and-error process. It is often done "by hand", based on intuitive geometries, using parameter sweeps to optimize the shapes and sizes of a few individual components, such as the ring resonators, photonic crystals or bowtie antennas shown in **Figure 1.2**. On the other hand, analytical methods such as transformation optics lead to very unpractical devices with material characteristics that cannot be achieved by normal materials. This has motivated the field of metamaterials, but with little practical success. Furthermore, many complex optical functionalities cannot be achieved by classical design methods, or with mediocre

performance at best. These are the main reasons why **an automated method is desired for the design of electromagnetic devices, which we propose and describe in the next chapter**.

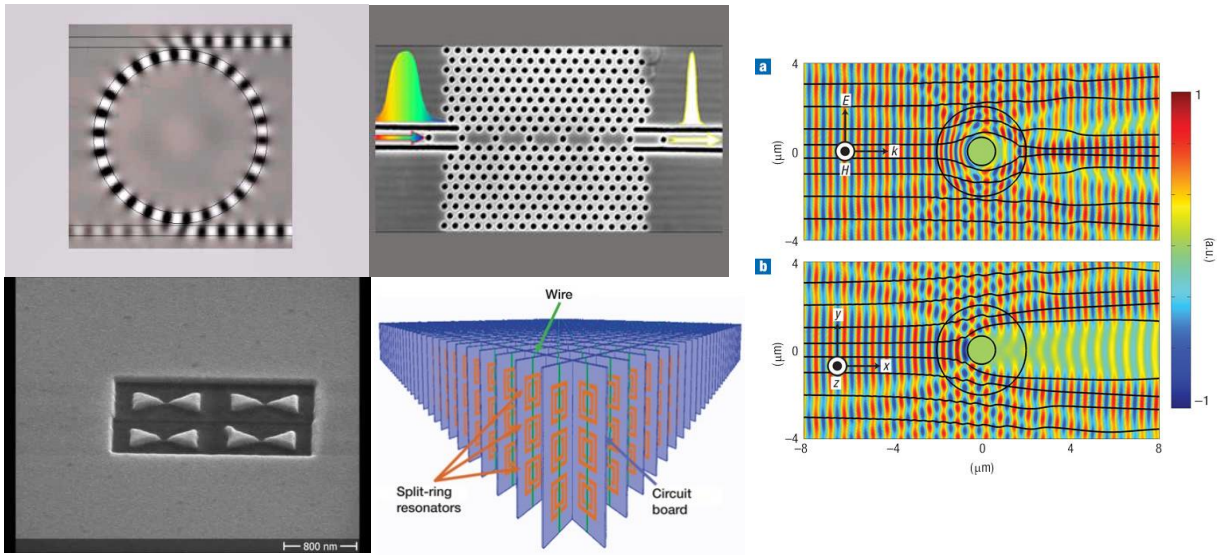


***Figure 1.2.*** *A few examples of electromagnetic devices. From left to right, top to bottom: a microring resonator, a photonic crystal, an optical cloak, bowtie nano-antennas and a negative index metamaterial.*

# II) Inverse-design: theory

## a) Definition

**An electromagnetic inverse-design method is an optimization method that allows, given a set of inputs ($\mathbf{E_{in}}$, $\mathbf{H_{in}}$, $\varepsilon_{in}$, $\mu_{in}$) and a set of desired outputs ($\mathbf{E_{out}}$, $\mathbf{H_{out}}$), to find a device structure ($\varepsilon$, $\mu$) which converts the inputs into the desired outputs following the wave equation, and potentially some constraints.** $\mathbf{E_{in}}$ and $\mathbf{H_{in}}$ are the input electric and magnetic fields, respectively. $\varepsilon$ and $\mu$ are the permittivity and permeability, respectively.

Let us break this definition into the main keywords:

**1) The outputs** can either be specific fields $\mathbf{E_{out}}$ and $\mathbf{H_{out}}$, or a function of those fields $\mathcal{F}$, such as an output power. In the latter case, the output can be a strict equality, or an inequality, such as a minimum power. The output materials $\varepsilon_{out}$, $\mu_{out}$ are typically fixed.

**2) The wave equation** that is used in this work is the steady-state wave equation (frequency-dependent) with linear isotropic materials and in the absence of currents. There are two equivalent versions of the wave equation for electric and magnetic fields:

$$\nabla\times\mu^{-1}\nabla\times\mathbf{E}=w^2\varepsilon\mathbf{E} \quad (1)$$

$$\nabla\times\varepsilon^{-1}\nabla\times\mathbf{H}=w^2\mu\mathbf{H} \quad (2)$$

Let us consider equation (1). As can be seen, it has three unknowns, $\varepsilon$, $\mu$ and $\mathbf{E}$, and there is no way to transform this equation into a linear system, as shown in Appendix A. As a result, **there is**

**no known way to find an exact solution to this equation given a set of boundary conditions**. All that can be done is find approximate solutions using optimization techniques.

**3) The basic optimization objective** can be written, for equation (1) as:

$$\min_{\varepsilon,\mu} \| F(\mathbf{E_{out}}) - F_{ideal} \| \quad (3)$$

**4) Constraints and regularizations** can be added to the optimization objective, such as keeping the material parameters real, or bounded by certain values, or to decrease the material or field variations.

## b) Topology optimization vs objective-first

The most straightforward way to minimize the optimization objective (3) is to iteratively find the gradient of this objective with respect to the material parameters and update the device materials using gradient-descent. This approach has been commonly called **topology optimization[36-48]** in scientific literature, and it has been solved using adjoint-based gradient-descent. However, this method tends to converge towards the first local optimum it encounters, without being able to "escape" from it, which requires to either start from a good structure to optimize, or to try a lot of random starting points to get a good solution[49]. Jonathan Fan's group has combined topology optimization with rigorously-coupled wave analysis (RCWA) to successfully design, analyze and fabricate high-efficiency high-index metasurfaces[50-53].

The alternative method, which is employed in this work, is to reverse the roles of the output objective and the wave equation. The **output objective becomes a fixed constraint**, and **the wave**

**equation becomes the optimization objective**. Unlike topology optimization, both material and field variables are optimization variables. The problem can then be written:

$$\min_{\varepsilon,\mu,\mathbf{E}} \left\| \nabla \times \mu^{-1} \nabla \times \mathbf{E} - w^2 \varepsilon \mathbf{E} \right\| \quad (4)$$

given fixed $\mathbf{E_{bnd}}$, $\varepsilon_{bnd}$ and $\mu_{bnd}$ and constraints on $\varepsilon$, $\mu$

This method, called **objective-first inverse-design**, has been pioneered by Vuckovic's group[54-60]. As opposed to topology optimization, **it optimizes the performance of the device indirectly by minimizing the physics residual in the wave equation**. Therefore, a forward simulation is needed after optimization to verify the performance of the device with "physical fields". Instead of fixing boundary conditions exactly, one could also define inequality-based constraints on it, but we will only consider fixed constraints in this work.

## c) Separation of the problem into linear sub-problems

As discussed in Appendix A, the problem (4) is non-convex, which is a **NP-hard problem to solve**. As a result, there is no known way to find the optimal solution. In order to find an approximate solution, we can **decompose it into three linear sub-problems by fixing two variables and optimizing for the third one.** Doing this alternatively for each variable will lead to a decrease of the physics residual at each step, and often to a good result in terms of the desired output objective, as shown in chapter X. The three linear sub-problems can be written, at time step n:

$$\min_{\mathbf{E_{int}}^{(n)}} \left\| A\left(\varepsilon^{(n-1)}, {\mu^{-1}}^{(n-1)}\right) \mathbf{E_{int}}^{(n)} + a\left(\varepsilon^{(n-1)}, {\mu^{-1}}^{(n-1)}, \mathbf{E_{bnd}}\right) \right\| \quad (5)$$

$$\min_{\varepsilon^{(n)}} \left\| B\left(\mathbf{E}^{(n)}\right)\varepsilon^{(n)} + b\left({\mu^{-1}}^{(n-1)}, \mathbf{E}^{(n)}\right) \right\| \quad (6)$$

$$\min_{{\mu^{-1}}^{(n)}} \left\| C\left(\mathbf{E}^{(n)}\right){\mu^{-1}}^{(n)} + c\left(\varepsilon^{(n)}, \mathbf{E}^{(n)}\right) \right\| \quad (7)$$

where A, B and C are operators such that:

$$A(\varepsilon,\mu) = \nabla \times \mu^{-1} \nabla \times - w^2 \varepsilon \quad (8)$$

$$B(\mathbf{E}) = -w^2 \mathbf{E} \quad (9)$$

$$C(\mathbf{E}) = \nabla \times (\nabla \times \mathbf{E}) \quad (10)$$

In equations (7, 10), we have exchanged the positions of $\mu^{-1}$ and $\nabla \times \boldsymbol{E}$ because their product is commutative (the matrix representation of $\mu$ is diagonal). a, b and c are vectors:

$$a(\varepsilon,\mu^{-1},\mathbf{E_{bnd}}) = A(\varepsilon,\mu)\mathbf{E_{bnd}} \quad (11)$$

$$b(\mu^{-1},\mathbf{E}) = C(\mathbf{E})\mu^{-1} \quad (12)$$

$$c(\varepsilon,\mathbf{E}) = B(\mathbf{E})\varepsilon \quad (13)$$

and where the total field is the sum of the boundary field and the variable interior field:

$$\mathbf{E}^{(n)} = \mathbf{E_{int}}^{(n)} + \mathbf{E_{bnd}} \quad (14)$$

These three problems are in the form min(||Ax+b||), which can be solved numerically, up to a rounding error, by **traditional linear optimization methods**. Although the problem is shown

here with the electric field, the same approach can be used with the magnetic field, where equation (1) is replaced by (2). The matrix formulations of these problems are presented in Appendix A.

**For the rest of this work, we will only consider non-magnetic materials**, where $\mu = \mu_0 := 1$ (with appropriate units), so that the third sub-problem can be discarded.

Next, we will present variations and enhancements of this problem.

## d) Enhancements to the optimization

**1) The initial conditions** ($\varepsilon^{(0)}$ or $\mathbf{E^{(0)}}$) have a significant impact on the final structure/field after optimization. This will be illustrated in chapter 3 with the optical diode design. As it is quite hard to design a realistic initial field, we only study here initial permittivities. In this work, we mainly start from constant permittivities across the whole design space, but one could also consider starting from random permittivities, or from manually designed devices.

**2) The order** of the sub-problems in the optimization can be chosen different from the one shown above, but it is recommended to start with the field optimization $\mathbf{E_{int}^{(1)}}$, so that there is no need to provide a realistic initial field $\mathbf{E^{(0)}}$ to the optimization.

**3) The field** of the optimization can either be the electric field, as shown above, or the magnetic field. This is a crucial decision when doing the optimization in 2D. In that case, electromagnetic waves can be decomposed into TE and TM components with scalar transversal fields, which greatly simplifies the calculations and visualization.

**4) Constraints** can be added to the optimization variables if they are compatible with the optimization algorithm. For example, if Matlab's linear least-squares solver is used to minimize ||A.x+b||, constraints on x of the shape B.x <= b, or C.x = c, or low <= x <= up. These can be used to limit the range of permittivities available or set a maximum for the norm of the field, or set a specific field in some parts of the space.

**5) Additional costs** can be added to the optimization objective, under the condition that those costs are convex with respect to the optimization variable. This approach can replace hard constraints, providing more flexibility. As opposed to hard constraints, optimization is still done in the full design-space, but structures that minimize the additional costs will be favored. We use this approach mainly for binarization and regularization, which are detailed below.

**6) Multiple objectives** can be used when one wants to design devices to achieve multiple functionalities, such as the optical diode described in the next chapter. In that case, the N×1 vectors that represent the field and the source term in equations (4-14) are replaced by N×k vectors where N is the number of pixels of the design-space and k is the number of objectives. In equations (5-13), the N×N matrices A, B and C are replaced by kN×N matrices, and vectors a, b and c become kN×1 vectors.

## e) Binarization

The proposed inverse-design algorithm converges towards structures with a continuous spectrum of permittivities. In all cases that we will consider in this work, **the permittivity is constrained between two real positive bounds: $\varepsilon_{low} < \varepsilon < \varepsilon_{high}$,** which is compatible with convex optimization. However, in most practical situations, one wants to build devices made of only two

or a few specific materials. In silicon photonics, for example, these materials are silicon, and air or silicon dioxide. We can use a simple **"cutoff" approach to transform a continuous structure into a binary structure**. The optimization is done with a continuous permittivity range where the boundaries $\varepsilon_{low}$ and $\varepsilon_{high}$ are the two design materials. Then, all pixels with permittivity lower than the cutoff are set to $\varepsilon_{low}$ and all pixels with permittivity higher are set to $\varepsilon_{high}$. As can be seen with the optical diode, this approach does not usually yield good results: the conversion from continuous to binary must be a bit subtler.

Instead of converting to binary after optimization, we modify the algorithm to **incentivize the design of devices "close to binary"**. As explained in previous part, we can add any cost that is linear or convex with respect to the variables. Therefore, we would like to implement a cost function that is inversely proportional to how binary the device is. However, such a function would have two minima at $\varepsilon_{low}$ and $\varepsilon_{high}$, which cannot be achieved with a convex function other than a constant.

We choose an intermediate approach where **we define the cost as the difference between the optimized structure at timestep n and a binary structure obtained by the cutoff method at timestep n-1**. This transforms the second equation into:

$$\min_{\varepsilon^{(n)}} \left\| B\left(\mathbf{E^{(n)}}\right)\varepsilon^{(n)} + b\left(\mathbf{E^{(n)}}\right) \right\| + \lambda_{bin} \left\| \varepsilon^{(n)} - \varepsilon_{bin}{}^{(n-1)} \right\| \quad (15)$$

This cost function is linear with $\varepsilon$, so the same optimization algorithm can be used. $\lambda_{bin}$ is an hyperparameter, which we call **binarization coefficient**, that can be changed to adjust the strength of the binarization. Typically, $\lambda_{bin}$ is small or null at first as one wants the algorithm to focus on the optimization task. Once the algorithm has converged towards a stable structure,

typically after a few tens or hundreds of iterations, $\lambda_{bin}$ can be increased to start the binarization process. The algorithm will favor structures that resemble the "dumb" binary structure obtained with the cutoff, but the primary optimization objective still plays its role to avoid that the binarization strongly impacts performance. If $\lambda_{bin}$ is chosen carefully, a good binarization can be done in a few tens to hundreds of iterations, meaning that the resulting structure is "almost binary" and that the performance after "cutoff" binarization is almost the same. In order to evaluate how close to binary a structure is, we define a metric:

$$B=2\left\|\frac{\varepsilon-\varepsilon_{mid}}{\varepsilon_{high}-\varepsilon_{low}}\right\| \tag{16}$$

This binary metric is equal to 1 when the structure is totally binary, and 0 if the structure's permittivity is constant and equal to $\varepsilon_{mid} := (\varepsilon_{high}+\varepsilon_{low})/2$. In our algorithm, this binary metric is used to adjust the value of the binarization coefficient, such that:

$$\lambda_{bin}{}^{(n)}=\frac{\lambda_0}{1-B^{(n-1)}} \tag{17}$$

This way, even as the structure gets more and more binary at each iteration, the binarization cost will stay roughly constant, $\approx \lambda_0$. Empirically, this prevents the binarization to gets slower and slower the more binary the structure is.

Finally, let us note that binarization using **E** or **H** are very different. If $1 < \varepsilon < 12$, permittivities of $\varepsilon=2$ and $\varepsilon=11$ would have the same binary cost in the first case, with $\varepsilon_{mid} = 6.5$. In the second case, given that the optimization is done on $\varepsilon^{-1}$, $\varepsilon=11$ would have the same cost as $\varepsilon=1.008$, and $\varepsilon_{mid} \approx 1.85$.

## f) Regularization

A loss function proportional to the variations in the structures can be added to the optimization cost to incentivize simpler structures with less boundaries. For example, this will prevent single or few-pixels sub-structures, and parts of the structures that have negligible impact on the performance. In our implementation, the regularization cost is:

$$\lambda_{reg}\left(\|D_x\varepsilon\|+\|D_y\varepsilon\|+\|D_z\varepsilon\|\right) \quad (18)$$

where $\lambda_{reg}$ is the **regularization hyperparameter**, $D_x$, $D_y$ and $D_z$ are derivative matrices such that $D_x\varepsilon\ (x,y,z) = \varepsilon(x+1,y,z) - \varepsilon(x,y,z)$ where x, y and z are integer coordinates of the pixels in the design space.

## g) Acceleration

The algorithm as presented can be a bit slow to converge. We have implemented a simple "hack" to speed up convergence. Every two iterations, we accelerate the evolution of the field:

- $\mathbf{E_{int}^{*(n)}}$ is computed from $\mathbf{E_{int}^{(n-1)}}$ by minimizing equation (5)
- $\mathbf{E_{int}^{(n)}} := \mathbf{E_{int}^{(n-1)}} + \lambda_{acc}\ (\mathbf{E_{int}^{*(n)}} - \mathbf{E_{int}^{(n-1)}})$

where $\lambda_{acc}$ is the acceleration hyperparameter, and $\lambda_{acc} = 1$ corresponds to no acceleration. We found this technique to speed the convergence significantly with an optimal value of $\lambda_{acc} = 5$. If the value is too large, oscillations of the field/structure will appear, similar to what would happen in gradient-descent with a large learning rate. Furthermore, this method often yields not only faster

but also better results. Intuitively, the acceleration acts like a perturbation of the regular optimization, which can help get out of local minima.

## h) Finite-differences implementation in 3D

In order to numerically solve the equations presented in this chapter and design electromagnetic devices, one needs to define a design-space with discrete coordinates, called a grid. In this work, we will work with a cubic grid, or **square grid** in 2D. **We will call points of the design-space "pixels", defined by integer coordinates x, y and z**. **We choose the space unit to be the size of a pixel** (always 1), and the link to physical dimensions is described by the wavelength in vacuum $\lambda_0$, expressed in number of pixels, and such that:

$$k_0 = \frac{2\pi}{\lambda_0} \tag{19}$$

**A good choice for $\lambda_0$ is $10n_{max}$: 10 times the maximum index of refraction of the structure**. A larger $\lambda_0$ will allow better numerical precision at the expense of the computation time. In order to perform the calculations, we work with the **Yee grid[61]**, which is a choice of the location of the field components at specific points inside a pixel. In the pixel (x, y, z) = (0, 0, 0), the coordinates of the fields components are $E_x$(0.5, 0, 0), $E_y$(0, 0.5, 0), $E_z$(0, 0, 0.5), $H_x$(0, 0.5, 0.5), $H_y$(0.5, 0, 0.5) and $H_z$(0.5, 0.5, 0). This choice allows to minimize the numerical error when computing finite differences, proportional to $\lambda_0^{-2}$.

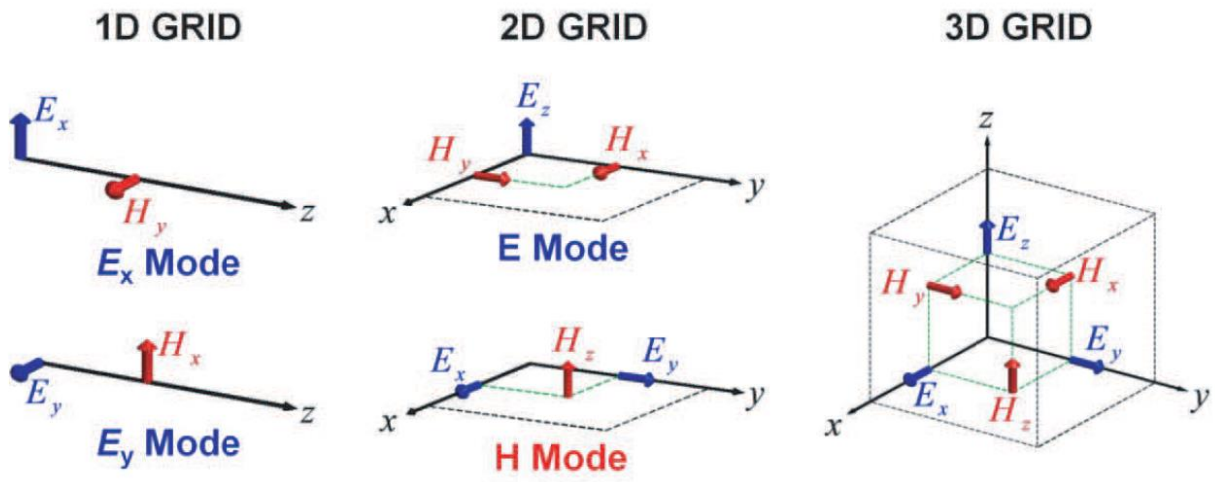


***Figure 2.1.*** *Representation of a unit-cell of the Yee grid for one, two or three-dimensional spaces. The three components of the vectors E and H are each at a different position in space, with half coordinates.*

With this choice of coordinates, it is easy to see that finite differences are going to be different for E-field and for H-field. In short, finite-differences with E will involve the current and next pixel in space, while finite-differences with H will involve the current and previous pixel in space. Here we show how this works for the H curl equation projected on z:

$$\nabla\times\mathbf{H}=i\omega\varepsilon E \;\rightarrow\; \frac{\partial H_y}{\partial x}-\frac{\partial H_x}{\partial y}=i\omega\varepsilon E_z$$

$$\rightarrow \left[H_y(0.5, 0, 0.5)-H_y(-0.5, 0, 0.5)\right]-\left[H_x(0, 0.5, 0.5)-H_x(0, -0.5, 0.5)\right]=i\omega\varepsilon E_z(0, 0, 0.5) \quad (20)$$

It makes sense that the coordinate of Ez is the middle of the coordinates of the two $H_y$ and the two $H_x$ involved in the finite differences. As finite differences are different with **E** and **H**, we define 6 matrix operators $D_x^E$, $D_y^E$, $D_z^E$, $D_x^H$, $D_y^H$ and $D_z^H$ to handle finite-differences with both fields along each space dimension. The matrix representations of those operators can be found

in[62], along with explanations about the boundary conditions. With these notations, the wave equation on the electric field can be written:

$$\begin{pmatrix} 0 & -D_z^H & D_y^H \\ D_z^H & 0 & -D_x^H \\ -D_y^H & D_x^H & 0 \end{pmatrix} \begin{pmatrix} 0 & -D_z^E & D_y^E \\ D_z^E & 0 & -D_x^E \\ -D_y^E & D_x^E & 0 \end{pmatrix} \begin{pmatrix} E_x \\ E_y \\ E_z \end{pmatrix} = w^2 \begin{pmatrix} \varepsilon_x & 0 & 0 \\ 0 & \varepsilon_y & 0 \\ 0 & 0 & \varepsilon_z \end{pmatrix} \begin{pmatrix} E_x \\ E_y \\ E_z \end{pmatrix} \quad (21)$$

The first matrix is the curl operator for the H-field and the second matrix is the curl operator for the E-field. The third matrix can have different shapes. If the permittivity is assumed to be uniform in each pixel, then we have $\varepsilon_x = \varepsilon_y = \varepsilon_z = \varepsilon$. If we assume the permittivity to vary continuously across the device, then we can create "averaging" operators Mx, My, Mz that will compute the permittivity at the relevant location as the interpolation of permittivities at integer coordinates, such that $\varepsilon_x = M_x\varepsilon$, $\varepsilon_y = M_y\varepsilon$ and $\varepsilon_z = M_z\varepsilon$. For example, the interpolation of $\varepsilon_x$ is:

$$\varepsilon_x(0.5, 0, 0) = (M_x\varepsilon)(0,0,0) = \frac{1}{2}\big(\varepsilon(0,0,0) + \varepsilon(1,0,0)\big) \quad (22)$$

In equation 21, the third matrix is a diagonal matrix, so the matrix product could also be written as an element-wise vector product between ε and **E**. Note that each ε or **E** vector here represents a "flattened" 3-dimensional permittivity or field. The matrix representation of the wave equation with H-field can be found in Appendix A.

## i) Finite-differences implementation in 2D

In the following work, we focus on the design of planar structures, which means 3-dimensional structures where the permittivity is uniform along the vertical dimension. Furthermore, we assume that incoming electromagnetic radiation travels in-plane, which means it

does not have any vertical momentum. Under those conditions, electromagnetic devices can be described by a 2-dimensional wave equation in the x-y plane. Furthermore, it can be shown that **any electromagnetic wave in 2D can decomposed into two components that can each be described by the scalar vertical field**: the Transverse Electric (TE) wave, described by $H_z$ only, and the Transverse Magnetic (TM) wave, described by $E_z$ only. Dealing with scalar fields has the great advantages of simplifying the computations (the matrices are smaller) and the visualization of the results. The matrix representations of the 2-dimensional wave equations are:

$$(D_y^H D_y^E + D_x^H D_x^E + w^2 \varepsilon) E_z = 0 \qquad \text{(TM)} \qquad (23)$$

$$\left(D_y^E \varepsilon_x^{-1} D_y^H + D_x^E \varepsilon_y^{-1} D_x^H + w^2\right) H_z = 0 \qquad \text{(TE)} \qquad (24)$$

All subsequent simulations in this work have been performed by solving one of those two equations.

## j) Building an inverse-design solver

In order to build a software capable of using the algorithm described here to design electromagnetic devices, three main components are needed:

1) A data structure to define the problem: the design-space, the boundary conditions and constraints, the matrices involved in the optimization, the hyperparameters of the optimization, binarization…

2) An iterative optimization algorithm which implements the loop described in c) as well as the optimization enhancements

3) A forward simulation package (for us, based on FDFD) to evaluate the real performance of the device.

More details about our implementation of the inverse-design solver are shown in Appendix B.

# III) First theoretical demonstration: Inverse design of an ultra-compact broadband optical diode

Once the inverse-design algorithm has been implemented, it is very important to demonstrate whether it works or not. The fundamental questions to ask are:

1) Whether minimizing the residual field error will improve the performance of the device or not?

2) What kind of performance can we expect from inverse-designed devices, and how does it compare with other design methods?

3) What are the hyperparameters to tune and how to do it?

In this chapter, we use the example of the optical diode to answer those three questions and give some intuition about the practical use of inverse-design.

# PART I: Demonstration of the algorithm

## a) Motivations for the design of an optical diode

There has been a lot of interest recently for photonic devices that can achieve asymmetric light transmission or optical diode behavior[63-72]. Typically, **an optical diode is a two-port device where light coming from the first port is transmitted to the other port while light coming from the second port is not transmitted to the first port but either reflected, deflected or absorbed instead**. In particular, there is high interest for on-chip asymmetric light transmission devices for integrated photonic applications. An optical isolator is the ideal solution as it can transmit and block any spatial mode in the two directions. However, optical isolation is very challenging to be implemented in integrated devices[73]. This can only be achieved with large devices based on magneto-optic materials[74-77] or indirect interband transitions[78] usually not compatible with CMOS fabrication processes.

On the other hand, optical diode behavior can be achieved in a much simpler way with a reciprocal device based on **asymmetric mode conversion**[66]. Such a device relies on spatial symmetry breaking, which means that it can be done with any type of material. Reciprocal optical diodes can only achieve asymmetric transmission with specific modes[73]. Nonetheless, they typically need much smaller footprint than optical isolators, and some reciprocal diode designs are compatible with CMOS fabrication. Various types of reciprocal optical diodes have been demonstrated recently based on chiral metamaterials[79-83], hyperbolic metamaterials[84], digital metamaterials[71], metasurfaces[67], ring resonators[65], metal-silicon waveguides[85] and photonic crystals[63, 64, 68-70, 86]. Particularly, a very compact optical diode was proposed recently based on a photonic crystal structure made of silicon and air[66]. In the reported device,

the first even spatial mode from the left waveguide is converted into the first odd spatial mode by the optical diode structure and transmitted to the right waveguide, while the first even mode from the right is reflected back. However, the reported device only works with air waveguide and needs to be integrated into a larger photonic crystal medium, which increases the total footprint of the device (~ 2 × 4 square wavelength). Furthermore, the reported optical diode could only operate around a very small bandwidth, which is ~ 1% of the resonant wavelength.

In the next parts, we are going to show how our algorithm allows the design of an optical diode with lower footprint and a much larger bandwidth than the photonic crystal-based device. **The simulated diode is based on silicon, with air as medium, and integrated between two silicon waveguides.** Next, we show the choice of the objectives to design an optical diode, how the algorithm converges towards the final structure, and a parametric study to illustrate the choice of the model's hyperparameters. The performance of 3D devices based on our 2D simulations are also discussed as a function of the thickness.

## b) Optimization setup

Here we present the definition of the optical diode in the algorithm. The design-space is a 2-dimensional black-box representing a planar structure. On the boundaries of the design-space, which are 2 pixels-wide in our implementation, the permittivities and fields are well-defined. The design-space is surrounded by air ($\varepsilon = 1$), with two Silicon waveguides ($\varepsilon = 12$) on the left and right sides. The **H**-field on the bottom and top boundaries is null, and the field on the left and right boundaries depends on our definition of an optical diode. Here, we choose our optical diode to meet two objectives: first objective is to convert the first (even) mode incoming from the left waveguide to the second (odd) mode to the right waveguide, second objective is to reflect the first

mode from the right waveguide back, as shown in **Figure 3.1**. In the second case, the field on the left boundary is set to 0 to achieve zero transmission, and the field on the right boundary is a superposition of the first even mode of incident light and reflected light.

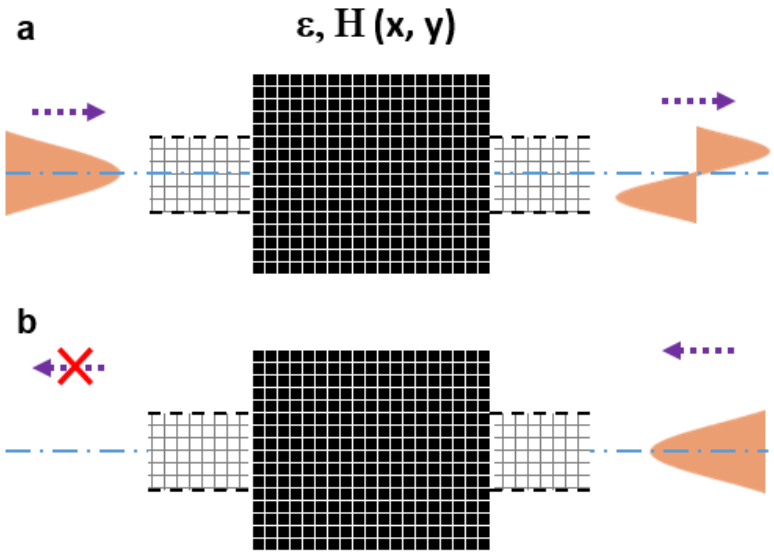


***Figure 3.1.*** *Schematic representation of the optical behavior for an optical diode. The first even mode is fully transmitted when it comes from the left port (a) and converted to the odd mode. Same input is reflected back when coming from the right port (b).*

Compared to a simple inverse design algorithm with one condition as described in previous chapter, we only modify the size of the field variable **H**, which become a N × 2 matrix instead of a N-vector, where N is the number of pixels in the device and 2 is the number of conditions. In general, and as explained in[87], this method can be used to assign any number k of objectives that one wants the device to achieve, with a computational cost proportional to k.

We focus on an optical diode which operates in Transverse Electric field (TE), which means the scalar vertical field is the magnetic field $H_z$. The permittivity values for the local medium are set to vary between $\varepsilon_{min}$ = 1 (air) and $\varepsilon_{max}$ = 12 (Silicon). For every iteration of the

algorithm, we perform two Finite-Difference Frequency Domain (FDFD) simulations to evaluate the performance of the device (the transmitted power) when the first even mode is incident from each side of the device.

The designs are evaluated according to four figures of merit. The physics residual R corresponds to the minimized value in Equations (4-7) chapter 2. The most important figure of merit is the transmission, which is the ratio of the output power to the input power and which is computed for both directions $T_{LR}$ (left to right) and $T_{RL}$ (right to left). Finally, the binary coefficient B, described in chapter 2, equation 16, allows us to monitor how close to binary our continuous structure is. We will verify that the closer B is to 1, the closer the performances of continuous and binary structures are. For every iteration, the figures of merit of both the structure with continuous $\varepsilon$ (the "continuous structure") and the binary structure are computed, the latter being the one that matters for a practical device and thus the one that we want to optimize.

## c) Design of the optical diode

First, we study the optimization process while designing an optical diode using the binarization algorithm described in chapter 2.e. The design space size is chosen to be $3/4\lambda \times 3/2\lambda$ where $\lambda$ is the wavelength, and the resolution is 40 pixels / $\lambda$ (30 × 60 pixels). The waveguide width is $0.4\lambda$ (16 pixels) and the initial permittivity in the device is uniformly equal to $8\varepsilon_0$.

The algorithm is run for 1000 iterations with the parameters given above. The evolution of the figures of merit is reported in **Figure 3.2** as a function of the iteration number. As expected, the physics residual field decreases (solid black curve in **Figure 3.2a**) along the optimization process. This results in the transmission efficiencies getting closer and closer to the ideal optical

diode values, with a final transmission ratio $R_{cont} = T_{LR}/T_{RL} = 92.6\% / 2.8\% = 33$ (30 dB). Thanks to the binarization cost, the continuous structure converges quickly towards a structure close to binary, as shown by the evolution of the binary value (**Figure 3.2b**) that converges towards 1. As a result, both the residual and the transmission efficiencies of the binary structure (dotted curves in **Figure 2a and 2c**) follow closely the values of the continuous structure, with a very similar final transmission ratio of $R_{bin} = 93.5\% / 3.2\% = 29$ (29 dB). The continuous and binary designs computed are represented by the color maps of **Figure 3.2d** and their respective figures of merit are shown in **Table 3.1**.

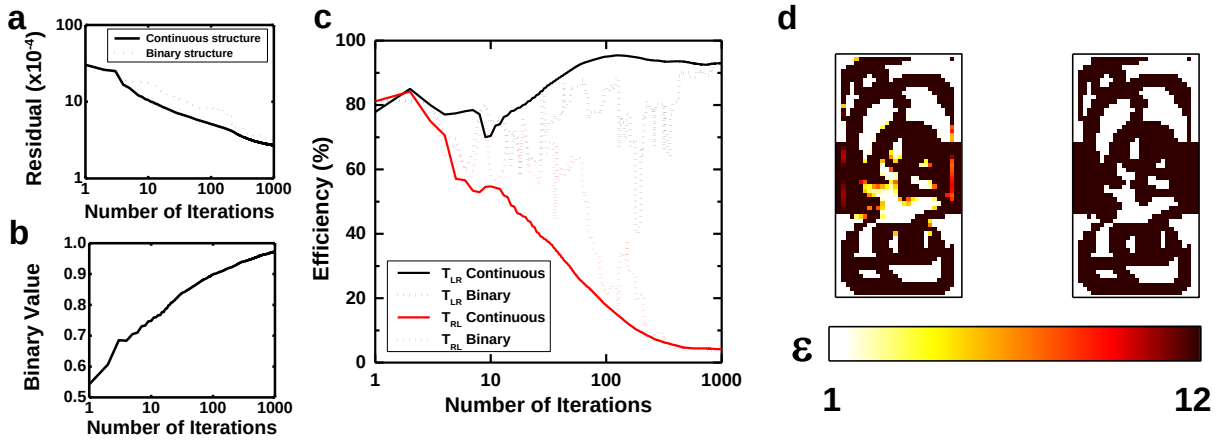


***Figure 3.2.*** *Physics residual (a), binary value (b) and transmission efficiencies for both direction incidences (c) of the designs computed by the objective-first inverse design algorithm as a function of the number of iterations. Figures of merit from the continuous and binary structures are respectively shown in solid and dotted lines.*
*(d) Color maps of the continuous (left) and binary (right) structures calculated by the inverse-design algorithms after 1000 iterations. Each structure is composed of 30 × 60 pixels, where the color shows the computed permittivity, between 1 (air) and 12 (Silicon).*

As discussed in previous part, the optimal binary structure achieves a performance very close to the ideal optical diode. Remarkably, this performance is achieved with a design area of only one square wavelength, which is one of the smallest optical diode reported to date, and in

particular 10 times smaller than the performance of the photonic crystal based optical diode reported in [66].

| Algorithm | Residual ($\times 10^{-4}$) | Binary | Transmission L → R | Transmission R → L |
|---|---|---|---|---|
| Continuous structure | 2.8 | 0.97 | 92.6 % | 2.8 % |
| Binary structure | 3.3 | 1 | 93.5 % | 3.2 % |
| Ideal value | 0 | 1 | 100 % | 0 % |

***Table 3.1****: Figures of merit of the 2 structures in Figure 2d.*

The structure of the optical diode and its operation are represented in the next figure. **Figure 3.3a** is a color map of the permittivity distribution, where black corresponds to silicon and white is air. **Figures 3.3b and 3.3c** are color maps of the real part of the magnetic field $H_z$ when the first even mode is incident from the left and right ports, respectively. In the case of left-to-right transmission, the even mode from the left is converted into an odd mode to the right as expected. This mode conversion is achieved by adding a $2\pi$ phase to the part of the field going through the lower part of the structure, as opposed to a $3\pi$ phase change for the part of the field going through the upper part. On the other hand, when the mode is sent from right to left, most of the power is deflected towards the top, then reflected back by the successive silicon-air layers that act similarly to a Bragg mirror.

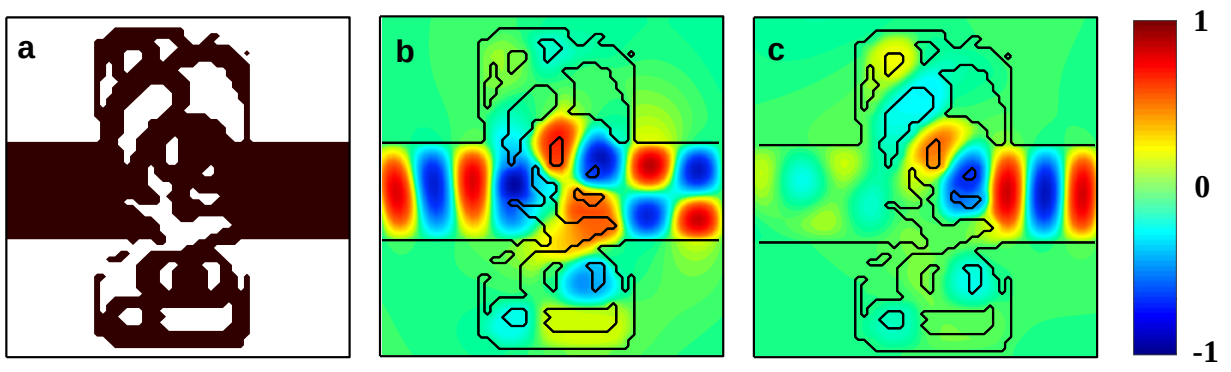


***Figure 3.3.*** *a) Color map of the optimal binary dielectric structure (4), black being Silicon and white is air. b) and c) are color maps of the real part of the magnetic field in the optical diode as calculated from FDTD simulations under excitation either from the left waveguide (b) or from the right waveguide (c).*

We use Lumerical, which is an Electromagnetics numerical solver, to perform finite-difference time-domain (FDTD) simulations of the proposed structure in order to verify the performance is as expected. The size of the structure is chosen so the operation wavelength is 1550 nm, but any resonant wavelength could be chosen by simply scaling up or down the structure. FDTD simulations are firstly performed in 2D settings, with a mesh size equal to half a pixel. The structure of **Figure 3.3a** is built out of silicon ($\varepsilon$ = 12), with air as the surrounding medium ($\varepsilon = 1$), and we use stretched coordinates PML boundary conditions. A pair of simulation are performed and compared: one using a source which is the first even mode incident from the left port with TE polarization and the other which is the same source but incident from the right port. The transmission as a function of the wavelength is plotted for both directions in **Figure 4a**. As can be seen, FDTD simulations (lines) agree very well with simulations from our FDFD code (spheres) at the resonant wavelength. Furthermore, we can see that the optical diode behavior is covering a broad wavelength spectrum. The left-to-right transmission stays higher than 80% and

the right-to-left transmission stays lower than 10% for wavelengths between 1.4 and 1.7 μm. This corresponds to a large relative spectral width $\Delta\lambda/\lambda = 20\%$ as opposed to the very narrow spectral width of a photonic crystal based optical diode of 1-2% only[66]. A ratio of up to 45 (33 dB) is observed between the two transmissions at resonant wavelength.

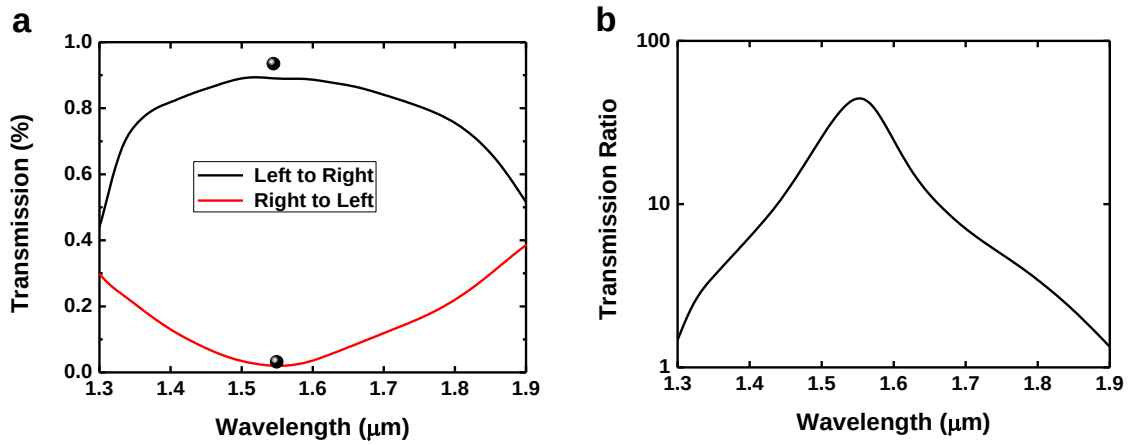


***Figure 3.4.*** *a) FDTD simulations of the optical power transmission in the optical diode as a function of the wavelength in both directions. The spheres represent the values calculated by our FDFD algorithm. b) Ratio between the two transmissions.*

# PART II: Hyperparameters tuning

The designs obtained with our algorithm are highly dependent on the simulation parameters such as the size of the black box, the initial conditions, the acceleration and binarization. Here we show a parametric study to understand the process of finding an optical diode with the best tradeoff between performance (transmission ratio), compactness, and manufacturability (thickness). Although the design part is exclusively done in 2D, we will also discuss about how well the performance can be reproduced with 3D designs.

Some parameters are kept unchanged in this part: the algorithm is run on a rectangular grid of pixels, defined by the pixel size chosen to be equal to $\lambda/40$ for this study, the length $L$ and width $W$ all expressed as a function of the wavelength $\lambda$ in the vacuum. The waveguiding ports width is chosen to be ~ $0.4\lambda$. Finally, the initial value of the permittivity $\varepsilon_{air} \leq \varepsilon_{init} \leq \varepsilon_{Si}$ is set to be uniform in the black box.

## a) Acceleration coefficient

As explained in chapter 2 g), the acceleration has been implemented to increase the speed of convergence and provide some "perturbation" to the algorithm to avoid some local minima. Here we test the convergence of the algorithm for various acceleration coefficients from 0 to 8. The optimization algorithm is run for 100 iterations. **Figure 3.5** shows the evolution of the physics residual as a function of the number of iterations, and **Table 3.2** shows the residual and transmission ratio after 100 iterations. Larger acceleration coefficients allow to converge faster, with lower residuals. However, for $\lambda_{acc} > 4$, oscillations of the residual appear, showing that the

acceleration is unstable. Therefore, we choose $\lambda_{acc}$ = 4 as the optimal value of the acceleration coefficients, which yields the best results in most designs, and the best ratio for this particular one.

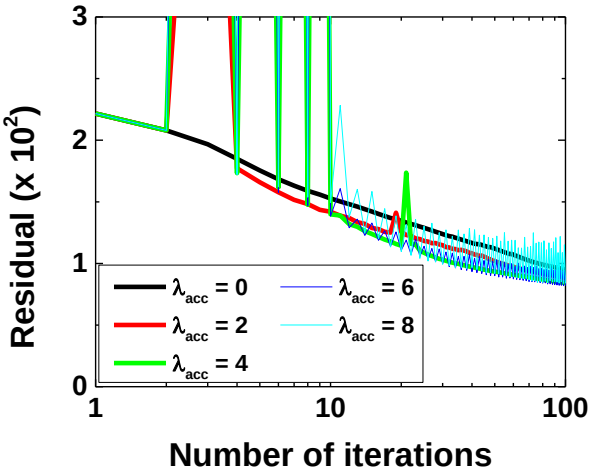


| Acceleration coefficient | Residual (x$10^3$) | Ratio $T_{L\to R}$ / $T_{R\to L}$ |
|---|---|---|
| 0 | 9.5 | 15 |
| 2 | 8.8 | 19 |
| 4 | 8.4 | 28 |
| 6 | 8.2 | 26 |
| 8 | 8.4 | 22 |

***Figure 3.5.*** *Evolution of the residual as a function of the number of iterations for optical diodes inverse-designed with acceleration coefficients from 0 to 8. $\lambda_{acc}$=0 shows the slowest convergence. $\lambda_{acc}$=8 shows fast decrease of the residual, but with large oscillations. $\lambda_{acc}$=4 shows the fastest convergence without significant oscillations.*

***Table 3.2****: Residual and ratio between the two transmissions after 100 iterations for various acceleration coefficients.*

## b) Binarization coefficient

In part I d), after 100 iterations a ratio of 28 is achieved for the optimized structure, but after conversion to a binary structure the ratio drops to less than 4, which is a very poor performance. This is because the optimized structure is far from binary, with a coefficient B = 0.848, and a lot of information is lost in the conversion. We use the binarization algorithm, described in chapter 2 e), to get a continuous structure very close to binary while keeping a good performance. The choice of the binarization hyperparameter is crucial: too low and the continuous

structure will not be close to binary, too high and the continuous structure will have low performance.

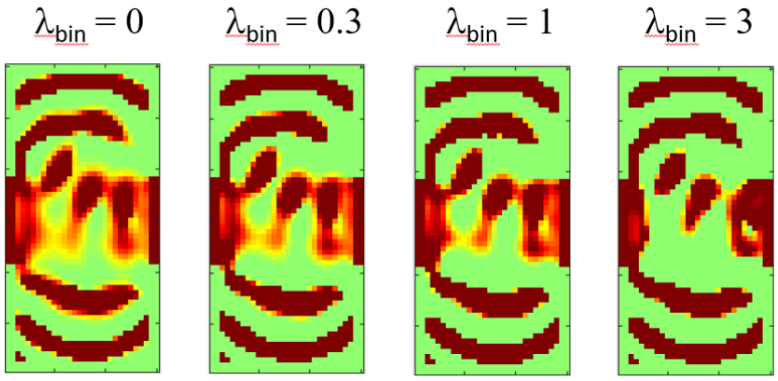


***Figure 3.6.*** *Structures obtained after 100 iterations of optimization followed by 100 iterations of binarization with various coefficients ($\lambda_{bin}$ = 0 is equivalent to optimization). The color scale varies from green ($\varepsilon$=1) to dark red ($\varepsilon$=12). The coefficients must be multiplied by $10^{-4}$ in practice.*

| Binarization coefficient (x$10^{-4}$) | Binary value | Ratio continuous | Ratio binary |
|---|---|---|---|
| 0 | 0.867 | 37 | 9 |
| 0.3 | 0.924 | 29 | 10 |
| 1 | 0.944 | 29 | 18 |
| 3 | 0.960 | 28 | 12 |

***Table 3.3****: Performance metrics of structures obtained after 100 + 100 iterations of optimization + binarization for various binarization coefficients.*

**Figure 3.6** shows the structure and **Table 3.3** shows the performance of a few optical diodes obtained after 100 iterations of optimization followed by 100 iterations of binarization for a few coefficients $0 < \lambda_{bin} < 3x10^{-4}$. The binary level of the continuous structure is shown, as well as the performance of both the continuous and the binary structures, in terms of ratio $T_{LR}$ / $T_{RL}$. As $\lambda_{bin}$ is larger and larger, the binary value becomes closer and closer to 1. On one hand, the

performance of the continuous structure decreases, as the algorithm focuses on competing objectives, minimizing both the physics residual and the binary coefficient. On the other hand, the performance of the binary structure gets better, as the difference between continuous and binary structures gets smaller. However, when the binary coefficient is too large, the binarization becomes a bit too abrupt, and the performance of the binary structure decays too. Empirically, we find a coefficient of $10^{-4}$ to be the best for a fast yet not too abrupt binarization. Keeping the binarization for a few hundred additional iterations allows to get performance of continuous and binary structure very close, as shown in part c.

## c) Design-space size and shape

Next, we study how the shape and size of the design space impact the device performance. For all the designs in this part, the initial permittivity is $\varepsilon_{init} = 4$. First, we study the impact of the design space aspect ratio on the performance while keeping the device area constant, approximately equal to $\lambda^2$. The three aspect ratio tested are W:L = 1:2, 1:1 and 2:1, for a number of pixels of 30×60, 40×40 and 60×30 respectively. The algorithm is run for each design space, and the binary devices' performances after optimization are summarized in **Table 3.4**. The structures and the magnetic field under excitation from the left waveguide are also shown in **Figure 3.7**. As can be seen, the performance of the long structure ($W:L$ = 1:2) is quite low, with a transmission ratio of only 6. From the field profile, we see that only the right part of the structure acts as an optical diode while the left part is mostly wasted space extending the left waveguide. On the other hand, the square and wide structures both show good transmission ratio. This indicates that the choice of the design space is critical for the algorithm to converge towards a good design. Here, the wide structure aspect ratio is preferred for the best optical diode performance.

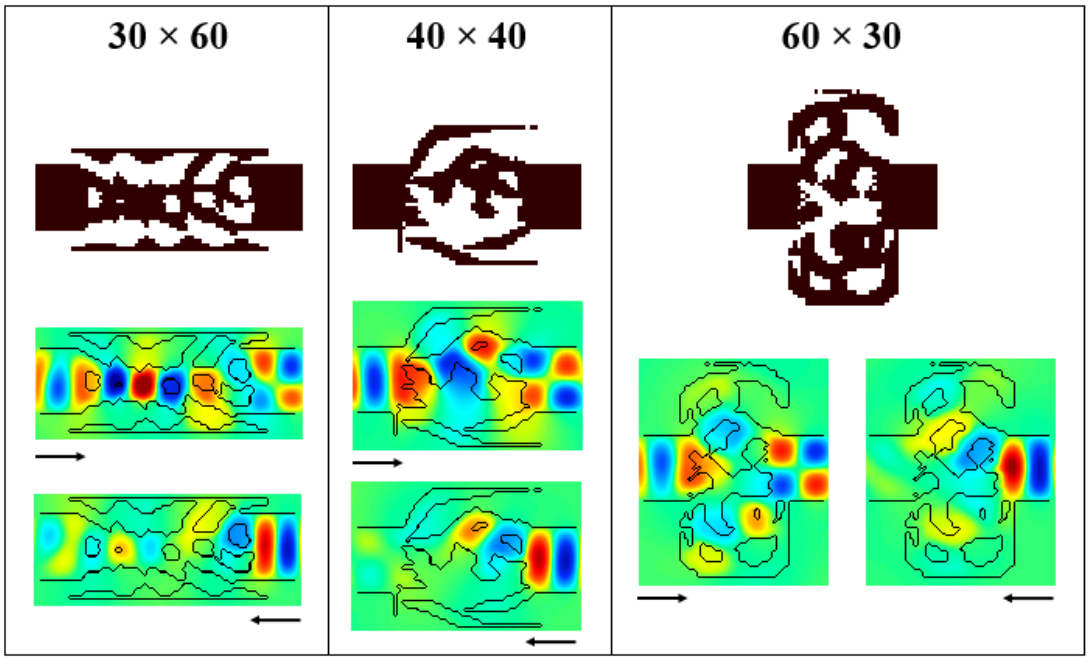


***Figure 3.7.*** *Color map of the dielectric structures (black and white) and the real part of the magnetic field (color) in the three optical diodes with aspect ratio 1:2 (left), 1:1 (middle) and 2:1 (right).*

| Structure Size (W×L) | $T_{L\to R}$ | $T_{R\to L}$ | Ratio |
|---|---|---|---|
| 30 × 60 | 64.1 | 10.4 | 6 |
| 40 × 40 | 85.8 | 4.1 | 21 |
| 60 × 30 | 90.2 | 3.4 | 27 |

***Table 3.4****: Performance (transmissions and ratio) of the binary structures in Figure 3.7.*

Next, we study the influence of the design space size for a fixed aspect ratio chosen to be W:L = 2:1 based on the previous optimization. Four device sizes are successively tested, with W×L = 20×40, 30×60, 40×80 and 60×120 respectively from the smallest to the largest design, with respective device areas of $\lambda^2/2$, $\lambda^2$, $2\lambda^2$ and $4\lambda^2$. The binary structures and fields are represented in **Figure 3.8** and the performance in **Table 3.5**. As expected, the performances of the first three

designs improve with the size as more and more degree of freedoms are available for the algorithm to converge towards better solutions. However, the performance does not improve anymore when the design space is too large (60×120), mainly because the binary conversion is less precise.

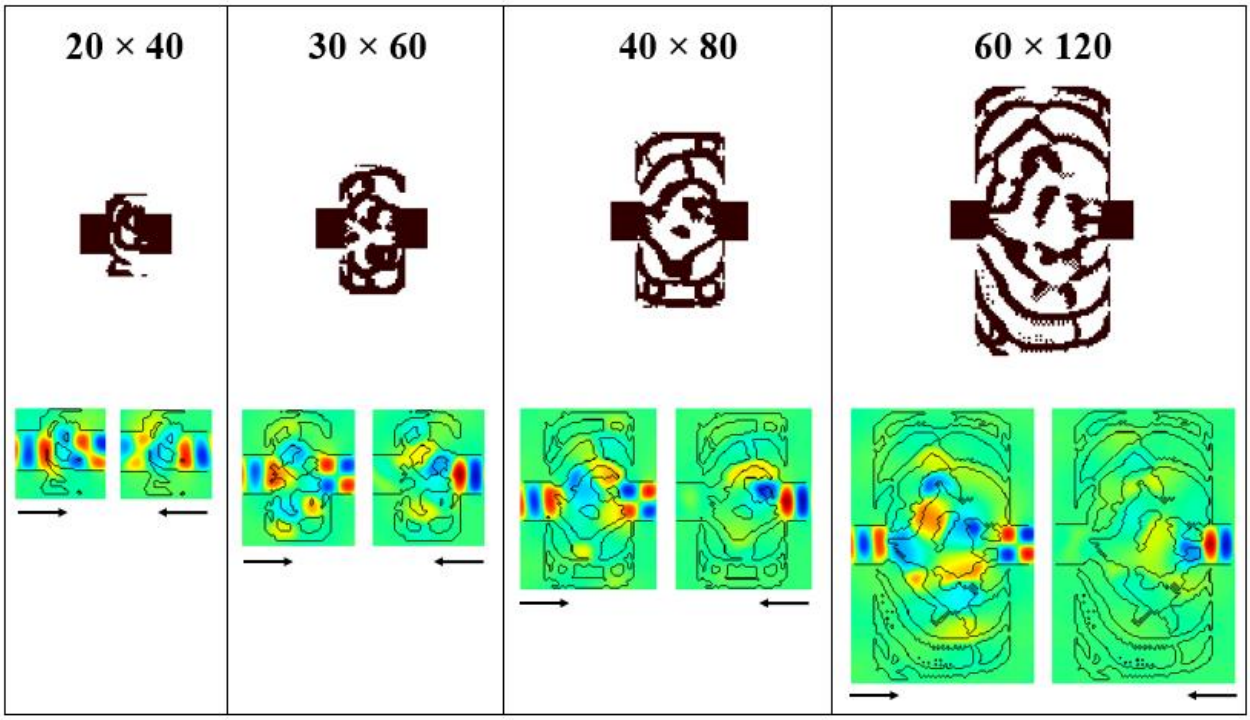


***Figure 3.8.*** *Color map of the dielectric structures (black and white) and the real part of the magnetic field (color) in the four optical diodes with, from left to right, size W×L = 20×40, 30×60, 40×80 and 60×120.*

For this study, we also report the performance of 3D structures based on the computed 2D designs but with a finite thickness equal to λ/4 and surrounded by air. As can be seen, the transmissions of the 3D designs are usually much lower than the 2D cases, especially in larger structures. This is mainly because in thin structures the field is not confined efficiently and "leaks" from the top and bottom of the structure, particularly in the air gaps of the silicon structure. The leakage is proportional to the total area of the gaps, which explains why the transmission is so low

in large structures. For this reason and although the 2D performance is not optimal, we prefer the smaller 30×60 structure that is expected to have better performance in a practical device.

| Structure Size (W×L) | 2D $T_{L\rightarrow R}$ | 2D $T_{R\rightarrow L}$ | 2D Ratio | 3D $T_{L\rightarrow R}$ | 3D $T_{R\rightarrow L}$ | 3D Ratio |
|---|---|---|---|---|---|---|
| 20 × 40 | 81.8 | 37.3 | 2.2 | 75 | 30 | 2.5 |
| 30 × 60 | 90.2 | 3.4 | 27 | 57 | 1.8 | 32 |
| 40 × 80 | 95.6 | 0.6 | 159 | 37 | 0.9 | 41 |
| 60 × 120 | 93.6 | 1.0 | 94 | 17 | 0.18 | 94 |

***Table 3.5****: Performance (transmissions and ratio) of the binary structures in Figure 3.8.*

## d) Initial permittivity

Now that the design space size has been optimized, we study the impact of the initial conditions on the design, specifically the initial permittivity that is used at the first iteration of the algorithm. For this study, the device size is W × L = 3/4 λ × 3/2 λ (30 × 60 pixels). The binarization algorithm is run for initial integer permittivities between 1 and 12. Here we report the optimized structures for $\varepsilon_{init}$ = 1, 4, 8 and 12 respectively. The binary structures and fields are represented in **Figure 3.9** and the performance of both the 2D and 3D structures with thickness equal to λ/4 are shown in **Table 3.6**.

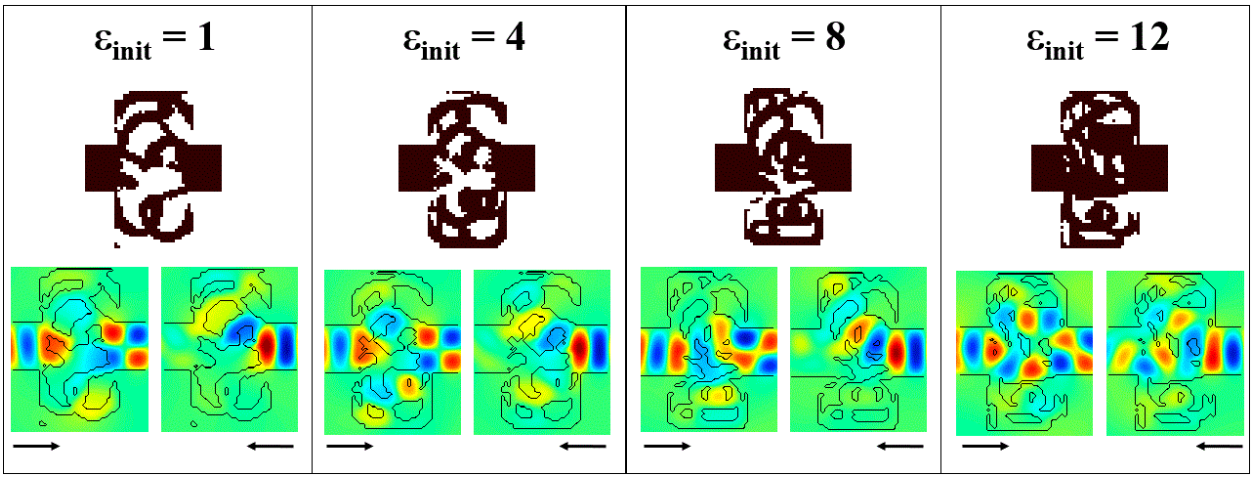


***Figure 3.9.*** *Color map of the dielectric structures (black and white) and the real part of the magnetic field (color) in the four optical diodes computed starting from an initial permittivity $\varepsilon_{init}$=1, 4, 8 and 12 from left to right.*

| Initial permittivity | 2D $T_{L\to R}$ | 2D $T_{R\to L}$ | 2D Ratio | 3D $T_{L\to R}$ | 3D $T_{R\to L}$ | 3D Ratio |
|---|---|---|---|---|---|---|
| 1 | 90.3 | 4.1 | 22 | 52 | 2.2 | 24 |
| 4 | 90.2 | 3.4 | 26 | 57 | 1.8 | 32 |
| 8 | 93.5 | 3.2 | 29 | 78 | 2.6 | 30 |
| 12 | 83.5 | 27.1 | 3.1 | 72 | 21 | 3.4 |

***Table 3.6****: Performance (transmissions and ratio) of the binary structures in Figure 3.9.*

First of all, we notice that the algorithm converges towards very different structures depending on the initial condition. Depending on the initial permittivity, the final structure will be composed of air for the most part if $\varepsilon_{init}$ is small and of silicon for the most part when $\varepsilon_{init}$ is large. From the perspective of the field, the optical diode behavior can be achieved in many ways. One way to understand intuitively the difference between these structures is by visually finding the phase change along the shortest optical path between the left and right waveguides. In the case of

left to right transmission, the smallest phase change is $\pi$ when $\varepsilon_{init} = 1$ or 4, $2\pi$ when $\varepsilon_{init} = 8$ and $3\pi$ when $\varepsilon_{init} = 12$. As for the performance, we can see that the first three designs have very similar transmissions in 2D although the structures differ drastically. Nonetheless, the performances of the 3D structures are very different and seem to favor structures with more silicon, as the third structure has a much better transmission from left to right. The reason is that the field is better confined vertically in structures with a high silicon content, which prevents scattering of optical power from the bottom and top of the structure. However, too much silicon content does not allow an efficient optical diode behavior as well. Empirical observation shows that the best 3D performance is achieved with $\varepsilon_{init} \approx 7\text{-}8\ \varepsilon_0$.

## e) Device thickness

So far we studied the performance of 2D structures, which is equivalent to considering infinitely thick structures in 3D, and also the performance of $\lambda_0/4$-thick devices surrounded by air, where $\lambda_0$ is the target resonant wavelength. These results are extended here to the case of a more realistic structure with finite thickness etched through a silicon-on-insulator (SOI) wafer. The structure is assumed to be etched through the entire upper silicon layer, until the insulator material which is assumed to be silicon dioxide for the calculations. The performance of 3D devices based on the design from **Figure 3.3** are studied as a function of the thickness. The transmission in both directions are shown in **Figure 3.10a and 3.10b** for device thicknesses of $\lambda_0$, $\lambda_0/2$, $\lambda_0/4$ and $\lambda_0/8$ as well as for an infinitely thick device (2D). **Figure 3.10c** is a color map representing the transmission ratio as a function of the wavelength and the device thickness both expressed as a function of $\lambda_0$. As can be seen, the thinner the 3D device, the higher the difference with the 2D

case. In particular, the resonant wavelength λ is blue-shifted when the device thickness t decreases, following the empirical law:

$$\lambda = \frac{\lambda_0}{\sqrt{1+\left(\frac{\lambda_0}{2nt}\right)^2}} \quad (1)$$

where *n* is an empirical coefficient equal to 6 for the case of this device. This empirical law is represented by the black line in **Figure 3.10c**. Although the transmission ratio and bandwidth decrease with the thickness, very good optical diode performance can be achieved for devices as thin as $\lambda_0/6$, with a transmission ratio higher than 10 over a large bandwidth $\Delta\lambda/\lambda \approx 13\%$. Such an optical diode optimized for telecom wavelengths (around 1550nm) would yield a device with an area of approximately $3\mu m^2$ and a thickness of 250nm, which corresponds to most common SOI wafers commercially available and should be easy to fabricate with current silicon processes.

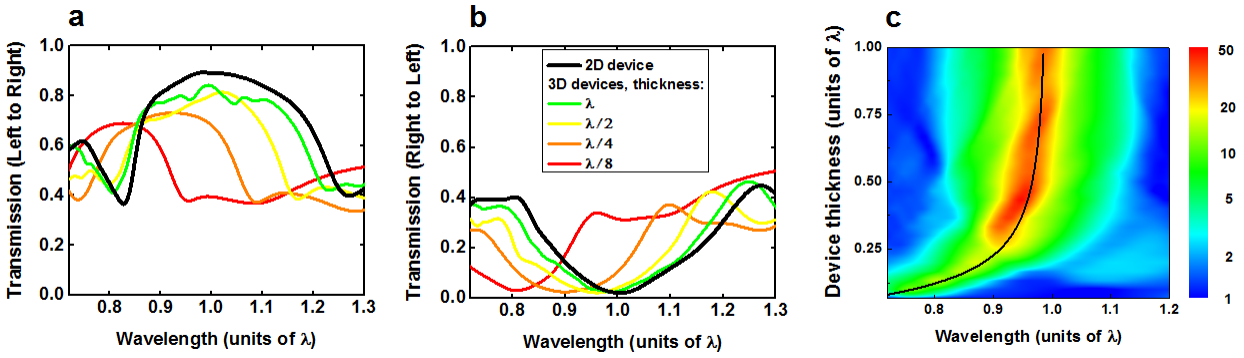


***Figure 3.10.*** *FDTD simulations of the optical power transmissions (a and b) and ratio (c) in a 3D optical diode etched in a SOI wafer as a function of the wavelength and for various device thicknesses.*

# Conclusion

In this chapter we have shown that our algorithm works as hoped: **minimizing the physics residual results in improved performance**. An efficient ultra-compact optical diode based on silicon and air only has been designed. The device operates by converting the first even mode from the left port into the first odd mode of the right port, while the first even mode from the right port is reflected back by the structure. Only a few minutes of computing time are needed in order to converge towards a high-performance design, which means one can test the influence of various parameters very fast. A parametric study was designed in order to understand and optimize the impact of various hyperparameters on the final designs. We found that although a large design space allows convergence towards very high-performance structures in 2D, smaller designs behave better in practical 3D devices due to the lower scattering, and devices with higher silicon content are preferred for the same reason. Optimized design shows a broadband optical diode behavior around the resonant wavelength, with a peak transmission ratio of 30 between excitations from the left and right sides. Compared to previous silicon-air optical diodes devices, mostly based on photonic crystals, this design has a smaller footprint of 1 square wavelength and a broader wavelength spectrum.

# IV) Inverse design and 3D-printing of polymer meta-devices for free-space manipulation

In the previous part, we demonstrated the convergence and efficiency of the algorithm on a Silicon-based optical diode. However, this type of device requires very expensive fabrication methods, as the only known examples have been fabricated with electron-beam lithography. Furthermore, Silicon-based devices are good to manipulate light on-chip, but not very well-suited for free-space applications, apart from metasurfaces, because only planar devices can be fabricated with reasonable complexity. In this chapter, we want to **extend the range of inverse-design applications, by using 3D-printing to access new types of architectures that can be practically fabricated**. Compared to the previous chapter, there are two main differences:

_ For free-space manipulation, the input and output signals are very different than waveguide modes. Here we use plane-waves with various angles and wavelengths, and cylindrical waves for focusing.

_ Most 3D-printing methods use polymer materials, which have a much lower index ($n \approx 1.5$, $\varepsilon \approx 2.3$) than Silicon. We need to show that inverse-design algorithm can design efficient low-index devices.

# PART I: 3D-printed meta-devices for millimeter-wave manipulation

First, we propose a platform combining inverse-design with additive manufacturing to design and fabricate all-dielectric meta-devices[88]. As opposed to conventional flat metasurface-based devices that are composed of resonant building blocks resulting in narrow band operation, the proposed design approach creates non-resonant, broadband ($\Delta\lambda/\lambda$ up to >50%) meta-devices based on low-index dielectric materials. High-efficiency (transmission > 60%), thin ($\leq 2\lambda$) meta-devices capable of polarization splitting, beam bending, and focusing are shown in this part. Experimental demonstrations are performed at millimeter-wave frequencies using 3D-printed devices.

## a) Motivations

Conventional optical elements that control the polarization, phase and amplitude of electromagnetic (EM) radiation such as lenses, polarizers, beamsplitters, and mirrors are typically engineered at a scale much larger than the wavelength. Within the last two decades, significant amount of research has been devoted to understand light-matter interactions and design novel materials and electromagnetic devices with subwavelength features. Metamaterials, and more generally materials composed of nanostructures with subwavelength feature size, have emerged as a viable platform to manipulate electromagnetic radiation in unconventional manners [7, 11, 12, 29-31, 83, 89]. In particular, photonic crystals[6, 90, 91] and negative-index materials[92] have been used to achieve sub-diffraction lensing[93-95]. More recently, metasurfaces [8, 9, 50, 72, 96-102] have gained substantial interest due to their ability to perform optical functionalities such as lensing[98, 103], holograms[100, 104] and beam shaping[105] within an extremely thin layer. Although the ability to control phase, amplitude and polarization using subwavelength-thick

metasurfaces is a promising route towards building miniature optical devices, they suffer from several drawbacks prohibiting their potential in replacing conventional bulk optical elements. Initial metasurface designs utilized plasmonic metals that exhibit high optical losses and thus were of relatively low efficiency[101]. Lossy metals have been replaced with high-index dielectric materials like amorphous silicon [106], but such metasurfaces often rely on Mie-type resonances that result in a narrow wavelength range of operation[105, 107].

Typical metasurface design starts with identification of an optical resonator with a well-defined geometrical shape, such as triangles[99], rectangles[104, 108], ellipses[105] or V-antennas[96, 101]. Phase information is then calculated for various geometrical parameters such as radius, width, orientation, etc.[106]. The number of degrees of freedom in the design of these shapes is very limited, which makes it difficult to optimize both efficiency and bandwidth of meta-devices while achieving full control of the polarization. Here, our inverse-design method, combined with additive manufacturing, allows to design high-efficiency (>60%), broadband ($\Delta\lambda/\lambda$ > 25%), dielectric-based thin ($\leq 2\lambda$) electromagnetic meta-devices overcoming the aforementioned limitations. Next, we demonstrate the design, fabrication and characterization of wavelength-scale meta-devices for bending, polarization splitting and focusing of EM radiation at millimeter-wave frequencies.

## b) Design of meta-devices

First, we design two meta-gratings to behave as polarization beamsplitters for normally incident free-space radiation. As illustrated in **Figure 4.1A**, those devices bend parallel and perpendicular polarizations to opposite diffraction orders. We also design a meta-grating that bends both polarizations to the same diffraction order (**Figure 4.1B**). Finally, we propose a ~$\lambda$-

thick flat meta-lens (**Figure 4.1C**) that converts a normally incident plane-wave into a focusing cylindrical wave.

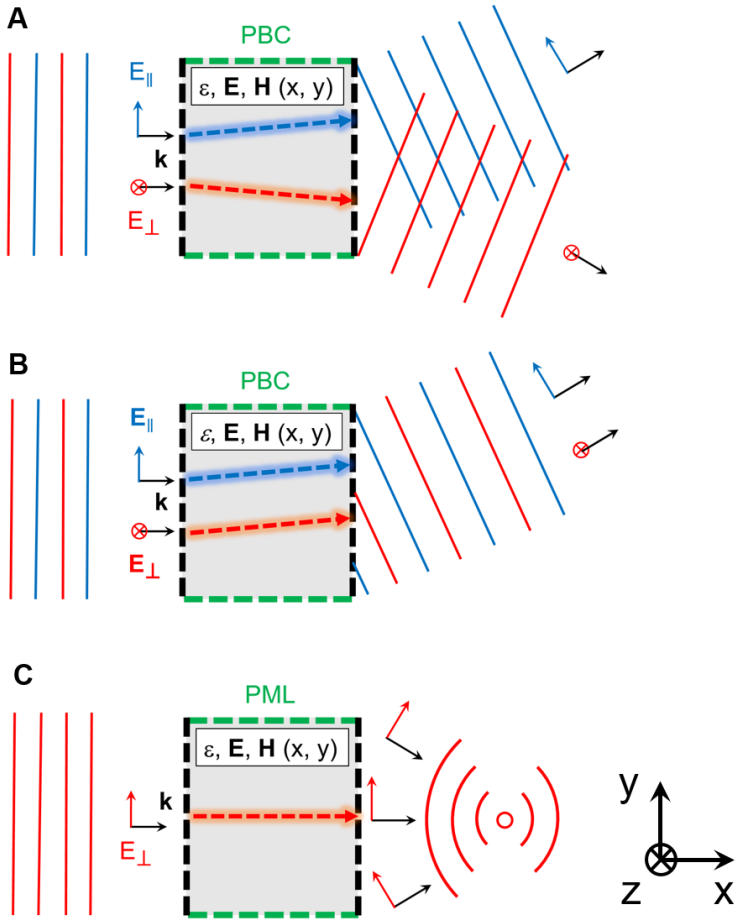


***Figure 4.1.*** *Schematics for the inverse electromagnetic approach for designing free-space meta-devices. The desired optical functionality is defined by a set of input and output conditions at the boundaries of the design space. A polarization splitter (A) is a grating that converts normally incident plane waves of parallel and perpendicular polarizations into two different diffraction orders. A bending device (B) converts a normally incident plane wave into the same diffraction order. A flat meta-lens (C) is a device that converts a plane wave into a cylindrical wave converging to a chosen focal point.*

Bending and polarization splitting are achieved using meta-gratings that convert an input plane wave to an output plane wave with a different diffraction order than m = 0, with periodic

boundary conditions along the *x*-axis. For meta-lenses, we aim to focus an input plane wave at a desired focal distance; hence, the output is chosen to be an hyperbolic phase profile[109] such that:

$$\phi(y)=\frac{2\pi}{\lambda}f\left[\sqrt{1+\left(\frac{y}{f}\right)^2}-1\right]\ (\text{modulo } 2\pi) \tag{1}$$

where f is the focal distance and y is the distance from the axis of the lens. Meta-lenses do not perform like a grating; therefore, we set the boundary conditions of a perfectly matched layer (PML) along the *x* direction. The designs are two-dimensional, which corresponds to meta-devices with infinite height along *z*. In practice, the fabricated devices are $\approx 10\lambda$ thick.

## c) Fabrication and measurement

Inverse-designed meta-devices are fabricated using additive manufacturing, commonly called 3D-printing. This bottom-up approach allows the fabrication of very complex devices with a large aspect ratio. Furthermore, 3D-printing is an incredibly scalable method, with resolutions ranging from 100 nm to 1 mm [110-112], allowing the fabrication of electromagnetic devices for applications from the visible to the millimeter- wave and microwave regimes [113-116]. Here, we demonstrate the proposed devices in the millimeter-wave regime (f > 30GHz) using high impact polystyrene (HIPS)[117] and a consumer grade 3D-printer based on fused deposition modeling for the fabrication. The material is chosen for its low cost and very low attenuation in the microwave to millimeter-wave region, with a loss-tangent measured to be $\tan\delta < 0.003$ over the 26-38 GHz band. In this band, the real part of the dielectric constant of HIPS $\varepsilon' \approx 2.3$ ($n \approx 1.52$), which is then used as a constraint in our algorithm to design binary devices made of air ($\varepsilon = 1$) and HIPS ($\varepsilon = 2.3$). Because of the low index, the phase difference between the input and output is approximately

proportional to the effective thickness of the polymer. Therefore, in order to allow a $2\pi$ phase shift between a part full of polymer and a part full of air, the device thickness needs to obey:

$$\Delta\phi = 2\pi(n-1)\frac{t}{\lambda} = 2\pi \times 0.52 \times \frac{t}{\lambda} \geq 2\pi \quad (2)$$

which means that the minimum device thickness is around $2\lambda$.

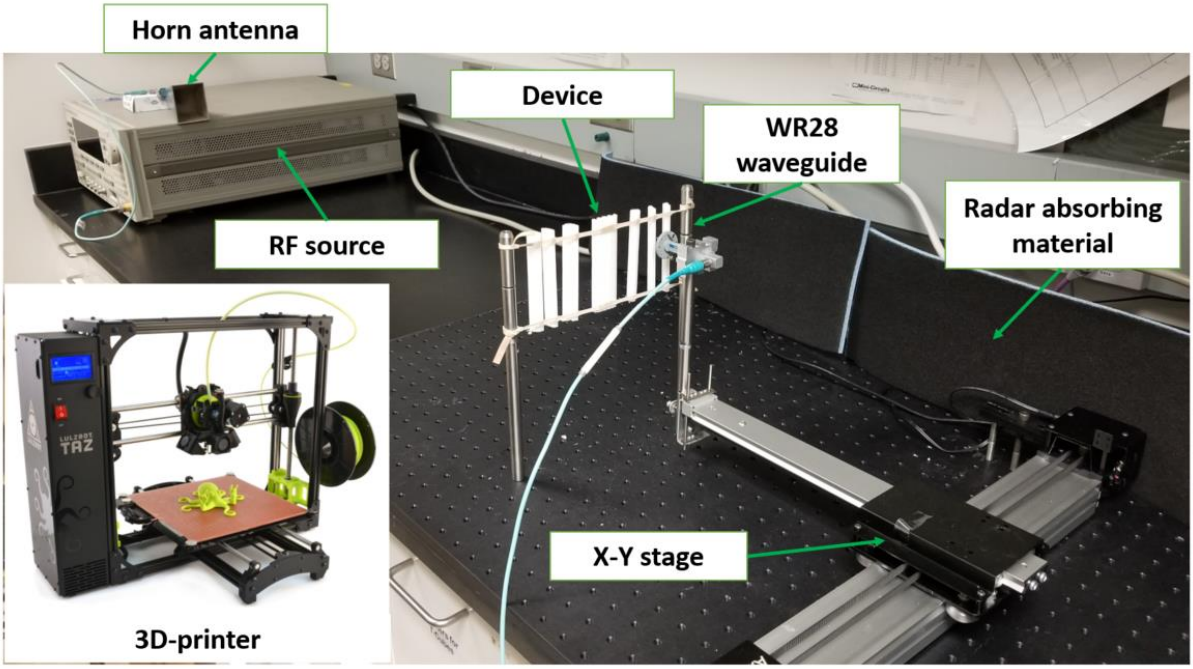


***Figure 4.2:*** *Photograph of the experimental setup used to test the millimeter wave properties of the stretchable lens. Signal is generated by a RF source and transmitted by a high gain Horn antenna as an approximate plane-wave. After the device, the electromagnetic power in the axial plane is collected by a WR-28 waveguide whose position is controlled by an automated X-Y stage, then analyzed by a parametric analyzer. In the bottom-left, picture of the 3D-printer used to fabricate the polystyrene meta-lens.*

To test the electromagnetic properties of the devices, a vector network analyzer (VNA) generates the input signal that is transmitted through a high-gain horn antenna placed far away from the sample (distance > $100\lambda$) in order to produce a plane wave perpendicularly incident on

the input surface. The device is surrounded by radar absorbing material to prevent reflections from the surroundings. For the three meta-gratings, the transmitted power is measured in the far-field (>100λ) with a low-gain horn antenna as a function of the angle between -40° and 40° in 2° steps and as a function of the frequency between 26 GHz (11.5 mm) and 38 GHz (7.9 mm). For the lenses, the output power is mapped along the axial plane on the right side of the device using a probe antenna attached to a X-Y stage. The measurement starts around 1cm to the right of the device due to technical limitations of the setup, which is the reason why the experimental intensity maps are truncated when compared to the simulated maps. Photographs of the 3D-printer and the measurement setup are shown in **Figure 4.2**.

## d) Meta-gratings

First, we demonstrate a free-space polarization splitter. The proposed meta-device (**Figure 4.3A**) deflects a normal incident plane-wave polarized along y (parallel) and z (perpendicular) directions into m=+1 and m=-1 diffraction orders respectively with high efficiency and over a broad bandwidth. The width is chosen to be ~2λ to reach desired phase change as explained in the experimental section. The periodicity, L along y is determined by the deflection angle θ of the desired diffraction order m (here m = ± 1 for all devices), following the grating equation $L \sin\theta = m\lambda$ . We designed and optimized the meta-device for an operation frequency of 33 GHz (free space wavelength of λ=9.1 mm) and a deflection angle of θ = ± 30°, for which L = 1.8 cm. The inverse-design algorithm generates a binary refractive-index distribution of dielectric and air that is then printed with dimensions of 2 cm x 7.2 cm x 8 cm. A photograph of the 3D-printed meta-device is shown next to the computer-generated pattern in Figure 4.3A, which shows the high fidelity of the 3D-printing method.

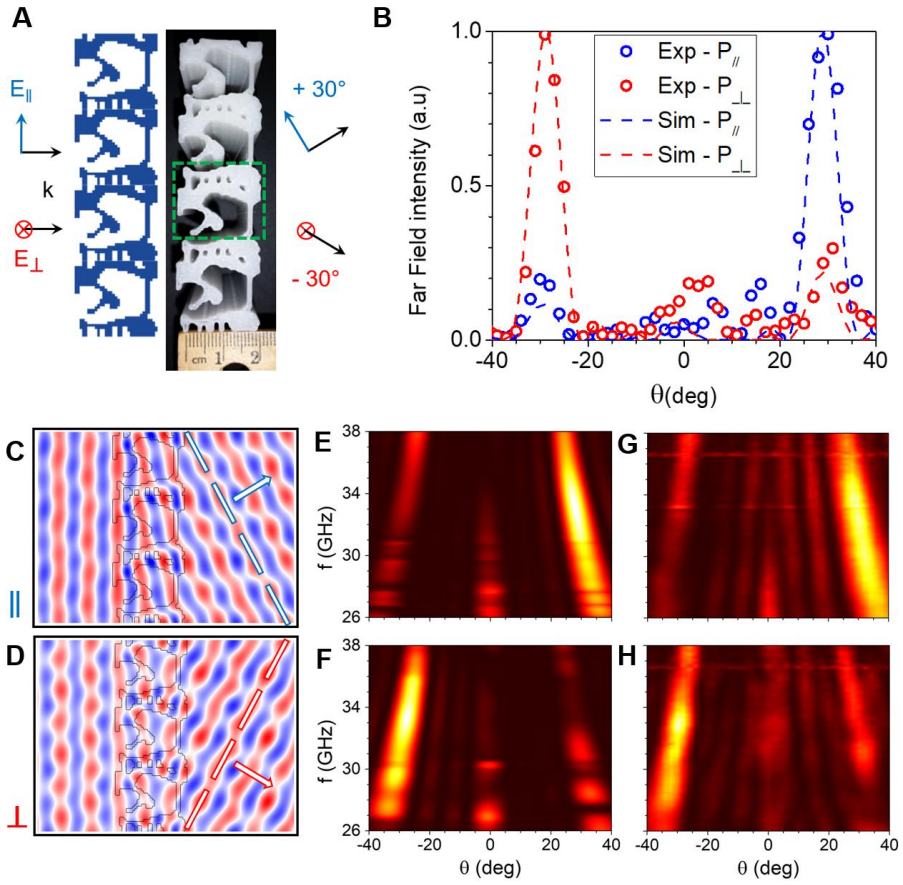


***Figure 4.3.*** *Inverse-designed polarization splitter. (A): Schematic drawing (left) and top-view photograph (right) of the 3D-printed 30° polarization splitter. The green rectangle indicates the unit cell of the grating. B) Simulated (dashed lines) and measured (circles) far-field power as a function of deflection angle for both parallel and perpendicular polarizations. (C) and (D): Simulated* $\boldsymbol{H}_z$ *and* $\boldsymbol{E}_z$ *field amplitudes for parallel (C) and perpendicular (D) polarizations, respectively, at 33 GHz. (E) to (H) Simulated (E, F) and measured (G, H) far-field intensity profiles as a function of the output angle and the millimeter-wave frequency for parallel (E, G) and perpendicular (F, H) polarizations.*

We measured the far-field angular transmission through the fabricated meta-device to verify the predicted polarization splitting behavior. **Figure 4.3B** plots the simulated and measured power distributions at 33 GHz. We observe that a plane wave with parallel polarization is bent at an angle $\theta = +30°$, whereas the perpendicular polarization is deflected with an angle of $\theta = -30°$.

The total power transmitted by the meta-device at 33 GHz is measured to be 76% for the parallel polarization and 54% for the perpendicular polarization, which are lower than the simulated values of 90%. The discrepancy is likely due to structure imperfections in the fabricated devices, the finite number of periods in the printed structures as well as an imperfect plane-wave input. The rejection ratio, defined as the ratio between the peak intensity and the maximum intensity outside the main peak, is experimentally found to be 5.2 dB and 7.0 dB for the parallel and perpendicular polarizations, respectively, which are close to the simulated values of 6.6 dB and 9.3 dB, respectively.

We perform full-field electromagnetic simulations to calculate the electromagnetic properties of the meta-device. We plot the vertical fields, i.e. $\mathbf{H}_z$ for parallel polarization (**Figure 4.3C**) and $\mathbf{E}_z$ for perpendicular polarization (**Figure 4.3D**), at 33 GHz. The spatial field distribution provides a clear picture of how the EM waves propagate inside the meta-device. In metasurfaces based on resonant geometric elements, the phase change is due to the interaction of the incoming plane-wave to a strong Mie resonance mode[105], which typically results in a relatively narrowband operation. Here, the phase change does not stem from the interaction with a specific resonant mode, but rather due to light propagation inside the dielectric structure, with a larger phase shift of $6\pi$ in a part filled with dielectric ($\varepsilon = 2.3$) than a $4\pi$ shift in a part mostly void ($\varepsilon = 1.0$). The polarization splitting is a result of the different phase-change response of the device to different polarizations owing to its complex dielectric shape.

Although we choose 33 GHz to be the frequency to optimize for highest efficiency in our inverse-design algorithm, we observe broad operation bandwidth that spans a range of frequencies from 27 to 38GHz, for a relative bandwidth $\Delta\lambda/\lambda \approx 33\%$, which is enabled by the inverse-design

method favoring non-resonant dielectric structures. **Figure 4.3** plots simulated (**E,F**) and measured (**G,H**) power transmitted in the far-field as a function of the angle and the frequency for parallel (**E,G**) and perpendicular (**F,H**) polarizations. The simulations and measurements agree relatively well.

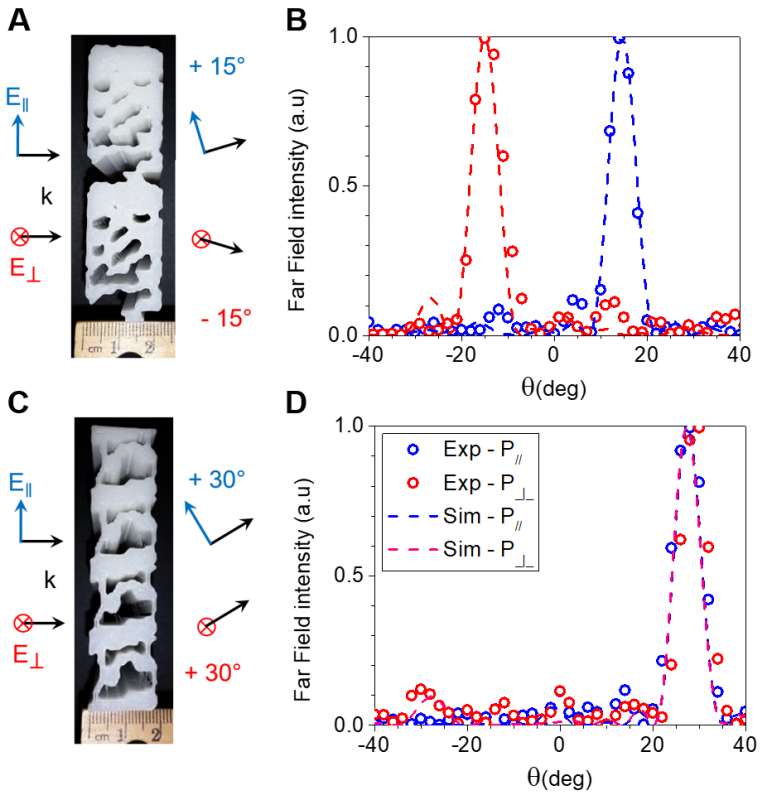


***Figure 4.4.*** *Inverse-designed meta-gratings. Photographs (A, and C) and simulated (dashed lines) and experimental (circles) far-field intensity plots of the 15° polarization splitter (B) and the 30° bending device (D) as a function of the output angle for a frequency of 33 GHz.*

In order to demonstrate the versatility and flexibility of the inverse-design approach, we designed and fabricated two additional meta-devices that bend the millimeter-waves. The first one is a polarization splitter with a bending angle of +/-15° (**Figure 4.4A**). Similar to the 30° splitter, this device presents a gradient of dielectric filling fraction along the *y*-direction with a larger

periodicity (L = 3.5 cm) in order to favor a smaller bending angle. The simulated and measured angular far-field transmitted powers are plotted for both polarizations at 33 GHz in **Figure 4.4B**. The measured rejection ratios for the 15° splitter are 8.2 dB and 10.6 dB for parallel and perpendicular polarizations respectively. The device has a dielectric filling fraction with a similar profile to that of a bending device towards the +15° diffraction order. The polarization splitting is due to the coupling of perpendicular polarization to a resonant wave propagating along the *y*-direction inside the device, which reverses the bending direction. This explains the lower bandwidth of the device for perpendicular polarization, from 31 to 37GHz (a relative bandwidth of 18%), compared to a very large bandwidth for the bending behavior of parallel polarization, from 22 to 44GHz (data not shown). The designs, simulated fields and broadband far-field data are shown in **Figure 4.5**.

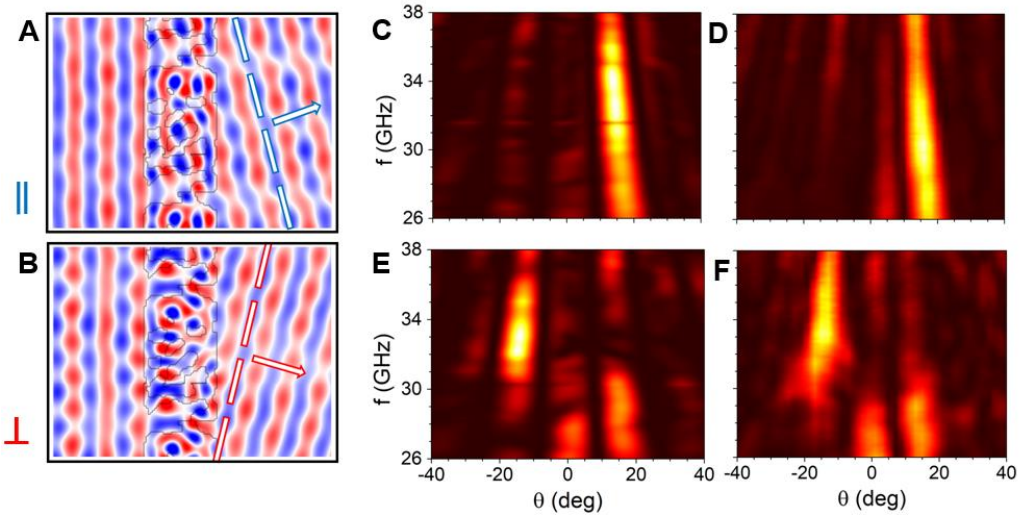


***Figure 4.5.*** *15° polarization splitter. Simulated $H_z$ (A) and $E_z$ (B) fields in the 15° polarization splitter with a perpendicularly incoming plane wave for parallel (A) and perpendicular (B) polarizations and at a frequency of 33GHz. Simulated (C, E) and experimental (D, F) far-field intensity color maps as a function of the output angle between -40° and 40° and as a function of the frequency between 26GHz and 38GHz for both parallel (C, D) and perpendicular (E, F) polarizations.*

In addition to polarization beam-splitter, we also designed and realized a polarization-independent bending device which bends both polarizations to the same diffraction order. Simulations and experimental results of the far-field power at 33 GHz are shown in **Figure 4.4D**, showing very good agreement between the theory and experiment. The designs, simulated fields and broadband far-field data are shown in **Figure 4.6**.

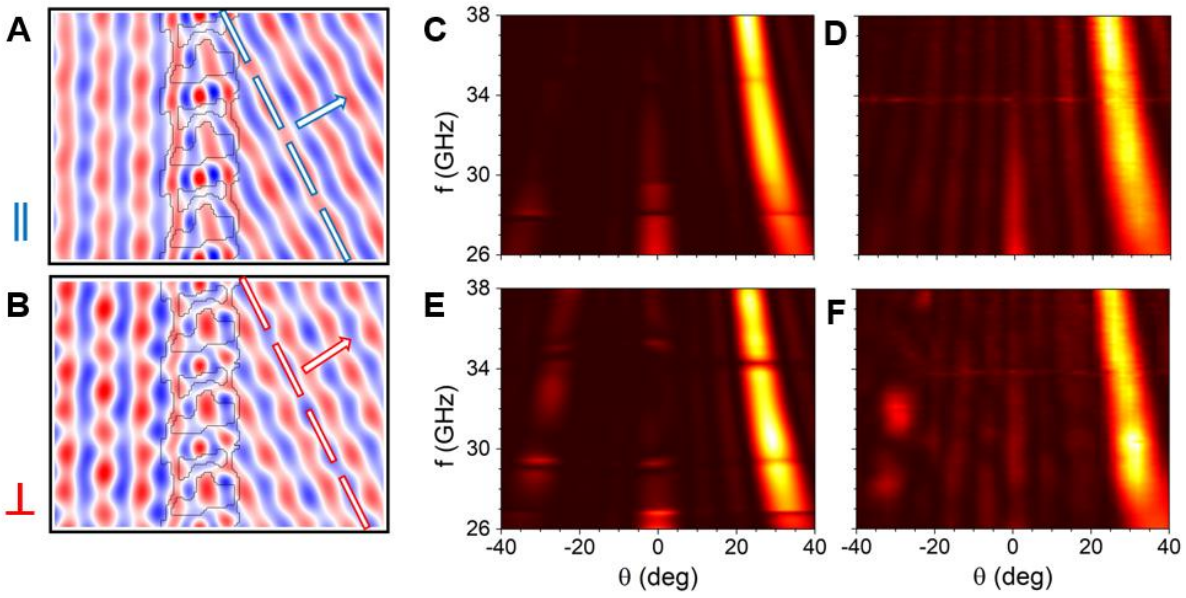


***Figure 4.6.*** *30° bend. Simulated $H_z$ (A) and $E_z$ (B) fields in the 30° bending device with a perpendicularly incoming plane wave for parallel (A) and perpendicular (B) polarizations and at a frequency of 33GHz. Simulated (C, E) and experimental (D, F) far-field intensity color maps as a function of the output angle between -40° and 40° and as a function of the frequency between 26GHz and 38GHz for both parallel (C, D) and perpendicular (E, F) polarizations.*

Although polarization-independent bending of EM radiation can be achieved with a triangular blazed grating (**Figure 4.7D**), such gratings deflect significant amount of power to higher diffraction orders, as shown in **Figure 4.7E and F**. On average from 26 to 38 GHz, the inverse-designed device reduces the amount of power sent into undesired diffraction orders by a

factor of 2.8 for parallel polarization and 2.0 for perpendicular polarization when compared to a blazed grating of similar thickness, which can be seen on the far-field power in **Figure 4.7B and C**. The bending to the first diffraction order extends to 44GHz with high efficiency (data not shown), which corresponds to a relative bandwidth of 55%, but significant power is diffracted to higher orders for larger frequencies.

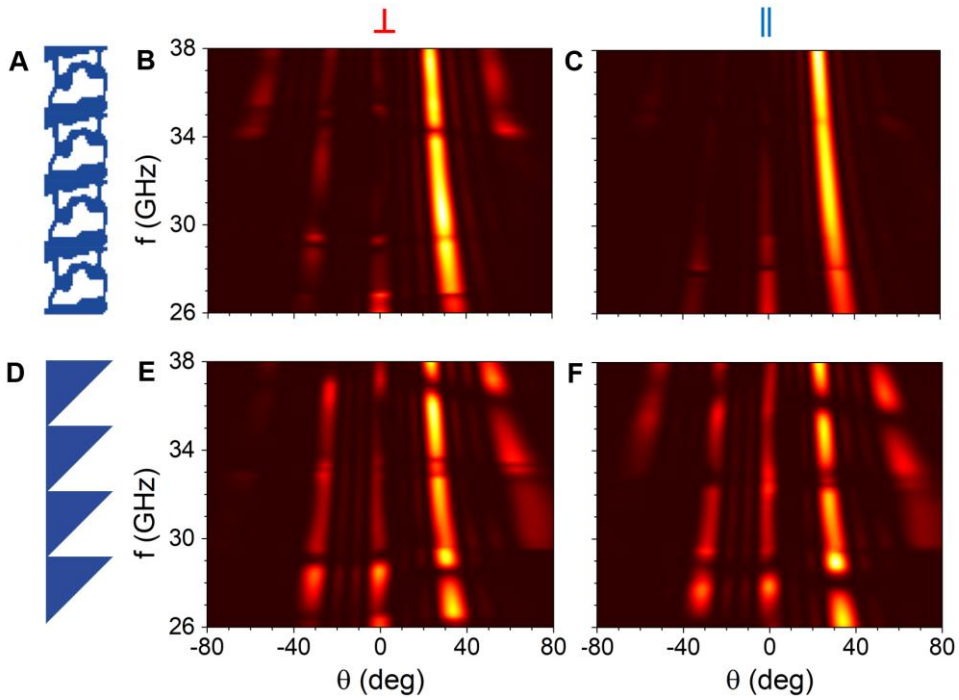


***Figure 4.7.*** *Comparison between the performance of the inverse-designed device (A to C) and a blazed grating (D to F) optimized to bend electromagnetic radiation by 30° independently of the polarization. The simulated far-field intensities are represented for angles from -80° to 80° and for frequencies from 26GHz to 38GHz for perpendicular (B, E) and parallel (C, F) polarizations. As can be seen, the inverse-designed meta-device transmits a much lower power to undesired grating orders (23% for perpendicular polarization and 18% for parallel polarization) than the blazed grating (47% for perpendicular polarization and 51% for parallel polarization). Simulated rejection ratios at 33GHz are 10.1 dB and 12.4 dB for the inverse-designed bending device, compared to 6.6 dB and 3.8 dB for the triangular grating for perpendicular and parallel polarizations respectively.*

## e) Meta-lenses

Next, we propose and design flat meta-lenses using the inverse-design algorithm and boundary conditions as illustrated in **Figure 4.1C**. We designed and fabricated two different meta-lenses with focal lengths of 2λ and 15λ, respectively. Both lenses are optimized and scaled for operation around 38 GHz (λ = 7.9 mm). The first meta-lens is 1.5-cm wide, 10-cm long, the second is 2.5-cm wide and 15-cm long and both are 10-cm tall. A picture of each device is shown with the computer-generated design in **Figure 4.8**.

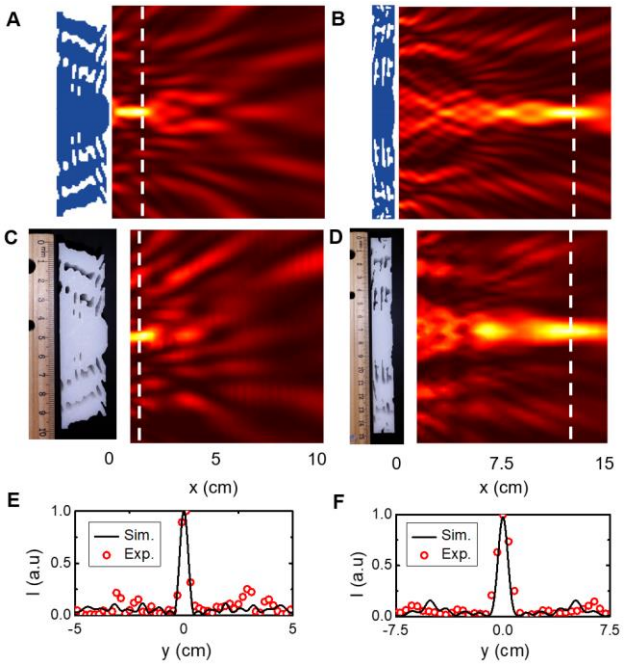


***Figure 4.8.*** *Inverse-designed meta-lenses. Simulated (A, B) and measured (C, D) spatial power distributions along the x-y plane at the output of the meta-lenses at 38 GHz. The input plane wave is generated by a horn antenna 1 m away on the left of the device while the output is measured with a probe antenna scanned along a 9x10 cm x-y plane for the first lens (A, C) and a 14 x 15 cm plane for the second lens (B, D). The first lens focuses perpendicularly polarized EM field 2λ away from the device whereas the second lens focuses it 15λ away. Schematics and pictures of the 3D-printed lenses are shown next to the simulated and experimental maps respectively. (E) and (F): Cross-section of the simulated (black line) and measured (red circles) power along the white dashed lines on the color maps for the first (E) and second (F) lens.*

The electromagnetic behavior of both devices is simulated with a perpendicularly-polarized incoming plane wave. The electric-field intensity profiles for the short-range and long-range meta-lenses are plotted in **Figure 4.8A and B**, respectively. We also performed a 2D scan of the transmitted power behind the meta-lenses using a millimeter-wave probe antenna positioned at z = 5cm. The measured spatial intensity distribution in the x-y plane for the short-range and long-range lenses are provided in **Figure 4.8C and D**, respectively. The simulated and measured spatial-intensity distributions closely match. As expected, the first device focuses EM radiation 1.5 cm (~2λ) away from the device whereas the second device's focal point is located 12 cm (~15λ) away. The full-width-at-half-maximum (FWHM) of the focused radiation for both devices are 0.5 cm and 1.1 cm as shown in **Figure 4.8E and F**, respectively, corresponding to practical numerical apertures (NAs) of 0.8 and 0.36 respectively, close to the theoretical values of 0.82 and 0.53, respectively. The proposed devices also show broadband focusing behavior from 28 GHz to 40 GHz. We provide the measured and simulated intensity profiles for operation at 30 GHz in **Figure 4.9**.

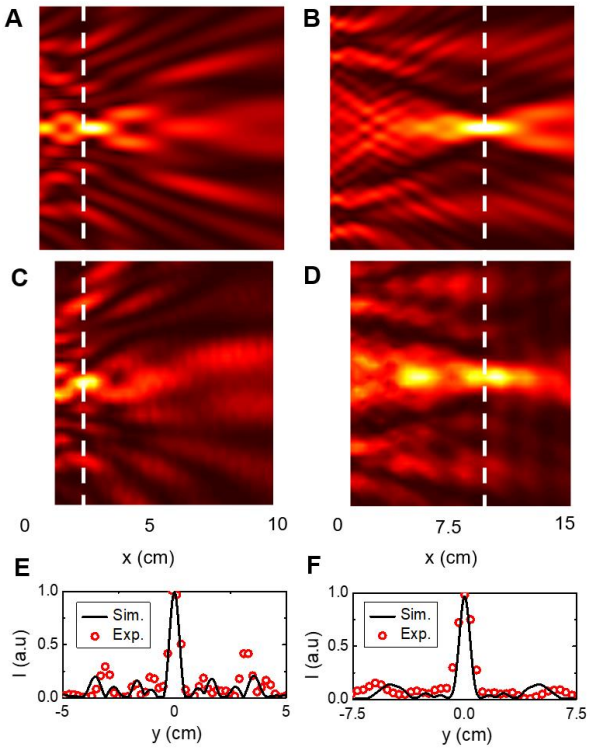


***Figure 4.9.*** *Inverse-designed meta-lenses at 30GHz. Simulated (A, B) and experimental (C, D) electromagnetic intensity color maps along the x-y plane at the output of the devices at a frequency of 30 GHz for the first (A, C) and second (B, D) lenses. (E) and (F): Cross-section of the simulated (black line) and measured (red circles) power along the white dashed lines on the color maps for both lenses.*

# PART II: Leveraging inverse-design to make a stretchable meta-lens

In the previous part, we showed that inverse-design can be used to design high-performance thin meta-gratings and meta-lenses based on 3D-printed polymers. Here, we want to demonstrate that inverse-design can help **make efficient tunable devices**. We demonstrate an inverse-designed all-dielectric, flat and stretchable, polymer-based meta-lens[118]. Focal distance tunability is an intrinsic property of stretchable diffractive meta-lenses[119]. However, meta-lenses designed in Part I e) are not stretchable. In this work, the key to achieve a high degree of stretchability is to carefully choose the initial point of the algorithm to get a design made of separate blocks that can be brought closer or further from each other. The lens is then fabricated by 3D-printing[110] and tested in the millimeter-wave regime, showing high tunability and superior performance when compared to a Fresnel lens.

## a) Design and fabrication

**Figure 4.10(a)** illustrates the boundary conditions and interior constraints used to the design the polymer lens. Here, the device is optimized to operate for a TE polarized incoming plane wave. The focal length is chosen to be $7.5\lambda$ at the optimized wavelength without stretching. Once the boundary conditions are set, the degrees of freedom of the inverse-design algorithm are the range of permittivities allowed and the size and initial conditions of the design space. The range of relative permittivities is defined by the materials used for the fabrication, here air, $\varepsilon = 1$ and high impact polystyrene (HIPS), $\varepsilon = 2.3$.

In order to generate the hyperbolic output phase profile in Equation 1, the design space must be large enough to allow phase change variations of up to $2\pi$ between a part full of air and a

part full of polymer. Heuristically, this condition is achieved with a lens thickness as low as 1.5λ, approximately, which is the thickness that we choose for the optimization. Finally, we set the initial condition of the optimization routine to a uniform permittivity level $\varepsilon_{init}$. This parameter has a considerable influence on the optimized design structure and performance[87]. Depending on its value, the final device will be either mostly made of polymer (when $\varepsilon_{init} = 2.3$) or made of sparse blocks (when $\varepsilon_{init} = 1$), as illustrated in **Figure 4.10(b)**, where we show three structures obtained via inverse-design optimization with initial permittivities of 2.3, 1.65, and 1.0 respectively. With seven individual blocks and a polymer content of only 30% of the design-space area, the third device is ideal to build a stretchable lens. This device can be either compressed by a factor down to s = 0.7, or stretched by any factor s > 1, as illustrated in **Figure 4.11**, where structures compressed by a factor of 0.8, 1.0, and 1.4 are shown.

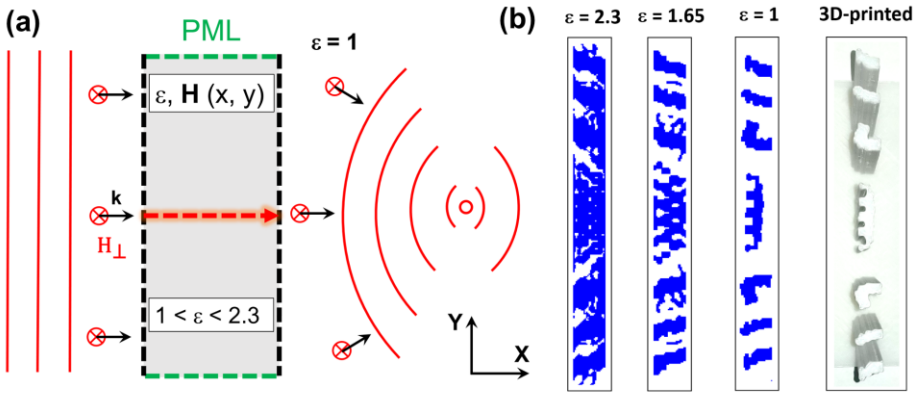


***Figure 4.10:*** *(a) Schematic representation of the inverse design of a lens. A TE-polarized input plane-wave perpendicularly incident to the left of the design space undergoes a transformation in the device to become an output cylindrical wave focusing at a desired focal distance. The algorithm optimizes both the permittivity and the perpendicular magnetic field inside the design space. PML = perfectly matched layer. (b) The left three images show structures optimized by the design algorithm starting from initial uniform permittivities of ε = 2.3, 1.65, and 1.0, respectively. The final image is a photograph of the 3D-printed HIPS lens from the ε = 1 simulation.*

## b) Experiment

The device was printed with a commercial 3D-printer, and a picture is shown in **Figure 4.11(b)**. The device's X×Y dimensions are 1.5×15λ, which corresponds to 1.25×12.5 cm for an operating wavelength of 8.3mm (36GHz). For such a 2D lens, the height is simulated as infinite, and in practice the device is 10cm-thick (12λ), which takes around 10 hours to print. After printing, we connect all seven blocks with each other at the top and bottom with two rubber bands, which act like a stretchable platform. When the rubber bands are quiescent, the device has a stretch factor of s = 0.8, for a length of 10cm. The device can then be stretched by a factor up to s = 1.5. We test the device's response to normally-incident electromagnetic radiation by using a radiofrequency source to generate a millimeter-wave beam through a high-gain horn antenna which directs the radiation perpendicularly towards the device. The device is placed 1m away from the antenna so that the beam is approximately a plane wave, and the output power is mapped along a plane on the other side of the device using a WR-28 waveguide (3.5×7mm) attached to a X-Y stage. A picture of the setup is shown in **Figure 4.2**. The measurement starts around 1cm to the right of the device due to technical limitations of the setup. We measured the output power for stretching factors of s = 0.8, 1.0, 1.2, and 1.4, which corresponds to lengths of 10cm, 12.5cm, 15cm, and 17.5cm, respectively. We also simulated the electromagnetic behavior of the device with full-field FDTD simulations. In **Figure 4.11**, we show the map of the power profile along the axial plane at 36GHz from simulations (left) and experiments (right) for stretching factors of 0.8 (top), 1.0 (middle), and 1.4 (bottom). As can be seen, there is a remarkable agreement between the simulations and the experiment, showing that the device behaves as a tunable lens as expected.

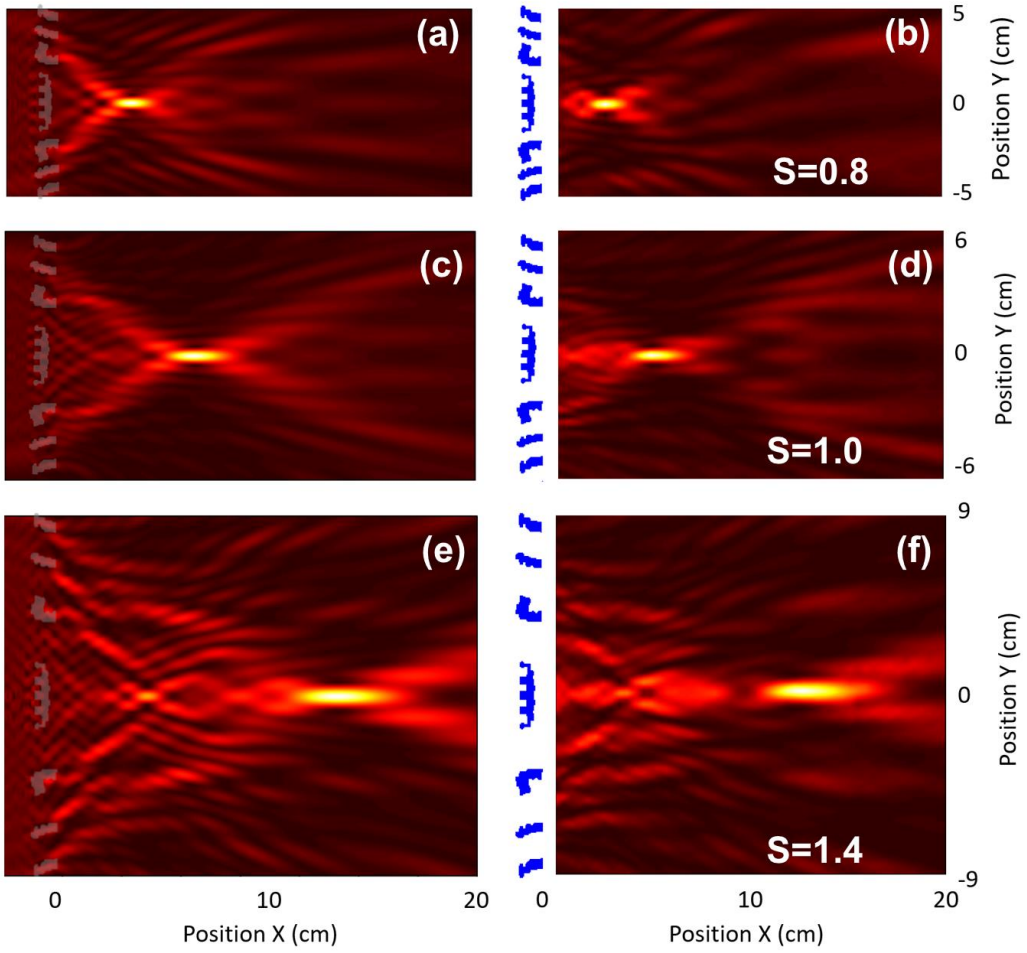


***Figure 4.11:*** *Simulated (left) and experimental (right) optical power profiles along the axial plane of the device for stretching factors of s = 0.8 (a and b), 1.0 (c and d), and 1.4 (e and f).*

We report the focal distance in **Figure 4.12(a)** for all stretching factors and for frequencies from 30GHz (λ = 10mm) to 40GHz (λ = 7.5mm). The focal distance can be fitted with the following heuristic law:

$$f \approx \left(\frac{\lambda_0}{\lambda}\right)^{\frac{3}{2}} \left(s^2 f_0 + s(s-1)\frac{L}{6}\right), \qquad (2)$$

where f is the focal distance, $f_0$ is the focal distance at optimal wavelength $\lambda_0$ and at stretching factor s = 1, and L is the lens length when s = 1. The first term in the parenthesis comes from the paraxial approximation, which is represented by the dashed line in **Figure 4.12(a)**, and the second term is a correction due to the high numerical aperture of the lens, which has magnitude comparable to the focal distance. Experimentally, we observe that the focal distance is tuned from 4.5cm to 17cm for a stretching factor from 0.8 to 1.4, which is tuning of a factor of 3.8 for a relative stretching factor of 1.75.

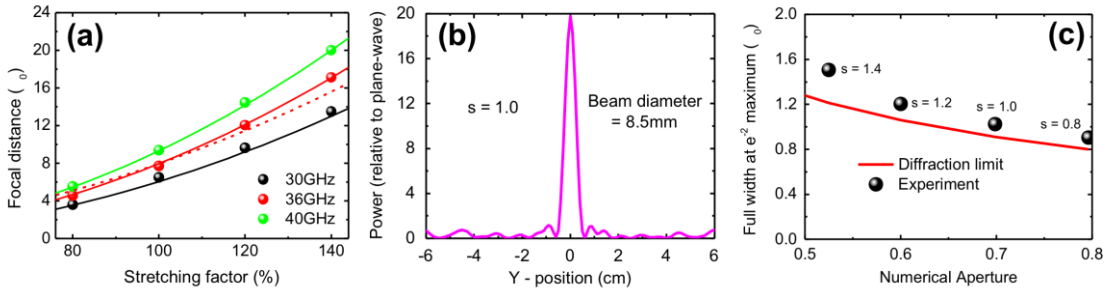


***Figure 4.12:*** *(a) Experimental (spheres) and theoretical (solid lines) focal distance as a function of the stretching factor and the frequency, expressed as a factor of the optimal wavelength $\lambda_0$. The dashed line represents the theoretical distance in the paraxial approximation. (b) Experimental power profile in the focal plane of the device for a stretching factor s = 1.0 and a frequency of 36GHz ($\lambda_0$ = 8.3mm). The power is normalized to the power of the plane-wave reaching the device. (c) Measured and diffraction-limited beam spot size in the focal plane as a function of the numerical aperture of the lens, which increases with lower stretching factors.*

In **Figure 4.12(b)**, the measured power profile is plotted in the focal plane of the device for s = 1.0 and at 36GHz, normalized by the power of the incident plane wave. The power at the focal point is 17 times higher than the power in any other point of the focal plane. The beam diameter, defined as the full width at $e^{-2}$ ($\approx 0.135$) maximum is 8.5mm, which is very close to the diffraction-limited value of D = 7.6mm. The beam diameter is reported in **Figure 4.12(c)** as a

function of the numerical aperture for all four experimental stretching factors and compared to the diffraction limit, given by:

$$D = \frac{2\lambda}{\pi\, NA}, \tag{3}$$

where NA is the numerical aperture, equal to 0.7 for a stretching factor s = 1.0, and which follows:

$$NA = \left[1 + \left(\frac{f(s)}{sR}\right)^2\right]^{-\frac{1}{2}} \quad . \tag{4}$$

The lowest NA corresponds to the highest stretching factor (s = 1.4) and the highest NA to s = 0.8. As can be seen, the stretchable lens is very close to being diffraction limited for 0.8 < s < 1.2, and the experimental beam diameter for s = 1.4 is still only 24% higher than the diffraction-limited value.

## c) Comparison with a Fresnel lens

A Fresnel lens with the same refractive index, matching size, focal distance, and operating wavelength is shown in **Figure 4.13(a)** and compared to the inverse-designed device. Both devices rely on diffraction and can be viewed as first-order gratings with periodicity that decreases farther from the center. However, the inverse-designed device has the advantage of using only 44% as much material as the Fresnel lens, and it can be uniformly compressed by a factor as low as s = 0.7 for better tunability, which is not possible with the Fresnel lens. We simulated the focusing efficiencies of both devices at the optimal wavelength and for stretching factors from 0.7 to 1.5 (1.0 to 1.5 for the Fresnel lens) and plotted them in **Figure 4.13(b)** (dashed lines) to compare their performance. Focusing efficiency is defined here as the ratio of the power that passes through an aperture in the focal plane with a size of the beam diameter as defined earlier, over the total power going through the focal plane. As can be seen, both devices have similar performance ≈ 75% at

low stretching factors, but the inverse-designed device has better efficiency for larger stretching factors, with efficiency > 60% for 0.7 < s < 1.4, compared to only 1.0 < s < 1.2 for the Fresnel lens. Experimental focusing efficiency of the inverse-designed device matches closely with the simulated efficiency and remains within 63% and 72% over the entire range of stretching factors.

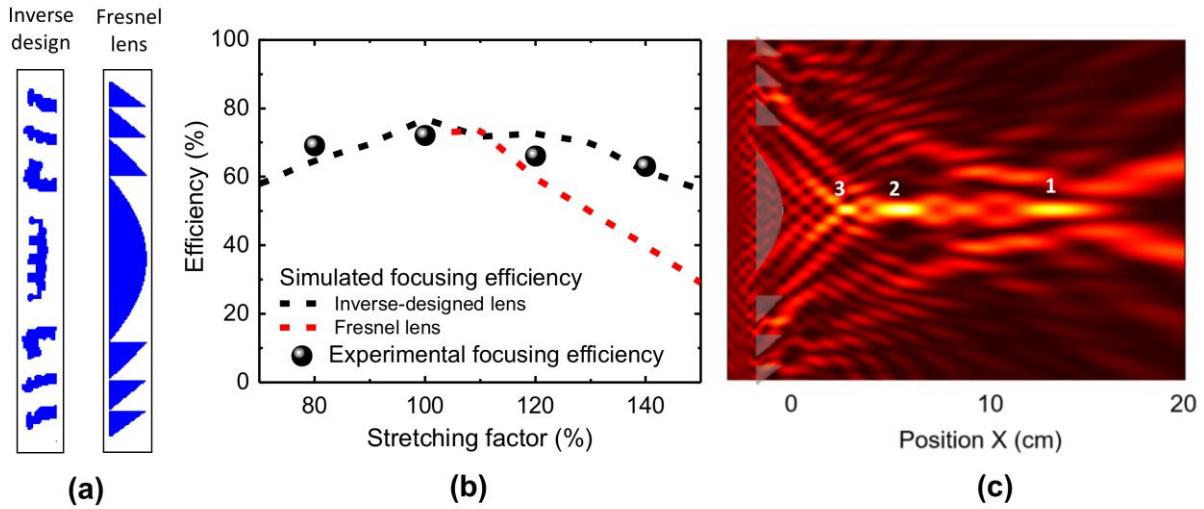


***Figure 4.13:*** *(a) Comparison between a Fresnel lens and the inverse-designed device, showing that the latter uses only 44% as much material. (b) Experimental (spheres) and simulated (black dashed line) focusing efficiency of the inverse-designed device and the Fresnel lens (red dashed line) as a function of the stretching factor. Focusing efficiency is defined as the ratio of the power going through the center peak divided by the power transmitted through the focal plane. (c) Simulated optical power profile along the axial plane of the Fresnel lens stretched by a factor s = 1.4. There are three main focal points corresponding to the 1st, 2nd and 3rd diffraction orders of the lens.*

Furthermore, the simulated absolute focusing efficiency is 64% for the inverse-designed lens at s=1.0, and it remains > 45% for 0.7 < s < 1.4. On the other hand, the absolute focusing efficiency of the Fresnel lens is 55% at s = 1.0 and drops to 23% at s = 1.4. The lower efficiency of the Fresnel lens for large stretching factors can be explained by two observations. First is that the large central block remains unchanged under stretching, so it will keep focusing on the same

point. Second is that the stretching opens gaps between blocks that are initially connected, which is a much greater perturbation of the overall geometry than for the inverse-designed device where stretching just increases the gap between the blocks. This results in a large power focused into focal points from higher diffraction orders, as illustrated by the optical power profile of the stretched Fresnel lens (s = 1.4), shown in **Figure 4.13(c)**. 23%, 29% and 31% of the power are focused on the focal points corresponding to the first, second and third diffraction orders, respectively. On the other hand, the stretched inverse-designed device focuses most of the power (46%) in the first order focal point, as can be seen in **Figure 4.11(e)**, owing to a simpler structure, with a much smaller central block in particular.

# PART III: Fabrication of a near-infrared 3D-printed polarization beamsplitter

So far, we have demonstrated 3D-printed inverse-designed devices working in the millimeter-waves. Thanks to Maxwell's equations invariance when changing dimensions and wavelength, devices working in the millimeter-waves have the exact same behavior at any other wavelengths when scaled appropriately. In practice, making the same device 10,000 times smaller is technically very challenging. In this part we describe how we used an advanced two-photon-lithography-based 3D printing technique to experimentally demonstrate an inverse-designed polarization beamsplitter in the Near Infrared (NIR). Furthermore, as opposed to conventional meta-devices that act on light normally incident to the substrate, this polarization beamsplitter controls free-space light propagating parallel to the substrate.

## a) Design and fabrication

The device structure is the same as the 30º polarization beamsplitter that was fabricated for millimeter-waves in Part I (**Figure 4.3A**). Indeed, the SU-8 material used for NIR has similar dielectric constant as HIPS used in the millimeter-waves, $n \approx 1.5$. More generally, most common polymers used for 3D-printing have very similar dielectric properties from the visible to the micro-waves, except in the mid- and long-wavelength infrared where they tend to have large absorption. Therefore, the same structure printed at different scales should have the same functionality.

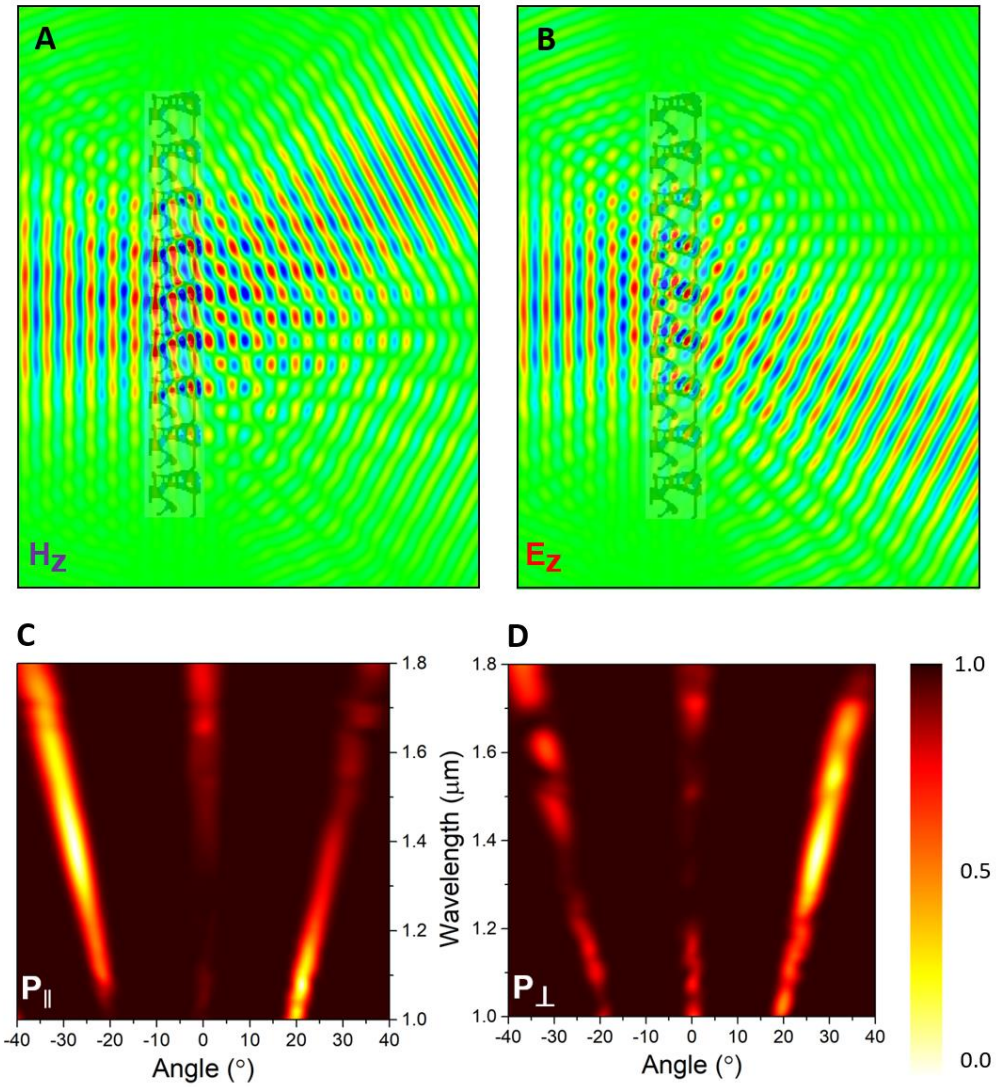


***Figure 4.14:*** *A-B) Simulations of the interaction between a Gaussian input at optimal wavelength with a structure made of 10 periods of the inverse-designed polarization beamsplitter. The magnetic field is shown in the case of parallel polarization (A), and the electric field is shown for perpendicular polarization (B). C-D) Simulated far-field profiles in the output of the 10-periods device under Gaussian illumination, for a parallel-polarized input (C) or a perpendicularly-polarized input (D). The optimization wavelength is chosen to be 1.5μm.*

In order to verify that the device behaves as expected under the conditions of the experiment, a 10-period structure is imported in Lumerical and simulated under illumination with

a Gaussian source from the left. The vertical fields at optimal wavelength are shown in **Figure 4.14A-B** in the cases of parallel (vertical magnetic field) and perpendicular (vertical electric field) polarizations, respectively. It is clear from the picture that most of the parallel polarization is bent to the left and most of the perpendicular polarization is bent to the right, as expected. A far-field monitor records the power sent as a function of the wavelength and the angle. The results are shown in **Figure 4.14C-D** for a device optimized for a wavelength of 1.5μm. As can be seen, the polarization splitting behavior is observed with a relatively high bandwidth, from 1.3μm to 1.7μm, which is due to the non-resonant behavior of the device.

A device working in the near-infrared, at a wavelength of 1.5μm, requires a fabrication method with at least 100-nm precision. This can be done with 2-photon lithography-based 3D printing methods developed recently[111, 112]. In this work, a commercial 3D laser lithography system (Photonic Professional from Nanoscribe GmbH) is employed to fabricate 3D optical components, in which a femtosecond laser at 780 nm wavelength with approximately 80MHz repetition frequency is used. The light is sent through an oil immersion objective 63 × (Zeiss) with a numerical aperture (NA) of 1.4, then focused into a high-resolution liquid photoresist (Nanoscribe IP-Dip) with an exposed refractive index of 1.54, which enables two-photon polymerization (TPP) only when the intensity of the focal spot is higher than the threshold intensity for TPP in the photoresist. Hence, the resolution is limited by the voxel size, which has a lateral diameter down to 100 nm depending on the laser power, writing speed, the NA of the objective and the sensitivity of the photoresist. In the dip-in mode, the objective lens of the system is immersed into the photoresist on a 25 mm × 25 mm fused silica slide, and the device is printed layer-by-layer vertically on top of the substrate. Although simulations assume an infinitely-wide

"2D" device, in practice the device has a finite width, chosen here to be 30 μm, which corresponds to 20 λ. The unit-cell size is 3 μm×3 μm (2 λ×2 λ), and the total length of the structure with 10 unit cells is 30 μm.

Due to the complexity of the structure and the required pixel size of 100 nm, which is close to the resolution limit of the Nanoscribe system, a low power input of approximately 6 mW is used, and the writing speed is approximately 50 μm/s. This allows the liquid polymer to be polymerized with a fine surface roughness but at the expense of a longer writing time of 6 h for one sample. After printing, the sample is removed from the sample holder and developed with propylene glycol monomethyl ether acetate (PEGMA, purity>99.5%) for 20 mins and IPA (purity>99.5%) for 15 mins and then dried using a $CO_2$ critical point dryer (Automegasamdri®-915B from Tousimis). Given the limited size of the sample and the close proximity of the substrate on which it is printed, it is virtually impossible to couple a focused beam from an objective to the side of the device without interactions with the substrate. To avoid this, the beamsplitter structure is actually printed on top of a large pre-printed support structure with a 30 μm-diameter support hole. After the structure is printed and developed, a tapered "capture fiber" is inserted through the support hole, and then a droplet of UV curable optical adhesive (NOA 61, Norland) is used to glue the sample to the fiber. At this point, the structure is attached to the capture fiber and can be lifted completely off the substrate. Now that the structure is on the capture fiber, it is easy to manipulate it spatially for alignment purposes. **Figure 4.15 A-B** shows the SEM images of the fabricated 3D inverse designed polarized beam splitter, while **Figure 4.15 C** shows an optical image of the structure on top of the support structure, which is itself supported by the fiber.

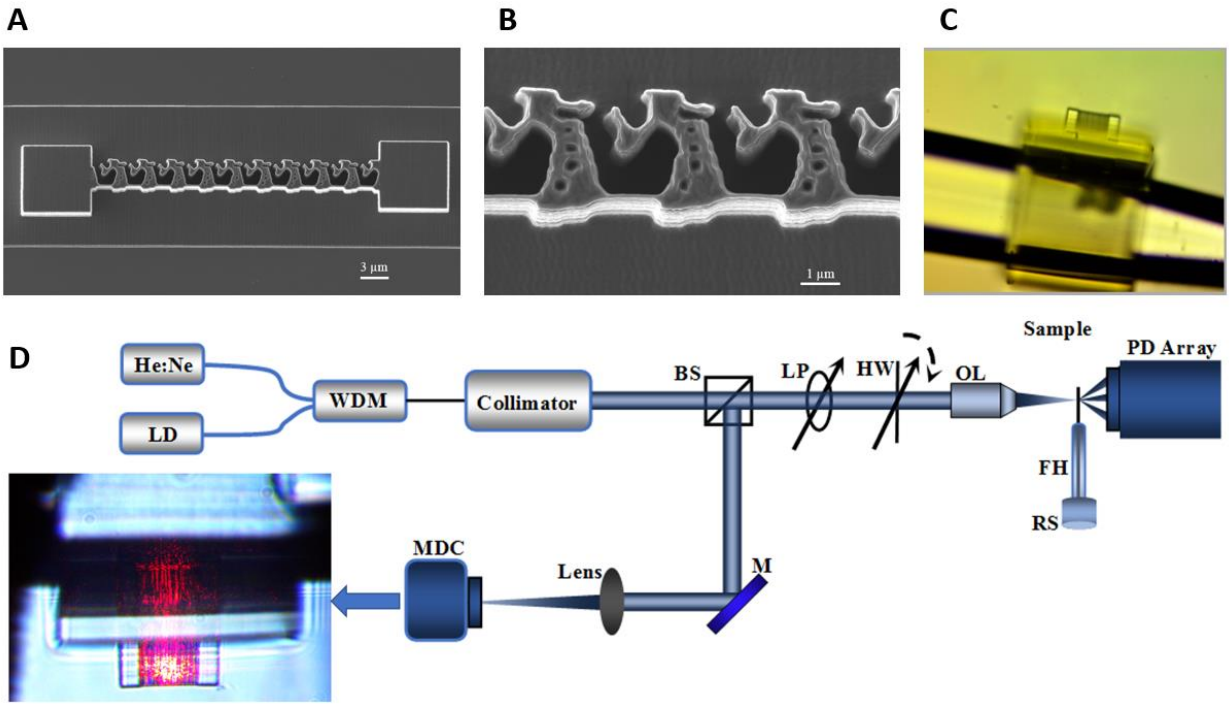


***Figure 4.15:*** *A-B) SEM of a test-structure of the 3D-printed polarization beamsplitter. C) Microscope image of the device used for optical characterization, printed on top of a cubic support structure, which is itself carried by a fiber. D) Schematic of the experimental setup to test the polarization beamsplitter. Labels: He:Ne, Helium Neon laser, LD, laser diode, WDM, wavelength division multiplexing, BS, beam splitter, LP, linear polarizer, HW, half wavelength, OL, objective lens, FH, fiber holder, RS, rotation stage, PD photodiode array, M, reflective mirror, MDC, microscope digital camera.*

## b) Characterization

In order to characterize the fabricated devices, optical measurements at near-infrared wavelengths were performed. A schematic representation of the experimental setup is shown in **Figure 4.15D**. A polarized Helium Neon laser (He: Ne, MELES GRIOT) with a wavelength of 633 nm and an average power of 5 mw is used for alignment by focusing the laser beam on the sample. Two laser diodes at 1.55 µm (LD, NLK 1556 STG) and 1.3 µm (LD, Optogear Model 1300) are used for testing. The lasers pass through a wavelength division multiplexing (WDM)

and are collimated by an optical fiber-based collimating system. After passing through a beam splitter (BS), a linear polarizer (LP) and a half-wave (HW) plate, the laser output is focused on the sample by an objective lens (Mitutoyo NIR 20×, with a numerical aperture of 0.4). The transmitted beam is collected by a [25.6 mm-wide] InGaAs photodiode (PD) linear array (Andor Technology, iDus DU492A-1.7) positioned 2 cm away from the sample, allowing measurement of the transmitted intensity as a function of the angle between 40° and -40°. The reflection beam of the visible light is focused by a lens and detected by a microscope digital camera (MDC, MU1403, AmScope. To allow for easy testing, the capture fiber containing the sample is mounted on a multi-axis rotation stage (RS). The inset of **Figure 4.15D** shows that the laser spot is focused on the sample, although there is some scattering light on the support.

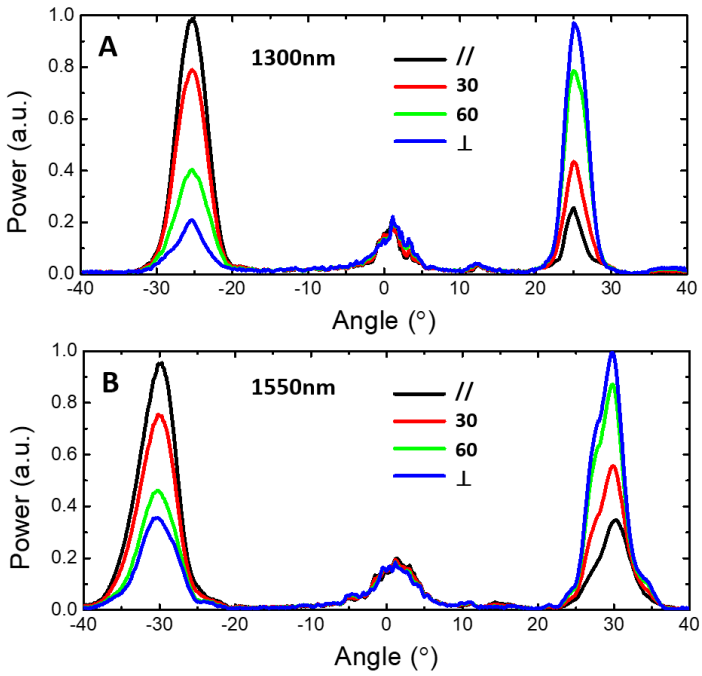


***Figure 4.16**: Experimental transmission of the polarization beamsplitter as a function of the angle for wavelengths of 1.3μm (A) and 1.55μm (B) and for polarizations between parallel and perpendicular polarizations.*

Measurements of the transmitted intensity as a function of the angle are shown in Figure [4] for wavelengths of 1.55 μm and 1.3 μm, respectively. For each wavelength, the polarization was changed by rotating a half waveplate (HW). Results are shown for parallel polarization, perpendicular polarization, and intermediate polarizations with angle of 30$^o$ and 60$^o$, respectively. The desired polarization beam-splitting is achieved for both wavelengths, with most of the parallel polarization going to the left peak, most of the perpendicular polarization going to the right, and only around 15% of the power in the center peak. The extinction ratios are $\frac{T_{\parallel}}{T_{\perp}} = 4.7$ and $\frac{T_{\perp}}{T_{\parallel}} = 3.8$ at 1.3 μm, and $\frac{T_{\parallel}}{T_{\perp}} = 2.7$ and $\frac{T_{\perp}}{T_{\parallel}} = 2.8$ at 1.55 μm. As expected, the splitting angle follows the grating equation, with 25$^o$ bending at 1.3 μm and 30$^o$ bending at 1.55 μm. This result illustrates the broad bandwidth of this device, which is a general property of non-resonant devices such as this.

# Conclusion

In conclusion, we have demonstrated a platform combining inverse-design and additive manufacturing for the design and fabrication of free-space meta-devices from the Near-Infrared to the microwaves. Most polymers have very stable dielectric properties over the whole spectrum, so the same design can be scaled to work with different materials and at different wavelengths. Given the properties of SU-8 in the visible part of the spectrum, shown in **Figure 4.17**, the devices presented in this part could work for wavelengths down to 400nm. Furthermore, thanks to the versatility of 3D printing method, devices can be printed to manipulate light either normally incident or parallel to the substrate (if any, typically for visible and IR wavelengths).

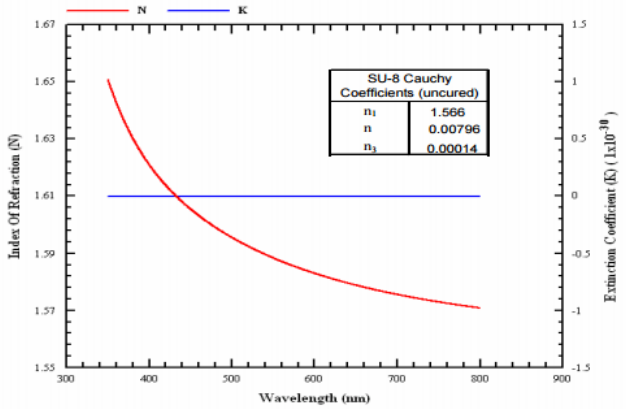


Figure 3. Cauchy Coefficients

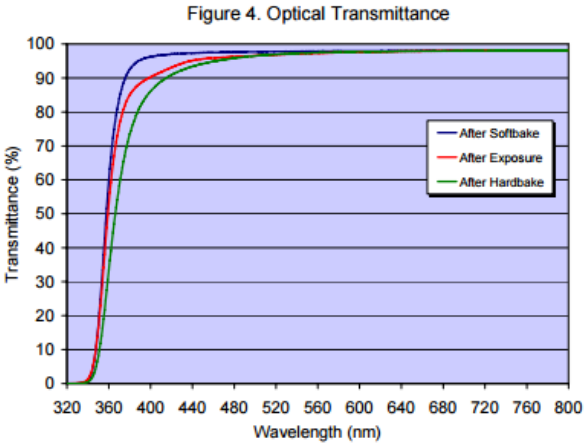


***Figure 4.17**: On the left, refractive index of the SU-8 as a function of the wavelength (red curve). On the right, optical transmittance as a function of the wavelength. Data from Microchem.*

We have demonstrated two millimeter-wave polarization beamsplitters at +/- 15º, +/-30º and a 30º bend for both polarizations. The design for the 30º beamsplitter has been reused successfully around 1.5µm, which is 5,000 times smaller than the millimeter-wave device. We also

demonstrated meta-lenses with various focal distances from very short (2.5λ) to long (20λ) distance. By carefully adapting our algorithm to output a sparse structure made of small building blocks, we designed a stretchable meta-lens, where the focal distance can be changed by a factor up to 4 for a stretching factor of only 1.8.

In our work, the design is planar with a very high aspect ratio (“infinite” height), but real 3-dimensional meta-devices could also be fabricated by adapting the algorithm and fabrication methods. Also, it would be rather simple to print multiple meta-devices along the light path to combine various functionalities, for example a polarization beamsplitter followed by two 1x2 or 1x3 wavelength beamsplitters could become a 1x4 or 1x6 beamsplitter.

# V) Conclusion and Future works

## a) Conclusion

We have demonstrated a method that can inverse-design a device to achieve desired optical behavior. More specifically, the method takes as input the desired boundary conditions (optical input and output) and finds a "good" permittivity map that can achieve these conditions, i.e. transform the given input into the desired output. We have demonstrated this method theoretically for multiple high-index devices, which could be realized practically with Silicon photonics. We have also shown that multiple functionalities can be achieved with low-index materials such as polymers, especially for manipulating free-space electromagnetic radiation.

In this work, we have pioneered the use of 3D-printing to fabricate inverse-designed devices, with experimental testing in the millimeter-waves and in the Near Infrared. We demonstrated multiple types of devices such as lenses, bends and beamsplitters. We showed that the same architecture could be replicated at a scale 5,000 times smaller while keeping a very similar behavior. We also demonstrated how the algorithm could be tuned to design a stretchable meta-lens with tunable focal distance.

These findings are just the beginning of the inverse-design story. Many new applications and enhancements can be explored. Here we show a few limitations of our algorithm that could become opportunities for future research:

_ We have worked with a **2D design space** (infinitely-thick) with **less than 10,000 pixels**, and dimensions typically not exceeding 5 wavelengths

_ Due to the two dimensions, we have only worked with light traveling **in-plane**

_ We have put very strict conditions on the materials, working only with **non-magnetic dielectric linear** materials ($\varepsilon > 0$) with **scalar permittivity**: **without gain or loss**

_ We have worked with simple **combinations of air and only one other material, which was either Silicon ($\varepsilon = 12$) or polymers ($\varepsilon = 2.3$)**.

_ We have only **optimized for one or few wavelengths**, because optimizing for several wavelengths at the same time increases the computational complexity.

In the next parts, we propose potential future works, including new types of devices that could be designed with existing software and fabricated, and enhancements to the software to implement new capabilities.

## b) Proposing new types of devices

There is a lot of interest for enhanced ability to manipulate light on-chip, for fast routing of light-information. Vuckovic's group has demonstrated an inverse-designed Silicon-based wavelength (de)multiplexer working in the Near Infrared. Various other useful devices could be realized by manipulating the modes, wavelengths or polarization. We can think of a polarization splitter to separate TE and TM polarizations from one single-mode input port to two single-mode outputs, a mode (de)multiplexer to separate the modes from a multimode input waveguide into different single-mode outputs, or a multimode waveguide bend that preserves the integrity of several modes after a 90° (or 180°) angle. Furthermore, combining several of those devices inside

"inverse—designed photonic chips" could lead to more advanced functionalities. As an example, one could think of combining a 1x3 mode (de)multiplexer with a 1x3 wavelength (de)multiplexer to obtain a 1x9 (de)multiplexer.

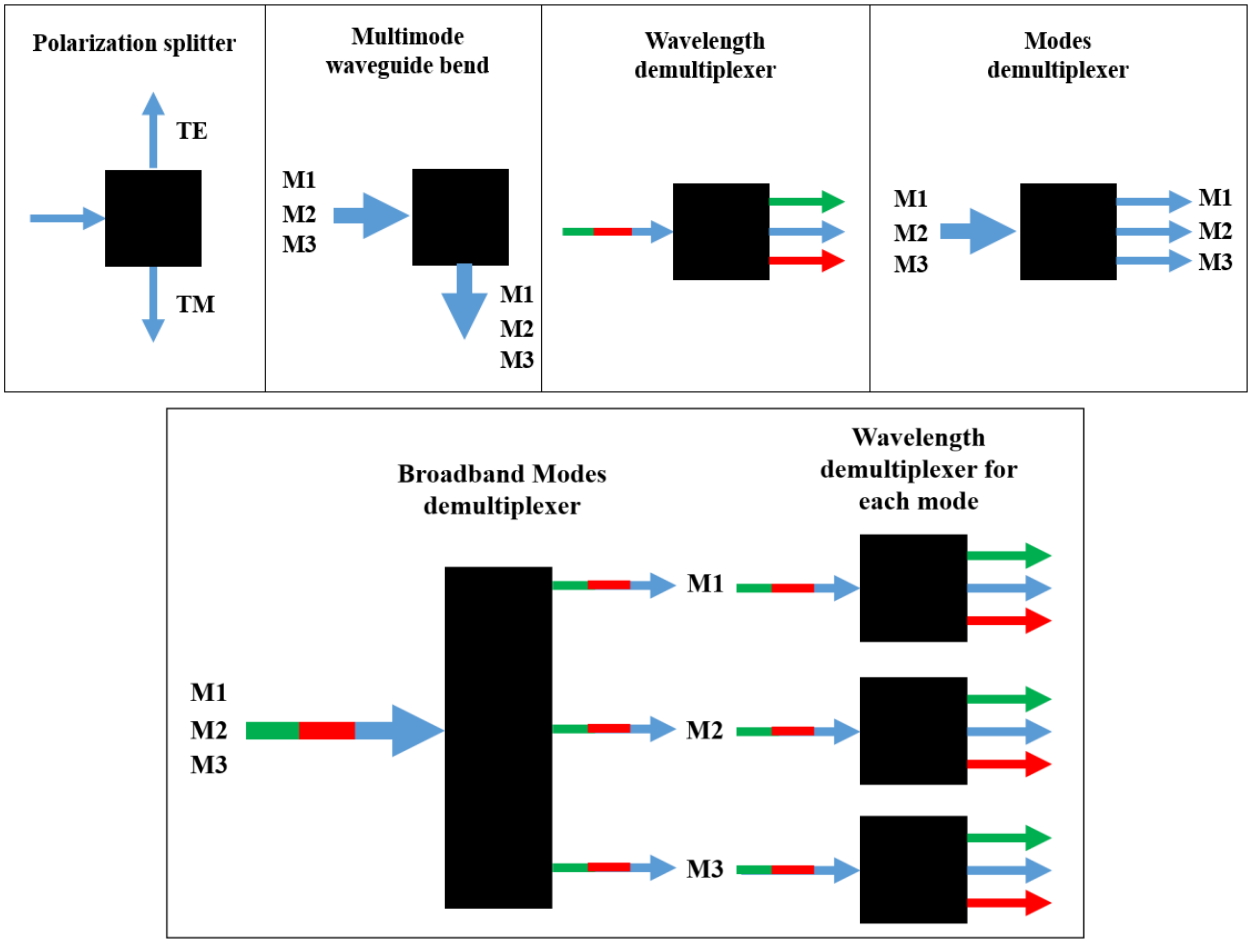


***Figure 5.1:*** *A few examples of nanophotonic devices that can be designed with our algorithm. On top, proposed single-devices. Bottom: a combination of a mode demultiplexer and three wavelength demultiplexers, one for each mode, to realize a 1x9 demultiplexer. We represent single-mode waveguides with thin arrows and multi-mode waveguides with large arrows.*

More possibilities could arise from the combination of inverse-design and 3D-printing, as one can start thinking about "3D-photonics". We provide a few examples of hypothetical devices

that could benefit from the new fabrication method. First, one could use inverse-design to improve the coupling between free-space light and a waveguide on-chip. This is especially critical with polymer materials, as typical gratings are limited to a 2-3% efficiency. On the other hand, preliminary simulations show that **inverse-designed gratings could improve the coupling efficiency 20-folds, to >60%**. Second, during the course of this work, a polymer-based wavelength demultiplexer project was unsuccessful due to light scattered and lost into the substrate after interacting with the device. 3D-printed suspended devices could prevent this scattering to happen. Third, very similarly to the polarization beamsplitter shown in chapter 4, one could design a beamsplitter to transmit one polarization and reflect the other polarization with a 90º angle, which would replicate the polarization splitting properties of a prism, within a very small device. Schematic representations of these three devices are shown in **Figure 5.2**.

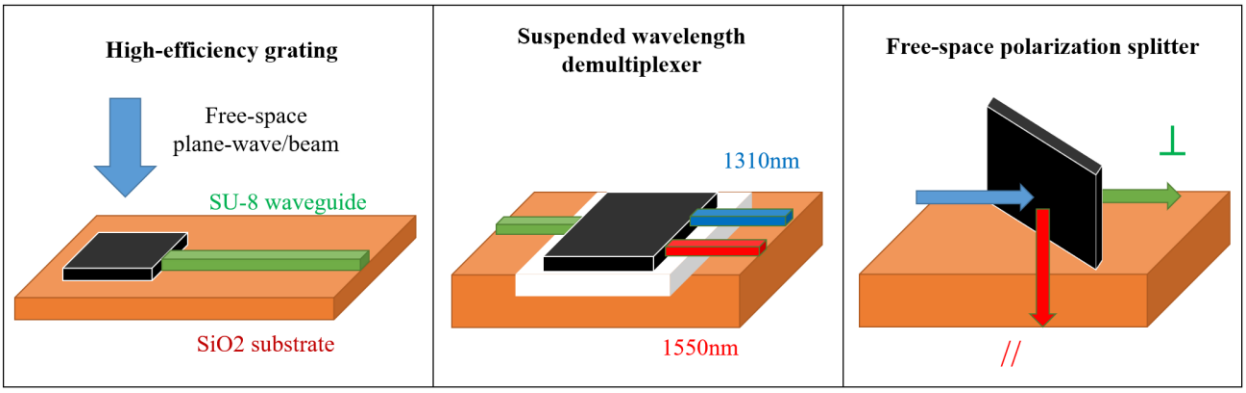


***Figure 5.2:*** *A few examples of 3D inverse-designed devices that are made possible by the 3D-printing. From left to right, a high-efficiency grating coupler, a suspended wavelength demultiplexer and a free-space polarization beamsplitter "nano-prism".*

Finally, we can imagine combining inverse-designed devices with active devices to enhance their properties. For example, the grating design proposed above could be modified by

rotational symmetry so that it would couple line in-plane and deflect it towards the center of the device. By placing a photodetector at the center, the “grating” allows to increase the optical area of the photodetector. This can be very useful for Infrared photodetectors where one wants to maximize the optical efficiency (proportional to the optical area) while minimizing the electronic noise, which is often proportional to the area of the detector. Inverse-design could also be used to design micron-scale lenses for the visible or near-infrared. Such lenses could be used to focus light from a fiber optics to a waveguide on-chip, which is a very difficult and inefficient task without aa lens due to the alignment precision required. This approach could also be used to transfer a signal created from an “active-chip” (with a laser) to a passive Silicon-based “processing chip” more easily. This would solve or ease a major hurdle in the development of Silicon photonics, where packaging is a critical step to connect active and passive devices.

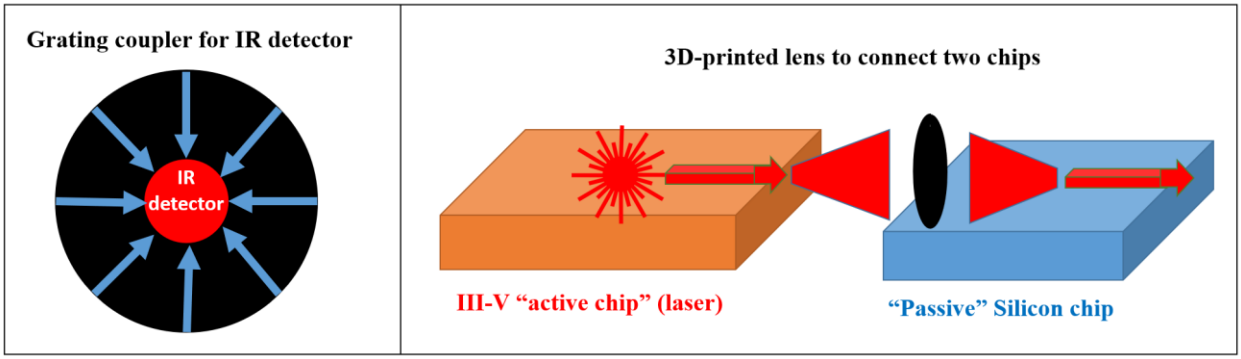


***Figure 5.3:*** *A few examples of devices where a 3D-printed inverse-design device can enhance the performance of an active device. On the left, a grating coupler increases the optical area of a photodetector. On the right, a micro-lens focuses the light coming out of a waveguide (diverging beam) from an active-chip towards the waveguide on a passive chip. This allows to keep efficient coupling with less strict alignment requirements.*

## c) Extending the algorithm capabilities

Inverse-design of electromagnetic devices is still at its infancy, as explained in a), and a lot has to be done to extend its capabilities to the design of the most general electromagnetic device, and with better control of the conditions. We propose here five areas of research that could lead to new types and better devices:

**1)** There is no fundamental difficulty to achieve a **fully 3-dimensional electromagnetic inverse-design**. Inverse-design has been achieved in 3D for mechanical devices[45], and in 2.5D (3D with the constraint of a planar device, meaning ε only depends on X and Y) for electromagnetic devices[55]. Compared to 2D, this will require between two and three orders of magnitude larger computational power, as well as improved visualization and fabrication techniques. For fabrication, the new 3D-printing approach that we explored for high aspect ratio planar devices seems very promising. Some **fabrication constraints** will need to be implemented in the inverse-design algorithm, such as a **lower precision in the Z-direction** (500nm, vs <100nm for X and Y), the **absence of free-standing structures** and the **ability for the polymer to leave the structure during development**.

**2) New regularization methods** can be implemented to match fabrication constraints. We have developed one regularization method, described in Chapter 2 f), used to decrease the permittivity variations, and as a result the amount of boundaries (the complexity) of the device. Other regularization methods have been developed to reduce the boundaries and the angles in the boundaries[120, 121]. New methods will need to be developed to accommodate fabrication

constraints for fully 3-dimensional inverse-designed devices. Additionally, the binarization could easily be adapted to the **design of devices with three or more materials**.

**3) New types of boundary conditions (BC)** can be explored. In this work, we have focused on waveguide-modes for on-chip communications, plane-waves and periodic BC for the design of gratings, and cylindrical waves for meta-lenses. We have also implemented (but not demonstrated here) Gaussian beam BC. Many other types of inputs/outputs can be explored. In particular, any type of field can be made and described as a **combination of plane-waves. Cylindrical or spherical Bessel functions** could also be used to make any type of optical beams. **Bloch BC** could be implemented for the design of photonic crystals[122] and metamaterials. **Perfect metal BC** could be used to design inverse-designed meta-antennas and meta-reflectarrays with dielectric structures around metals. One can also implement **interior BC, interior currents or dipole sources** to achieve new functionalities. For example, an invisibility cloak can be implemented by specifying the input and output boundary conditions to be the same and having null field in an interior part of the device. The algorithm could also be adapted to tune the coupling of an antenna to its environment, by modeling the antenna as a dipole source or by defining the currents at the surface of the antenna. Finally, **inequality-based BC**, such as "enforce output power >90%" could be used rather than the strict boundary conditions used in our algorithm.

**4)** Many tweaks can be implemented to **improve the optimization algorithm**, in order to escape local minima and fine-tune the optimization. For several reasons, regularization methods sometimes have unexpected positive impact on the physics residual optimization. Regularizations could also be implemented using inequality constraints rather than penalizing costs. Similar to genetic algorithms, adding perturbations to the structure during the optimization can help escape

local minima. Automated hyperparameter tuning could help select the best device size, waveguide size, initial permittivity, etc. Trying various random initial permittivity distributions rather than uniform permittivity could help explore a larger part of the whole design space. Finally, **combining different optimization methods** such as objective-first, topology optimization, and **using various modelling approaches** such as Finite-differences in the Frequency Domain (FDFD), Finite Elements and/or Rigorous Coupled-Wave Approximation (RCWA) could lead to a better overall optimization process and a better understanding of the physics behind it.

**5)** Bringing inverse-design to **other approximations of the wave equation** is probably the most promising research direction, because each approximation corresponds to a radically new type of device with different fundamental behaviors and opening new functionalities. In this work, we have focused on combinations of two dielectric materials: air-Silicon (high-index: $\varepsilon = 12$), and air-polymer (low-index: $\varepsilon = 2.3$), which is based on equation (1).

$$\nabla\times\nabla\times\mathbf{E}=w^2\varepsilon\mathbf{E}, \quad \varepsilon \text{ real and} > 0 \tag{1}$$

Already, these two configurations yield very different field-matter interactions. But very different electromagnetic behaviors and devices can be achieved with devices where the permittivity can be complex and/or negative, such as metals and metamaterials. Indeed, in metals, the permittivity follows the Drude model:

$$\varepsilon=\varepsilon_r-\frac{w_p^2}{w^2+i\gamma w} \tag{2}$$

where $\varepsilon_r$ is the real part of the permittivity, $w_p$ is the plasma frequency and $\gamma$ is the damping term responsible for the absorption. When w is very large (UV, visible), the metal behaves like a lossy

dielectric. Near-0 permittivity can occur when w is similar to the plasma frequency. When w becomes smaller than $w_p$, but with a similar order of magnitude, oscillations can occur in the metal depending on the excitation and the metal shape. Very complex behaviors can happen when combining materials with positive permittivity and materials with negative permittivity engineered at smaller scale than the wavelength. This is the realm of **plasmonics and metamaterials**, where inverse-design techniques could be very fruitful to invent new devices with better performance for making very compact plasmonic chips, focusing light below the diffraction limit, or achieving negative refraction. Creative optimization techniques such as those presented in[123] should be used to define constraints for complex permittivities, and avoid numerical errors that may arise around $\varepsilon \approx 0$. Finally, when w is much smaller than $w_p$, equation (1) can be replaced by (3):

$$\nabla \times \nabla \times \mathbf{E} = w\sigma \left( i - \frac{w}{\gamma} \right) \mathbf{E} \tag{3}$$

where $\sigma = w_p^2 / \gamma$ is the metal conductivity. In this regime, the metal acts like a conductor, with negative permittivity when $\gamma < w < w_p$, typically in the visible and infrared and imaginary permittivity when $w < \gamma$, typically in the long-wavelength infrared and longer wavelengths. In this last regime, the electromagnetic field behaves according to antenna theory between metal and air, and according to electronics circuit theory within the metal. Inverse-design could be used to optimize the shape of antennas[124] or radiofrequency systems. Finally, who knows what kind of devices could emerge by combining materials with dielectric properties, materials with plasmonic properties and materials with metallic properties at the same wavelength. This could happen in the infrared regime by combining doped Silicon (plasmonic), gold or silver (metal) and air.

Another promising research direction would be to use inverse-design with **magnetic materials**, where $\mu \neq 1$, and potentially with negative $\mu$ and/or $\varepsilon$, for the design of **negative-index devices**. Such **metamaterials** do not occur naturally but can be artificially created by making periodic arrangements dielectrics and metals with specific subwavelength geometries. Inverse-design approach could be used to design such metamaterials, then use them as building blocks for larger devices with complex functionalities.

Another level of complexity could be achieved with anisotropic materials[19], where the permittivity depends on the polarization and propagation direction of the light and must be represented by a tensor. There are two types of anisotropic materials, with their tensors shown in equation (4). A uniaxial material has an optic axis such that light propagating along this axis sees an "extraordinary" permittivity, and light propagating perpendicularly to the axis sees an "ordinary" permittivity. Biaxial materials do not have an optical axis, and the tensor representing the permittivity can take any form as long as it remains Hermitian.

$$\text{uniaxial:} \begin{pmatrix} \varepsilon_o & 0 & 0 \\ 0 & \varepsilon_o & 0 \\ 0 & 0 & \varepsilon_e \end{pmatrix} \text{ - biaxial:} \begin{pmatrix} \varepsilon_{xx} & \varepsilon_{xy} & \varepsilon_{xz} \\ \varepsilon_{yx} & \varepsilon_{yy} & \varepsilon_{yz} \\ \varepsilon_{zx} & \varepsilon_{zy} & \varepsilon_{zz} \end{pmatrix} \tag{4}$$

Among those materials, gyrotropic materials are of particular interest, as they are the basis to build Faraday rotators and optical isolators. The permittivity tensor of those materials is real symmetric under 0 magnetic field, but under perturbation from a quasi-static magnetic field $H_{qs}$, an imaginary component appears in the non-diagonal terms, such that:

$$\boldsymbol{\varepsilon E} = \left(\boldsymbol{\varepsilon_r} - i\boldsymbol{\chi^m H_{qs}}\times\right)\mathbf{E} \tag{5}$$

where $\varepsilon_r$ is the rest permittivity and $\chi^m$ is the magneto-optical susceptibility. This is an example of magnetic nonlinearity. There can be multiple other types of **magnetic or electric nonlinearities**, such as a component of the permittivity proportional to **E** in $\chi^2$ materials, or proportional to $\mathbf{E}^2$ in $\chi^3$ materials. Adapting the inverse-design to these materials could yield an improved understanding and design of nonlinear optical devices. The optimization algorithm will be different, as can no longer fix the permittivity and optimize for the field only.

Finally, solving the regular wave equation can be costly for large devices, as the number of pixels in a 3D device roughly grows as $(10L/\lambda)^3$, where L is the device size and $\lambda$ is the shortest wavelength inside the device (could be very small in metals). For $L > 10\lambda$, the number of pixels becomes too large to solve in a reasonable time. However, some devices with one dimension larger than the other can still be modelled with reasonable time under the condition that light propagates mostly along the large dimension z, and that the permittivity varies slowly along z. Under those conditions, one can use the **slowly varying envelope approximation**:

$$\mathbf{E} = \mathbf{u}\exp(ikz) \quad \text{where } \frac{\partial^2 \boldsymbol{u}}{\partial z^2} \approx 0 \tag{6}$$

where $k=w\sqrt{\varepsilon_0}$ is the propagation constant and $\varepsilon_0$ is the average permittivity of the propagation medium, not necessarily the vacuum permittivity. Under this approximation, the wave equation becomes the **paraxial wave equation**:

$$\nabla_\perp^2 \mathbf{u} + 2ik\frac{\partial \mathbf{u}}{\partial z} + w^2(\varepsilon - \varepsilon_0)\mathbf{u} = 0 \tag{7}$$

where $\nabla_\perp^2$ is the transverse Laplacian along the plane x-y. This equation still needs a fine sampling along x and y, but the sampling along z only depends on the variations of the envelope, which

mainly depends on the variations of the permittivity. This approach could be very useful to study the propagation of beams through filters, or inside slightly perturbed waveguides or fiber optics. Compared to traditional inverse-design, only a slight change in the components of the A and b matrices (while solving Ax=b) is required, so the objective-first algorithm can still be used.

To conclude this part, **we have only scratched the surface of what inverse-design approaches can achieve, and much remains to be discovered!!**

# Appendix A: More on the wave equation

The steady-state wave equations in the frequency domain, with linear isotropic materials, for E-field and H-field, are:

$$\nabla\times\mu^{-1}\nabla\times\mathbf{E}=w^2\varepsilon\mathbf{E} \quad (1)$$

$$\nabla\times\varepsilon^{-1}\nabla\times\mathbf{H}=w^2\mu\mathbf{H} \quad (2)$$

When we write these equations as matrix equations, we have:

$$\begin{pmatrix} 0 & -D_z^H & D_y^H \\ D_z^H & 0 & -D_x^H \\ -D_y^H & D_x^H & 0 \end{pmatrix}\begin{pmatrix} \mu_x^{-1} & 0 & 0 \\ 0 & \mu_y^{-1} & 0 \\ 0 & 0 & \mu_z^{-1} \end{pmatrix}\begin{pmatrix} 0 & -D_z^E & D_y^E \\ D_z^E & 0 & -D_x^E \\ -D_y^E & D_x^E & 0 \end{pmatrix}\begin{pmatrix} E_x \\ E_y \\ E_z \end{pmatrix}=w^2\begin{pmatrix} \varepsilon_x & 0 & 0 \\ 0 & \varepsilon_y & 0 \\ 0 & 0 & \varepsilon_z \end{pmatrix}\begin{pmatrix} E_x \\ E_y \\ E_z \end{pmatrix} \quad (3)$$

$$\begin{pmatrix} 0 & -D_z^E & D_y^E \\ D_z^E & 0 & -D_x^E \\ -D_y^E & D_x^E & 0 \end{pmatrix}\begin{pmatrix} \varepsilon_x^{-1} & 0 & 0 \\ 0 & \varepsilon_y^{-1} & 0 \\ 0 & 0 & \varepsilon_z^{-1} \end{pmatrix}\begin{pmatrix} 0 & -D_z^H & D_y^H \\ D_z^H & 0 & -D_x^H \\ -D_y^H & D_x^H & 0 \end{pmatrix}\begin{pmatrix} H_x \\ H_y \\ h_z \end{pmatrix}=w^2\begin{pmatrix} \mu_x & 0 & 0 \\ 0 & \mu_y & 0 \\ 0 & 0 & \mu_z \end{pmatrix}\begin{pmatrix} H_x \\ H_y \\ H_z \end{pmatrix} \quad (4)$$

Where the $D_{x,y,z}^{E,H}$ matrices represent first order finite-differences applied to different points in the Yee-grid (**Figure 6.1**) depending on the field and the vector component. The shape of those matrices in two dimensions can be found in [62].

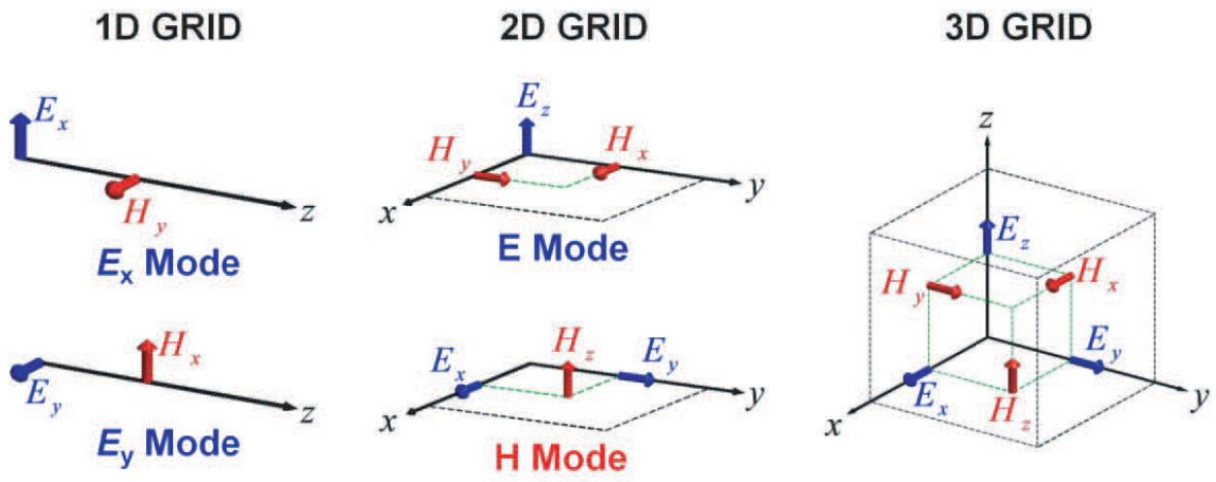


***Figure 6.1.*** *Representation of a unit-cell of the Yee grid for one, two or three-dimensional spaces. The three components of the vectors E and H are each at a different position in space, with half coordinates.*

When simplified assuming μ=1, the wave equations are quadratic. Equation (1) becomes:

$$\frac{1}{w^2}\,\nabla\times\nabla\times\mathbf{E}=\varepsilon\mathbf{E} \tag{5}$$

By calling **E** := x and ε := y, and by naming the operator A := $\frac{1}{w^2}\,\nabla\times\nabla\times$, the equation becomes Ax=xy. It should be obvious that this equation is non-linear in the variables, due to the product xy. However, we can write it as:

$$\frac{1}{2}\begin{bmatrix}x & y\end{bmatrix}\begin{bmatrix}0 & 1\\ 1 & 0\end{bmatrix}\begin{bmatrix}x\\ y\end{bmatrix}-\begin{bmatrix}A & 0\end{bmatrix}\begin{bmatrix}x\\ y\end{bmatrix}=0 \tag{6}$$

This is a quadratic equation ($\frac{1}{2}x^TPx+qx=0$) with real P and q but a complex variable, which is not a standard optimization problem. It can be reformulated with real variables by decomposing the field into real part R and imaginary part I:

$$\frac{1}{2}\begin{bmatrix} R & I & y \end{bmatrix}\begin{bmatrix} 0 & 0 & 1 \\ 0 & 0 & i \\ 1 & i & 0 \end{bmatrix}\begin{bmatrix} R \\ I \\ y \end{bmatrix} - \begin{bmatrix} A & iA & 0 \end{bmatrix}\begin{bmatrix} R \\ I \\ y \end{bmatrix} = 0 \quad (7)$$

With a real variable, the P matrix and q vector both become complex, which means that the optimization is **non-convex**, therefore it is a **NP-hard problem**. Indeed, only quadratic problems with real valued symmetric P and real valued q are convex.

# Appendix B: Code structure

The code behind our algorithm is called by *Sim_2D*, which allows to define most parameters of the problem: number of objectives, wavelengths (expressed in number of pixels), solve with E or H equation, TE or TM wave, size of the design space, size and position of the waveguides (if any), types of input/output, regularization and binarization hyperparameters, initial conditions, material constraints and interior conditions. This function then calls the function to run the job, which is organized in four main parts: **definition of the problem**, with *create_specs* and *matrices*, the **optimization** itself, which is run within *solve_waveguide*, the **simulations and representation of the performances** after each optimization iteration, which is done by simulate and plot within solve_waveguide, and finally **save the results**. Each of these parts have sub-functions to realize specific jobs, such as finding the waveguide modes, creating the finite-differences matrices, computing the Poynting vector to find output power… A functional representation of the code with all imbricated functions is shown in **Figure 6.2.**

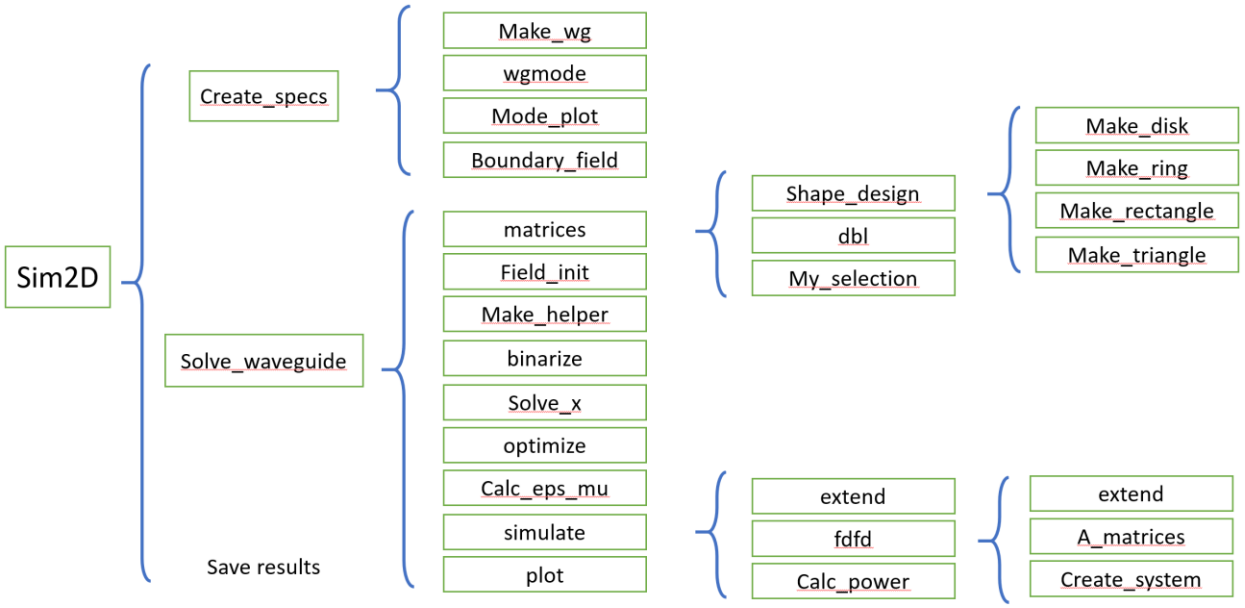


***Figure 6.2.*** *Functional representation of the code structure that we have implemented to do inverse-design.*

# References


1. Griffiths, D.J., *Introduction to Electrodynamics*. 1999: Prentice Hall.
2. Mansuripur, M., *Classical Optics and Its Applications*. 2002: Cambridge University Press.
3. Goodman, J.W., *Introduction to Fourier Optics*. 2005: W. H. Freeman.
4. Lax, M., W.H. Louisell, and W.B. McKnight, *MAXWELL TO PARAXIAL WAVE OPTICS.* Physical Review A, 1975. **11**(4): p. 1365-1370.
5. O'Shea, D.C., et al., *Diffractive Optics: Design, Fabrication, and Test*. 2004: Society of Photo Optical.
6. Joannopoulos, J.D., et al., *Photonic Crystals: Molding the Flow of Light, 2nd Edition*. Photonic Crystals: Molding the Flow of Light, 2nd Edition. 2008, Princeton: Princeton Univ Press. 1-286.
7. Engheta, N. and R.W. Ziolkowski, *Metamaterials: Physics and Engineering Explorations*. 2006: Wiley.
8. Kildishev, A.V., A. Boltasseva, and V.M. Shalaev, *Planar Photonics with Metasurfaces.* Science, 2013. **339**(6125).
9. Yu, N. and F. Capasso, *Flat optics with designer metasurfaces.* Nat Mater, 2014. **13**(2): p. 139-150.
10. Chen, H.Y., C.T. Chan, and P. Sheng, *Transformation optics and metamaterials.* Nature Materials, 2010. **9**(5): p. 387-396.
11. Leonhardt, U., *Optical conformal mapping.* Science, 2006. **312**(5781): p. 1777-1780.
12. Pendry, J.B., D. Schurig, and D.R. Smith, *Controlling electromagnetic fields.* Science, 2006. **312**(5781): p. 1780-1782.

13. Boyd, R.W., *Nonlinear Optics*. 2013: Elsevier Science.

14. Taflove, A., *Computational electrodynamics.* 2000.

15. Jin, J.M., *The Finite Element Method in Electromagnetics*. 2015: Wiley.

16. Gibson, W.C., *The Method of Moments in Electromagnetics, Second Edition*. 2014: CRC Press.

17. Margengo, E.A., C.M. Rappaport, and E.L. Miller, *Optimum PML ABC conductivity profile in FDFD.* IEEE Transactions on Magnetics, 1999. **35**(3): p. 1506-1509.

18. Shin, W., et al., *3D Finite-difference Frequency-domain Method for Plasmonics and Nanophotonics*. 2013.

19. Rumpf, R., et al., *Finite-Difference Frequency-Domain Algorithm for Modeling Electromagnetic Scattering From General Anisotropic Objects*. Vol. 61. 2014. 55-67.

20. Moharam, M.G. and T.K. Gaylord, *RIGOROUS COUPLED-WAVE ANALYSIS OF PLANAR-GRATING DIFFRACTION.* Journal of the Optical Society of America, 1981. **71**(7): p. 811-818.

21. Moharam, M.G., et al., *FORMULATION FOR STABLE AND EFFICIENT IMPLEMENTATION OF THE RIGOROUS COUPLED-WAVE ANALYSIS OF BINARY GRATINGS.* Journal of the Optical Society of America a-Optics Image Science and Vision, 1995. **12**(5): p. 1068-1076.

22. Van Roey, J., J. van der Donk, and P.E. Lagasse, *Beam-propagation method: analysis and assessment.* Journal of the Optical Society of America, 1981. **71**(7): p. 803-810.

23. Chung, Y. and N. Dagli, *AN ASSESSMENT OF FINITE-DIFFERENCE BEAM PROPAGATION METHOD.* Ieee Journal of Quantum Electronics, 1990. **26**(8): p. 1335-1339.

24. Saitoh, K. and M. Koshiba, *Full-vectorial imaginary-distance beam propagation method based on a finite element scheme: Application to photonic crystal fibers.* Ieee Journal of Quantum Electronics, 2002. **38**(7): p. 927-933.

25. Raju, G.S.N., *Antennas and Wave Propagation*. 2006: Pearson Education.

26. Hansen, R.C., *Phased Array Antennas*. 2009: Wiley.

27. Maier, S.A., *Plasmonics: Fundamentals and Applications*. 2007: Springer US.

28. Polman, A., *Plasmonics Applied.* Science, 2008. **322**(5903): p. 868-869.

29. Schurig, D., et al., *Metamaterial Electromagnetic Cloak at Microwave Frequencies.* Science, 2006. **314**(5801): p. 977-980.

30. Cai, W., et al., *Optical cloaking with metamaterials.* Nat Photon, 2007. **1**(4): p. 224-227.

31. Smith, D.R., et al., *Determination of Effective Permittivity and Permeability of Metamaterials from Reflection and Transmission Coefficients.* arXiv:physics/0111203, 2001.

32. Liao, P., *Theory of Dielectric Optical Waveguides 2e*. 2012: Elsevier Science.

33. *Optical Fiber Communications*, in *Wiley Encyclopedia of Telecommunications*.

34. Soref, R., *The Past, Present, and Future of Silicon Photonics.* Selected Topics in Quantum Electronics, IEEE Journal of, 2006. **12**(6): p. 1678-1687.

35. Shacham, A., K. Bergman, and L.P. Carloni, *Photonic Networks-on-Chip for Future Generations of Chip Multiprocessors.* IEEE Transactions on Computers, 2008. **57**(9): p. 1246-1260.

36. Bendsøe, P.M. and O. Sigmund, *Material interpolation schemes in topology optimization.* Archive of Applied Mechanics. **69**(9): p. 635-654.

37. Kiziltas, G., et al., *Topology design optimization of dielectric substrates for bandwidth improvement of a patch antenna.* IEEE Transactions on Antennas and Propagation, 2003. **51**(10): p. 2732-2743.

38. Borel, P.I., et al., *Topology optimization and fabrication of photonic crystal structures.* Optics Express, 2004. **12**(9): p. 1996-2001.

39. Jensen, J.S. and O. Sigmund, *Systematic design of photonic crystal structures using topology optimization: Low-loss waveguide bends.* Applied Physics Letters, 2004. **84**(12): p. 2022-2024.

40. Frandsen, L.H., et al., *Broadband photonic crystal waveguide 60° bend obtained utilizing topology optimization.* Optics Express, 2004. **12**(24): p. 5916-5921.

41. Jensen, J.S. and O. Sigmund, *Topology optimization of photonic crystal structures: a high-bandwidth low-loss T-junction waveguide.* Journal of the Optical Society of America B-Optical Physics, 2005. **22**(6): p. 1191-1198.

42. Jensen, J.S. and O. Sigmund, *Topology optimization for nano-photonics.* Laser & Photonics Reviews, 2011. **5**(2): p. 308-321.

43. Wang, F., J.S. Jensen, and O. Sigmund, *Robust topology optimization of photonic crystal waveguides with tailored dispersion properties.* Journal of the Optical Society of America B, 2011. **28**(3): p. 387-397.

44. Elesin, Y., et al., *Design of robust and efficient photonic switches using topology optimization.* Photonics and Nanostructures - Fundamentals and Applications, 2012. **10**(1): p. 153-165.

45. Sigmund, O. and K. Maute, *Topology optimization approaches.* Structural and Multidisciplinary Optimization, 2013. **48**(6): p. 1031-1055.

46. Frandsen, L.H., et al., *Topology optimized mode conversion in a photonic crystal waveguide fabricated in silicon-on-insulator material.* Optics Express, 2014. **22**(7): p. 8525-8532.

47. Yu, S., et al., *Topology optimization for light-trapping structure in solar cells.* Structural and Multidisciplinary Optimization, 2014. **50**(3): p. 367-382.

48. Vial, B. and Y. Hao, *Topology optimized all-dielectric cloak: design, performances and modal picture of the invisibility effect.* Optics Express, 2015. **23**(18): p. 23551-23560.

49. Yang, J. and J.A. Fan, *Topology-optimized metasurfaces: impact of initial geometric layout.* Optics Letters, 2017. **42**(16): p. 3161-3164.

50. Sell, D., et al., *Visible Light Metasurfaces Based on Single-Crystal Silicon.* ACS Photonics, 2016. **3**(10): p. 1919-1925.

51. Yang, J. and J.A. Fan, *Analysis of material selection on dielectric metasurface performance.* Optics Express, 2017. **25**(20): p. 23899-23909.

52. Sell, D., et al., *Large-Angle, Multifunctional Metagratings Based on Freeform Multimode Geometries.* Nano Letters, 2017. **17**(6): p. 3752-3757.

53. Jianji, Y., S. David, and F.J. A., *Freeform Metagratings Based on Complex Light Scattering Dynamics for Extreme, High Efficiency Beam Steering.* Annalen der Physik, 2018. **530**(1): p. 1700302.

54. Lu, J. and J. Vuckovic, *Inverse design of nanophotonic structures using complementary convex optimization.* Optics Express, 2010. **18**(4): p. 3793-3804.

55. Lu, J., S. Boyd, and J. Vučković, *Inverse design of a three-dimensional nanophotonic resonator.* Optics Express, 2011. **19**(11): p. 10563-10570.

56. Lu, J. and J. Vučković, *Objective-first design of high-efficiency, small-footprint couplers between arbitrary nanophotonic waveguide modes.* Optics Express, 2012. **20**(7): p. 7221-7236.

57. Lu, J. and J. Vučković, *Nanophotonic computational design.* Optics Express, 2013. **21**(11): p. 13351-13367.

58. Lu, J. and J. Vuckovic, *Objective-First Nanophotonic Design*, in *Numerical Methods for Metamaterial Design*, K. Diest, Editor. 2013, Springer Netherlands. p. 147-173.

59. Piggott, A.Y., et al., *Inverse design and implementation of a wavelength demultiplexing grating coupler.* Sci. Rep., 2014. **4**.

60. Piggott, A.Y., et al., *Inverse design and demonstration of a compact and broadband on-chip wavelength demultiplexer.* Nature Photonics, 2015. **9**(6): p. 374-+.

61. Kane, Y., *Numerical solution of initial boundary value problems involving maxwell's equations in isotropic media.* Antennas and Propagation, IEEE Transactions on, 1966. **14**(3): p. 302-307.

62. Rumpf, R.C., *Simple implementation of arbitrarily shaped total-field/scattered-field regions in finite-difference frequency-domain.* Progress In Electromagnetics Research B, 2012. **36**.

63. Wang, C., C.-Z. Zhou, and Z.-Y. Li, *On-chip optical diode based on silicon photonic crystal heterojunctions.* Optics Express, 2011. **19**(27): p. 26948-26955.

64. Lu, C.C., et al., *Ultrahigh-contrast and wideband nanoscale photonic crystal all-optical diode.* Optics Letters, 2011. **36**(23): p. 4668-4670.

65. Fan, L., et al., *An All-Silicon Passive Optical Diode.* Science, 2012. **335**(6067): p. 447-450.

66. Liu, V., D.A.B. Miller, and S.H. Fan, *Ultra-compact photonic crystal waveguide spatial mode converter and its connection to the optical diode effect.* Optics Express, 2012. **20**(27): p. 28388-28397.

67. Xu, Y.D., et al., *Broadband asymmetric waveguiding of light without polarization limitations.* Nature Communications, 2013. **4**: p. 8.

68. Khavasi, A., et al., *A heuristic approach to the realization of the wide-band optical diode effect in photonic crystal waveguides.* Journal of Optics, 2013. **15**(7): p. 5.

69. Zhang, Y., et al., *Silicon optical diode based on cascaded photonic crystal cavities.* Optics Letters, 2014. **39**(6): p. 1370-1373.

70. Zhang, Y., Q. Kan, and G.P. Wang, *One-way optical transmission in silicon grating-photonic crystal structures.* Optics Letters, 2014. **39**(16): p. 4934-4937.

71. Shen, B., R. Polson, and R. Menon, *Integrated digital metamaterials enables ultra-compact optical diodes.* Optics Express, 2015. **23**(8): p. 10847-10855.

72. Shen, B., R. Polson, and R. Menon, *Broadband asymmetric light transmission via all-dielectric digital metasurfaces.* Optics Express, 2015. **23**(16): p. 20961-20970.

73. Jalas, D., et al., *What is - and what is not - an optical isolator.* Nature Photonics, 2013. **7**(8): p. 579-582.

74. Espinola, R.L., et al., *Magneto-optical nonreciprocal phase shift in garnet/silicon-on-insulator waveguides.* Optics Letters, 2004. **29**(9): p. 941-943.

75. Zaman, T.R., X. Guo, and R.J. Ram, *Faraday rotation in an InP waveguide.* Applied Physics Letters, 2007. **90**(2): p. 023514.

76. Dötsch, H., et al., *Applications of magneto-optical waveguides in integrated optics: review.* Journal of the Optical Society of America B, 2005. **22**(1): p. 240-253.

77. Bi, L., et al., *On-chip optical isolation in monolithically integrated non-reciprocal optical resonators.* Nature Photonics, 2011. **5**(12): p. 758-762.

78. Zongfu, Y. and F. Shanhui, *Complete optical isolation created by indirect interband photonic transitions.* Nature Photonics, 2009. **3**(2): p. 91-94.

79. Menzel, C., et al., *Asymmetric Transmission of Linearly Polarized Light at Optical Metamaterials.* Physical Review Letters, 2010. **104**(25): p. 4.

80. Mutlu, M., et al., *Diodelike Asymmetric Transmission of Linearly Polarized Waves Using Magnetoelectric Coupling and Electromagnetic Wave Tunneling.* Physical Review Letters, 2012. **108**(21): p. 213905.

81. Schwanecke, A.S., et al., *Nanostructured metal film with asymmetric optical transmission.* Nano Letters, 2008. **8**(9): p. 2940-2943.

82. Fedotov, V.A., et al., *Asymmetric propagation of electromagnetic waves through a planar chiral structure.* Physical Review Letters, 2006. **97**(16): p. 4.

83. Singh, R., et al., *Terahertz metamaterial with asymmetric transmission.* Physical Review B, 2009. **80**(15): p. 4.

84. Xu, T. and H.J. Lezec, *Visible-frequency asymmetric transmission devices incorporating a hyperbolic metamaterial.* Nature Communications, 2014. **5**: p. 7.

85. Feng, L., et al., *Nonreciprocal Light Propagation in a Silicon Photonic Circuit.* Science, 2011. **333**(6043): p. 729-733.

86. Serebryannikov, A.E., *One-way diffraction effects in photonic crystal gratings made of isotropic materials.* Physical Review B, 2009. **80**(15): p. 13.

87. Callewaert, F., et al., *Inverse design of an ultra-compact broadband optical diode based on asymmetric spatial mode conversion.* Scientific Reports, 2016. **6**: p. 32577.

88. Callewaert, F., et al., *Inverse designed broadband all-dielectric electromagnetic metadevices.* arXiv:1706.08486, 2017.

89. Zhao, Q., et al., *Mie resonance-based dielectric metamaterials.* Materials Today, 2009. **12**(12): p. 60-69.

90. Cubukcu, E., et al., *Subwavelength Resolution in a Two-Dimensional Photonic-Crystal-Based Superlens.* Physical Review Letters, 2003. **91**(20): p. 207401.

91. Mandatori, A., M. Bertolotti, and C. Sibilia, *Asymmetric transmission of some two-dimensional photonic crystals.* Journal of the Optical Society of America B, 2007. **24**(3): p. 685-690.

92. Yao, J., et al., *Optical Negative Refraction in Bulk Metamaterials of Nanowires.* Science, 2008. **321**(5891): p. 930-930.

93. Pendry, J.B., *Negative Refraction Makes a Perfect Lens.* Physical Review Letters, 2000. **85**(18): p. 3966-3969.

94. Shelby, R.A., D.R. Smith, and S. Schultz, *Experimental Verification of a Negative Index of Refraction.* Science, 2001. **292**(5514): p. 77-79.

95. Fang, N., et al., *Sub–Diffraction-Limited Optical Imaging with a Silver Superlens.* Science, 2005. **308**(5721): p. 534-537.

96. Yu, N., et al., *Light Propagation with Phase Discontinuities: Generalized Laws of Reflection and Refraction.* Science, 2011. **334**(6054): p. 333.

97. Cui, T.J., et al., *Coding metamaterials, digital metamaterials and programmable metamaterials.* Light Sci Appl, 2014. **3**: p. e218.

98. Lin, D., et al., *Dielectric gradient metasurface optical elements.* Science, 2014. **345**(6194): p. 298.

99. Li, Z., et al., *Visible-Frequency Metasurfaces for Broadband Anomalous Reflection and High-Efficiency Spectrum Splitting.* Nano Letters, 2015. **15**(3): p. 1615-1621.

100. Zheng, G., et al., *Metasurface holograms reaching 80% efficiency.* Nat Nano, 2015. **10**(4): p. 308-312.

101. Qin, F., et al., *Hybrid bilayer plasmonic metasurface efficiently manipulates visible light.* Science Advances, 2016. **2**(1).

102. Li, X., et al., *Multicolor 3D meta-holography by broadband plasmonic modulation.* Science Advances, 2016. **2**(11).

103. Wang, P., N. Mohammad, and R. Menon, *Chromatic-aberration-corrected diffractive lenses for ultra-broadband focusing.* Scientific Reports, 2016. **6**: p. 21545.

104. Khorasaninejad, M., et al., *Broadband and chiral binary dielectric meta-holograms.* Science Advances, 2016. **2**(5).

105. Arbabi, A., et al., *Dielectric metasurfaces for complete control of phase and polarization with subwavelength spatial resolution and high transmission.* Nat Nano, 2015. **10**(11): p. 937-943.

106. Staude, I. and J. Schilling, *Metamaterial-inspired silicon nanophotonics.* Nat Photon, 2017. **11**(5): p. 274-284.

107. Kuznetsov, A.I., et al., *Optically resonant dielectric nanostructures.* Science, 2016. **354**(6314).

108. Khorasaninejad, M., et al., *Metalenses at visible wavelengths: Diffraction-limited focusing and subwavelength resolution imaging.* Science, 2016. **352**(6290): p. 1190-1194.

109. Khorasaninejad, M. and F. Capasso, *Metalenses: Versatile multifunctional photonic components.* Science, 2017.

110. Zhang, Y., et al., *Printing, folding and assembly methods for forming 3D mesostructures in advanced materials.* Nature Reviews Materials, 2017. **2**: p. 17019.

111. LaFratta, C.N., et al., *Multiphoton Fabrication.* Angewandte Chemie International Edition, 2007. **46**(33): p. 6238-6258.

112. Maruo, S. and J.T. Fourkas, *Recent progress in multiphoton microfabrication.* Laser & Photonics Reviews, 2008. **2**(1-2): p. 100-111.

113. Liang, M., et al., *A 3-D Luneburg Lens Antenna Fabricated by Polymer Jetting Rapid Prototyping.* IEEE Transactions on Antennas and Propagation, 2014. **62**(4): p. 1799-1807.

114. Du, G., et al., *3-D Printing Implementation of an X-band Eaton Lens for Beam Deflection.* IEEE Antennas and Wireless Propagation Letters, 2016. **15**: p. 1487-1490.

115. Wu, Z., et al., *Rapid and inexpensive fabrication of terahertz electromagnetic bandgap structures.* Optics Express, 2008. **16**(21): p. 16442-16451.

116. Wu, Z., et al., *Terahertz electromagnetic crystal waveguide fabricated by polymer jetting rapid prototyping.* Optics Express, 2011. **19**(5): p. 3962-3972.

117. Afsar, M.N., *Precision millimeter-wave measurements of complex refractive index, complex dielectric permittivity, and loss tangent of common polymers.* IEEE Transactions on Instrumentation and Measurement, 1987. **IM-36**(2): p. 530-536.

118. Callewaert, F., et al., *Inverse-designed stretchable metalens with tunable focal distance.* Applied Physics Letters, 2018. **112**(9): p. 091102.

119. Kamali, S.M., et al., *Highly tunable elastic dielectric metasurface lenses.* Laser & Photonics Reviews, 2016. **10**(6): p. 1002-1008.

120. Piggott, A.Y., et al., *Fabrication-constrained nanophotonic inverse design.* Scientific Reports, 2017. **7**(1): p. 1786.

121. Michaels, A. and E. Yablonovitch, *Gradient-Based Inverse Electromagnetic Design Using Continuously-Smoothed Boundaries.* arXiv:1705.07188, 2017.

122. Men, H., et al., *Robust topology optimization of three-dimensional photonic-crystal band-gap structures.* Optics Express, 2014. **22**(19): p. 22632-22648.

123. Wadbro, E. and C. Engström, *Topology and shape optimization of plasmonic nano-antennas.* Computer Methods in Applied Mechanics and Engineering, 2015. **293**: p. 155-169.

124. Hassan, E., E. Wadbro, and M. Berggren, *Topology Optimization of Metallic Antennas.* IEEE Transactions on Antennas and Propagation, 2014. **62**(5): p. 2488-2500.